Report No. FRA-ORD&D-74-42

PARAMETER OPTIMIZATION STUDIES OF MAGNETIC SUSPENSIONS FOR HIGH SPEED GROUND TRANSPORTATION

Robert H. Borcherts, L. C. Davis, C. C. Wan,
A. U. Mohdulla, John R. Reitz
Scientific Research Staff, Ford Motor Company
Dearborn, Michigan 48121

DEPARTMENT OF TRANSPORTATION • UNITED STATES OF AMERICA

April 1974

FINAL REPORT

Prepared for:

FEDERAL RAILROAD ADMINISTRATION
OFFICE OF RESEARCH, DEVELOPMENT AND DEMONSTRATIONS

WASHINGTON, D.C. 20590

TECHNICAL REPORT STANDARD TITLE PAGE

1. Report No. FRA-ORD&D-74-42

2. Government Accession No.

3. Recipient's Catalog No. PB 238 773

4. Title and Subtitle

Parameter Optimization Studies of Magnetic Suspensions for High Speed Ground Transportation

5. Report Date April, 1974

6. Performing Organization Code

7. Author(s)
Robert H. Borcherts, L. C. Davis, C. C. Wan,
A. U. Mohdulla, John R. Reitz

8. Performing Organization Report No.

9. Performing Organization Name and Address
Ford Motor Company
Transportation Research and Planning Office
23400 Michigan Avenue
Dearborn, Michigan 48124

10. Work Unit No.

11. Contract or Grant No. DOT-FR-10026

13. Type of Report and Period Covered
Final Report (Tasks VI and V) June 1973 - April 1974

12. Sponsoring Agency Name and Address
U. S. Department of Transportation
Federal Railroad Administration
400 Seventh Street S.W., Room 5416
Washington, D.C. 20591

14. Sponsoring Agency Code

15. Supplementary Notes Related reports include NTIS PB 223237 "Preliminary Design Studies of Magnetic Suspensions for High Speed Ground Transportation" (Ford Motor Co.) and FRA-ORD&D-74-41 "An Evaluation of the Dynamics of a Magnetically Levitated Vehicle" (SRI) PB236671

16. Abstract

The present study is part of a program, sponsored by the Office of Research, Development and Demonstrations, Federal Railroad Administration, to investigate efficient, cost-effective methods of high speed ground transportation for intercity travel. Previous aspects of the program have demonstrated the technical feasibility of two types of magnetic suspensions (the attractive-force, and the repulsive-force suspensions) for such applications, and have developed a baseline design for a TMLRV (tracked magnetically levitated research vehicle).

The present study is concerned with both of these magnetic suspensions. For the attractive force suspension the objective was the development of a mathematical model which predicts the magnetic behavior of the magnet-rail system at high speed, and a parameter optimization of the magnet. For the repulsive-force suspension the goal was to examine various track geometries to see if the amount of aluminum in the track could be reduced without loss of performance. Experimental studies have been carried out to support the analytical aspects of the program.

17. Key Words Tracked Levitated vehicles, magnetic levitation, high speed ground transportation, lift-to-drag ratio, non-linear magnetic behavior, finite-height guideways, slotted and ladder tracks

18. Distribution Statement
Document is available to the public through the National Technical Information Service,
Springfield, Virginia 22151

19. Security Classif. (of this report)	20. Security Classif. (of this page)	21. No. of Pages	22. Price
Unclassified	Unclassified	168	6.25

Reproduced by

PREFACE

This report covers work performed by Ford Motor Company during the period June 1973 to April 1974 under Contract DOT-FR-10026 with the Office of Research, Development, and Demonstration of the Federal Railroad Administration. This is the last of four reports which have been written under the designated contract. Previous reports are: "Technical Feasibility of Magnetic Levitation as a Suspension System for High-Speed Ground Transportation Vehicles" (PB 210-506, Feb. 1972), "Preliminary Design Studies of Magnetic Suspensions for High-Speed Ground Transportation" (PB 223-237, March 1973), and "Experimental Ride Simulation Studies" (PB 224893/AS, June 1973).

The authors would like to express their appreciation to Dr. John T. Harding of the Federal Railroad Administration for his close liaison with the project and for a number of suggestions which improved the overall study.

TABLE OF CONTENTS

APPENDICIES

LIST OF FIGURES

1. INTRODUCTION

The use of magnetic levitation as a suspension mechanism for high-speed ground transportation has received considerable attention during the past five years. A recent study by Ford Motor Company[1] under contract to the U.S. Department of Transportation focused on the principal problem areas peculiar to this type of suspension, and presented a baseline design for a research vehicle. This work, together with earlier DOT-sponsored studies at Ford and Stanford Research Institute[2,3] and development programs in Germany and Japan, have established the basic feasibility of magnetic suspension for ground vehicles moving at speeds of 480 km/h (300 mi/h).

There are, in fact, two viable magnetic suspension schemes, the electrodynamic (or repulsive-force) suspension, and the electromagnetic (or attractive force) suspension. Both suspensions appear capable of guiding and supporting a vehicle at speeds of 480 km/h, but the system specifications are different for the two cases. The repulsive-force suspension is an inherently-stable, large-gap suspension system which uses superconducting magnets in the vehicle and aluminum reaction surfaces in the guideway. No secondary suspension is required, and satisfactory-to-good ride quality can be achieved by means of active control.[4] The attractive-force suspension is a small-gap suspension system using ordinary electromagnets in the vehicle and steel track. Although inherently unstable, the suspension is stablized by gap sensing and magnet-current control via a feed-back control system. Satisfactory ride quality is achieved by using both current control and a secondary suspension.

The principal problem areas of both of these suspensions have been discussed in reference 1. As a result of that study, methods have been developed to circumvent the critical problem areas; however, complete solution to some of these problems must await high-speed and/or full-scale testing. In particular, we have not been able, on the basis of analytic studies and model experiments, to designate one of the two magnetic suspensions as clearly superior to the other for use with high-speed ground vehicles. A recent RFP from the Department of Transportation[5] proposes a program to provide this evaluation; this is a rocket sled program in which model vehicles supported by one or the other of these suspensions are accelerated to speeds of 480 km/h and their dynamic behavior studied. The program is planned for implementation in early 1974.

Other recent developments in the magnetic levitation field include an experimental study of a 4.25 m long experimental vehicle, supported and guided by four superconducting magnets, to speeds of 12 m/s.[6] This work was carried out by Stanford Research Institute under D.O.T. contract. Larger scale experiments are continuing in Japan and Germany. The Japan National Railways vehicle is 7 m long, 2 m wide, 1.7 m high, uses superconducting magnets, and is powered by a linear induction motor. It is being test run on a 400 m track at speeds up to 60 km/h. Messerschmitt-Bölkow-Blohm (MBB) and Krauss-Maffei (KM) in Germany are pursuing their development of the attractive-force suspension with rocket-propelled vehicles to speeds of 300 km/h. Recent papers bearing on the attractive-force suspension include a study of system dynamics and the vehicle control system[7] and an overall system study.[8]

The present report covers work performed by the Ford Motor Company under Contract DOT-FR-10026 (Tasks IV and V) with the Office of Research, Development and Demonstration of the Federal Railroad Administration, U.S. Department of Transportation. This study has limited, but well-defined objectives. For the attractive-force suspension the goals are to conduct analytic and experimental studies necessary to develop a mathematical model which predicts the penetration of magnetic flux into a ferromagnetic rail as a function of magnet geometry, vehicle speed, magnetic and electrical properties of the rail, and rail geometry. This involves extending the model formulated in reference 1 to include both the effect of three-dimensional field configurations and the non-linear effect caused by saturation of the magnetic yoke and rail. Earlier studies[1] had shown that the reduced flux penetration into the track at the higher speeds would substantially degrade the levitation force and also increase drag. It was also shown that this effect could be mitigated either by laminating the track or by making the levitation magnets very long, but detailed parameter optimization studies were not carried out at that time.

For the repulsive-force suspension the goal is to examine various track geometries to determine whether the amount of aluminum in the track can be reduced without significant loss in lift-to-drag ratio or of guidance. Specifically, we have studied various corner guideway configurations to determine the effect of guideway height (height of vertical member) on the guidance force, and have compared slotted- and ladder-track configurations with solid aluminum track as to potential lift and drag force. The effect of canted levitation coils (coils which are not parallel to the track surface) is also studied.

2. ELECTROMAGNETIC (ATTRACTIVE) SUSPENSION

Analytic and experimental studies were carried out during the course of this work in order to develop a mathematical model which predicts the penetration of magnetic flux into the ferromagnetic rail of an electromagnetic suspension system as a function of magnet geometry, speed, magnetic and electrical properties of the rail, and rail geometry. This involved extending the model formulated in our earlier studies (see e.g., reference 1, Sections 3.1 and 3.2) to include simultaneously the effect of three-dimensional field configurations and the non-linear effect caused by saturation of the yoke and rail. Experimental studies entailed the use of our 5 ft diameter rotating wheel, used in earlier studies of the repulsive force suspension, but which was modified to incorporate a steel plate to simulate the ferromagnetic rail of an attractive-force suspension.

2.1 Theoretical Modeling (including Effects of Limited Flux Penetration and Magnetic Saturation)

In the present task, we have substantially improved the model of the electromagnetic (attractive) suspension developed in Task II (see reference 1). These improvements are:

1) Derivation of a relationship between the magnetization currents (or the magnetization itself) and the real ampere-turns (NI) of the magnet. No connection between the two was made in Task II.

2) The track is mathematically divided into layers so that the effective permeability for each layer can be computed self-consistently. Previously the track was taken to be a single

region whose permeability was described by the equation (Eq. (3.19) of reference 1),

$$\varkappa = \frac{2L^2 B_s^{\ 2}}{\mu_o^{\ 2}\sigma\pi p\ F_L v} \qquad (2.1)$$

where L is the magnet length, $B_s \approx 2T$ is the saturation field of the iron, σ is the track conductivity, P = the width of the pole face, F_L is the required lift force, and v is the velocity. This formula greatly underestimates ϰ, although the dependence on L, F_L, and v are roughly correct. For example, the computed permeability from the model described in detail in subsequent sections is 56.3 for first layer of the track. Equation (2.1) gives only 7.1 (L = 1m, v = 134 m/s, F_L = 5.6 kN, $\rho = \sigma^{-1}$ = 13.25 μΩ-cm, and p = 4 cm). If we fit ϰ at this point and look at the dependence on L, F_L, and v, we obtain the results shown in Table 2.1. (See page 34).

3) Inclusion of a magnetization which is highly peaked at the edges of the magnet pole face. Previously, a uniform magnetization was used and this underestimates the lift considerably. For example, at v = 0 and air gap h = 1.5 cm, for a 1 m long magnet with p = 4 cm, the required ampere-turns for 10 kN of lift is 1.46×10^4 AT in the uniform-magnetization model, but only 1.23×10^4 AT in the present model. Comparison to experiment and other exact numerical calculations for v = 0 show the present model is more nearly correct.

A schematic drawing of the magnet and track is shown in Fig. 2.1. (The vertical is inverted for computational convenience.) We take $p = 2a$, $L = 2b$, and the distance between the pole centers to be c. The gap is h and the real ampere-turns are NI. The track considered is infinite in extent both laterally and in thickness. The latter is an unessential approximation which is, however, quite accurate because the track is thicker for structural reasons than the skin depth. The neglect of the effects of the finite width of the track could be a serious problem, except that we have noticed no serious inaccuracy in the predictions of our model relative to the experimental data which could be attributed to this source. (Comparison to experiment is made in Sec. 2.3.)

2.1.1. Multi-layer Model of Ferromagnetic Track

In this section we describe a multi-layer model of the track in which we determine the permeability of each layer self-consistently. This is the most accurate model that allows us to retain the essential simplicity of the Fourier methods we have used in the past for other problems and still treat the non-linear nature of the track. To solve the full non-linear problem rigorously appears to involve numerical techniques beyond the scope of the present investigation.

In Fig. 2.2, the model of the track is shown. The top portion of the track consists of N layers. The j^{th} layer lies between z_{j-1} and z_j and has permeability $\varkappa_j \mu_o$. The conductivity is σ. (It is straightforward to alter the equation derived below to accommodate free space below z_N instead of the semi-infinite slab. However, the semi-infinite slab is more convenient for our purposes.)

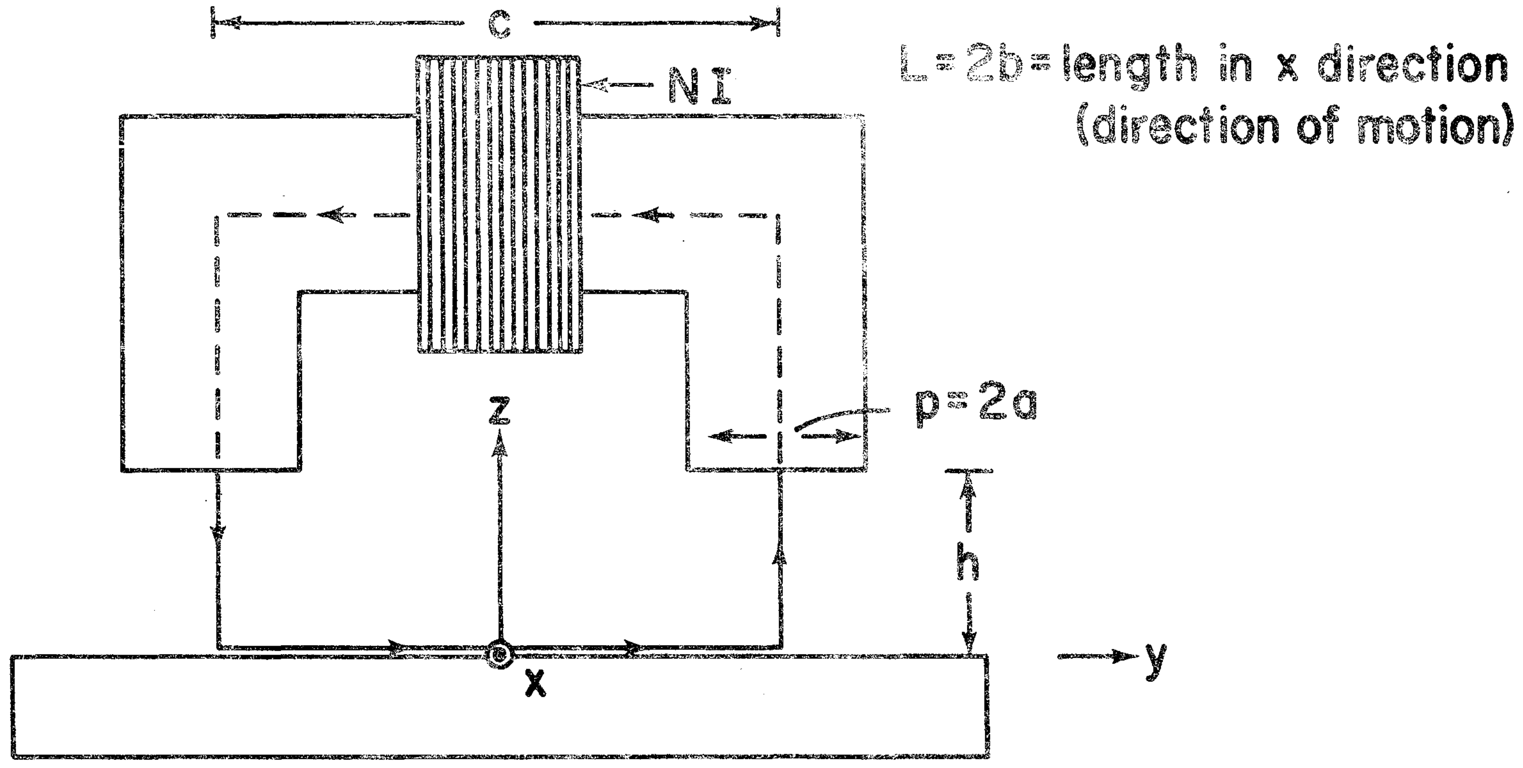

Fig. 2.1. Schematic diagram of electromagnetic (attractive) suspension and co-ordinate system.

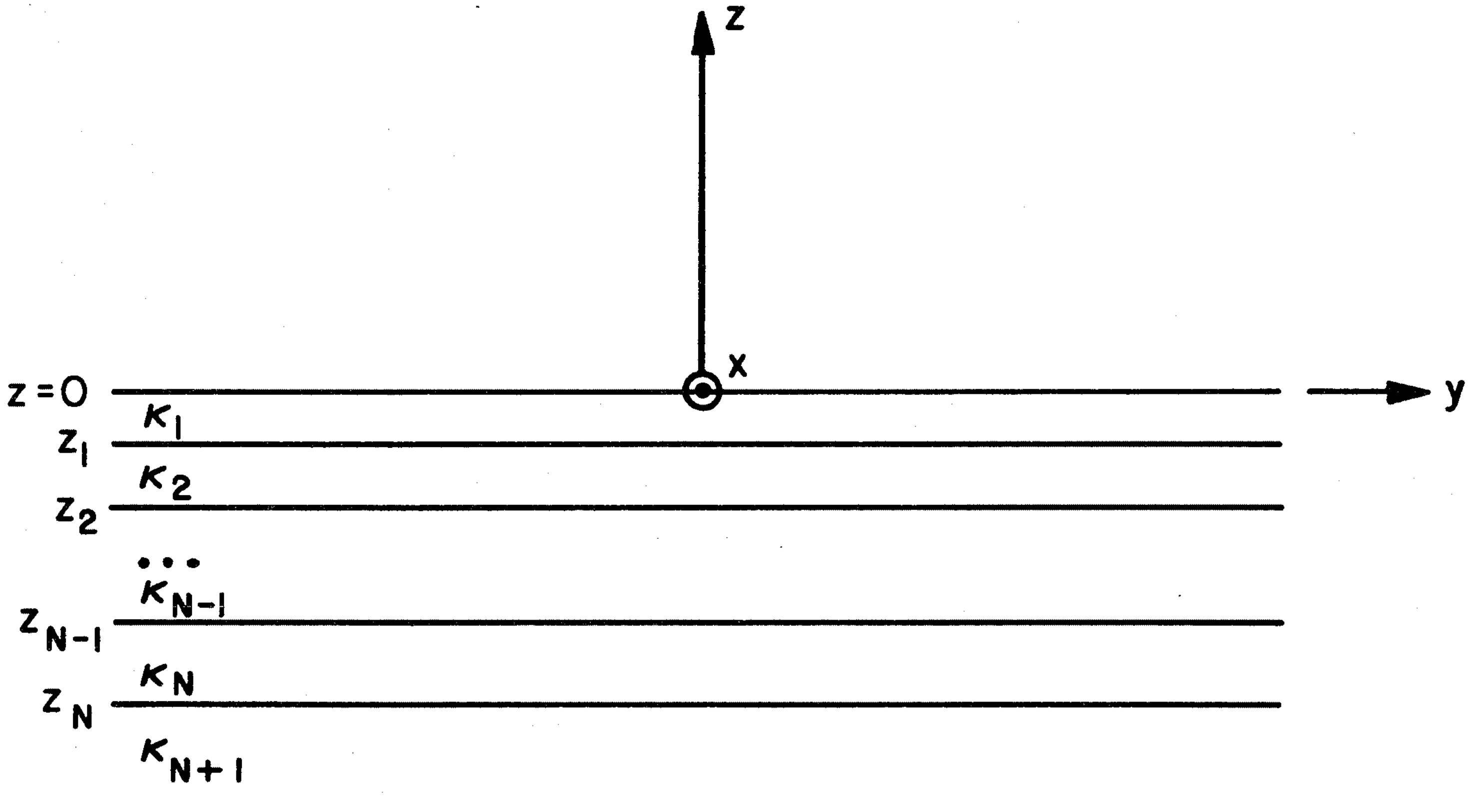

Fig. 2.2. Multi-layer track model.

In the $j^{\underline{th}}$ layer the field obeys

$$\nabla^2 \underline{B} = - \lambda_j \frac{\partial B}{\partial x} \qquad (z_{j-1} > z > z_j) \tag{2.2a}$$

where

$$\lambda_j = \mu_o \sigma v \varkappa_j \quad . \tag{2.2b}$$

In addition,

$$\nabla \cdot \underline{B} = 0 \tag{2.3}$$

and

$$\text{curl } \underline{B})_z = 0 \quad . \tag{2.4}$$

A single Fourier component of the field is

$$B_\gamma = b_{\gamma j} \; e^{\alpha_j (z-z_{j-1})} + c_{\gamma j} \; e^{-\alpha_j (z-z_{j-1})} \; \sin k_y y \; e^{ik_x x} , \quad \gamma = x,z, \tag{2.5a}$$

$$B_y = -b_{yj} \; e^{\alpha_j (z-z_{j-1})} + c_{yj} \; e^{-\alpha_j (z-z_{j-1})} \; \cos k_y y \; e^{ik_x x} \tag{2.5b}$$

where

$$\alpha_j = \sqrt{k^2 - i \; \lambda_j k_x} \equiv k \; \beta_j \tag{2.5c}$$

$$k^2 = {k_x}^2 + {k_y}^2 \quad . \tag{2.5d}$$

The $\nabla \cdot \underline{B} = 0$ and curl $\underline{B})_z = 0$ conditions require

$$b_{yj} = i \; k_y \; b_{xj}/k_x \quad , \qquad c_{yj} = i \; k_y \; c_{xj}/k_x \quad , \tag{2.6a}$$

and

$$b_{zj} = -i \; k \; b_{xj}/k_x \; \beta_j \; , \qquad c_{zj} = i \; k \; c_{xj}/k_x \; \beta_j \quad . \tag{2.6b}$$

If the magnet is confined to a region above $z = h$, then for $h > z > 0$

$$B_\gamma = (a_\gamma e^{-kz} + a'_\gamma e^{kz}) \sin k_y y \, e^{ik_x x} , \quad \gamma = x,z , \tag{2.7a}$$

and

$$B_y = -(a_y e^{-kz} + a'_y e^{kz}) \cos k_y y \, e^{ik_x x} \tag{2.7b}$$

where again the coefficients are related,

$$a_y = i\, k_y a_x / k_x , \qquad a'_y = i\, k_y a'_x / k_x , \tag{2.8a}$$

and

$$a_z = i\, k\, a_x / k_x , \qquad a'_z = -i\, k\, a'_x / k_x . \tag{2.8b}$$

For $z < z_N$,

$$B_\gamma = d_\gamma e^{\alpha_{N+1}(z-z_N)} \sin k_y y \, e^{i\, k_x x} , \quad \gamma = x,z \tag{2.9a}$$

and

$$B_y = -d_y e^{\alpha_{N+1}(z-z_N)} \cos k_y k \, e^{i\, k_x x} \tag{2.9b}$$

where

$$d_y = i\, k_y d_x / k_x \tag{2.9c}$$

and

$$d_z = -i\, k\, d_x / k_x \, \beta_{N+1} . \tag{2.9d}$$

Matching tangential components of $\underline{H}$ and the normal component of $\underline{B}$ across the boundaries gives:

$$a_x + a'_x = (b_{x1} + c_{x1}) / \kappa_1 , \tag{2.10a}$$

$$a_x - a'_x = (b_{x1} - c_{x1}) / \beta_1 , \tag{2.10b}$$

$$b_{xj} + c_{xj} = (\varkappa_j/\varkappa_{j-1})(b_{xj-1}\, e^{-\alpha_{j-1}d_{j-1}} + c_{xj-1}\, e^{\alpha_{j-1}d_{j-1}}),\ j = 2,3\ldots N \quad (2.10c)$$

$$b_{xj} - c_{xj} = (\beta_j/\beta_{j-1})(b_{xj-1}\, e^{-\alpha_{j-1}d_{j-1}} - c_{xj-1}\, e^{\alpha_{j-1}d_{j-1}}) \ , \quad (2.10d)$$

$$d_x = (\varkappa_{N+1}/\varkappa_N)(b_{xN}\, e^{-\alpha_N d_N} + c_{xN}\, e^{\alpha_N d_N}) \ , \quad (2.10e)$$

$$d_x = (\beta_{N+1}/\beta_N)(b_{xN}\, e^{-\alpha_N d_N} - c_{xN}\, e^{\alpha_N d_N}) \ , \quad (2.10f)$$

where

$$d_j = z_{j-1} - z_j \ . \quad (2.10g)$$

The first equation from each pair is from the continuity of H_x and the second is from the continuity of B_z, making use of the relationships between b_{zj} and b_{xj}, etc. The continuity of H_y gives nothing new.

We can write (in analogy to our previous work)

$$a'_x = -i\, W_1 \quad (2.11)$$

and

$$a_x = -\Gamma\, a'_x \quad (2.12)$$

where W_1 is some quantity related to the Fourier transform of the magnet current distribution (see next section) and Γ characterizes the track. It depends upon the track parameters, the velocity, and the wave vector components k_x and k_y. It does not depend upon the magnet current distribution (except that we have assumed a certain symmetry about $y = 0$).

Further we write

$$\Gamma = f_1 \tag{2.13a}$$

$$b_{xj} = i W_1 f_{2j}, \qquad j = 1,2 \ldots N \tag{2.13b}$$

$$c_{xj} = i W_1 f_{2j+1} , \tag{2.13c}$$

and

$$d_x = i W_1 f_{2N+2} . \tag{2.13d}$$

The f_m depend upon v, k_x, k_y and the track parameters but are independent of the magnet current distribution. The matching equations can be rewritten as

$$\varkappa_1 f_1 - f_2 - f_3 = \varkappa_1 \tag{2.14a}$$

$$-\beta_1 f_1 - f_2 + f_3 = \beta_1 \tag{2.14b}$$

$$- P_j f_{2j-2} - Q_j f_{2j-1} + f_{2j} + f_{2j+1} = 0 \qquad j = 2,3 \ldots \tag{2.14c}$$

$$- R_j f_{2j-2} + S_j f_{2j-1} + f_{2j} - f_{2j+1} = 0 \tag{2.14d}$$

$$- P_{N+1} f_{2N} - Q_{N+1} f_{2N+1} + f_{2N+2} = 0 \tag{2.14e}$$

$$- R_{N+1} f_{2N} + S_{N+1} f_{2N+1} + f_{2N+2} = 0 , \tag{2.14f}$$

where

$$P_j = \varkappa_j e^{\varphi_{j-1}} / \varkappa_{j-1} , \tag{2.14g}$$

$$Q_j = \varkappa_j e^{-\varphi_{j-1}} / \varkappa_{j-1} , \tag{2.14h}$$

$$R_j = \beta_j e^{\varphi_{j-1}} / \beta_{j-1} , \tag{2.14i}$$

$$S_j = \beta_j e^{-\varphi_{j-1}} / \beta_{j-1} , \tag{2.14j}$$

and

$$\varphi_j = -\alpha_j d_j \quad . \tag{2.14k}$$

This gives 2N+2 equations in 2N+2 unknowns (the f_m), which are solved numerically on the computer by standard means for large N or can be solved analytically for small N.

Adding all components of the fields gives, e.g.,

$$B_x = 2 \, \mathrm{Re} \int_0^\infty dk_x \int_0^\infty dk_y (b_{xj} \, e^{\alpha_j(z-z_{j-1})} + c_{xj} \, e^{-\alpha_j(z-z_{j-1})} \sin k_y y \; e^{i k_x x} \; , \tag{2.15}$$

$$z_{j-1} > z > z_j \quad .$$

The other components have similar equations.

To find the self-consistent values of κ_j, we must make an initial guess for the κ_j's, calculate the magnetic fields in the track and then compute the κ_j from the new fields, and start the process all over again. Several iterations are required to obtain self consistency. For a given $\kappa(H)$ curve describing the track, then

$$\kappa_j = \kappa(H_j) \tag{2.16}$$

where H_j is the field at some representative point in the jth layer. The point we have chosen is $x = 0$, $y = c/2$, $z = z_{j-1}$, i.e.,

$$H_j = H_y(0, c/2, z_{j-1}) \quad . \tag{2.17}$$

The plane $x = 0$ represents an average of the x-dependence of the field, whereas $y = c/2$ gives the best fit to the experimental data. Originally, we thought $y = 0$ would be the best point but this gave too conservative results. To make sure that we adequately treat the saturation problem with a limited number of layers, we take $z = z_{j-1}$, i.e., the top of the layer instead of any point further down. This may be conservative, but appears to be adequate for our purposes.

2.1.2 Magnet Model

The model of the magnet that we have found useful is shown in Fig. 2.3. We concentrate solely on the magnetization since the real ampere-turns contribute little directly to the forces or fields. The magnetization is assumed to be uniform in the x (direction of motion) and z (vertical) directions. The poles are taken to be infinitely high and the real ampere-turns are assumed to be at infinity. The model of Task II corresponded to $M_z(y)$ = constant over the width of the pole. (See Sec. 3.1 of reference 1.) In this section we introduce a non-uniform $M_z(y)$. ($M_z = 0$ for $|x| > b$ and for $h > z$.) The precise form of $M_z(y)$ will be discussed at the end of this section. The volume magnetization currents are

$$\underline{J} = \text{curl } \underline{M} \tag{2.18}$$

$$J_x = \frac{dM_z(y)}{dy} , \quad |x| < b, \quad z > h \tag{2.19a}$$

$$= 0, \qquad \text{otherwise.} \tag{2.19b}$$

Consider a region of width $\delta z'$ at $z = z'$, the magnetization current $i_x = J_x \delta z'$ gives rise to a field in the region $z < z'$, whose y component is (See Eq. (2.7b))

$$\delta B_y = -\int_{-\infty}^{\infty} dk_x \int_0^{\infty} dk_y \, \delta a_y' \, e^{kz} \cos k_y y \, e^{ik_x x} \quad . \tag{2.20}$$

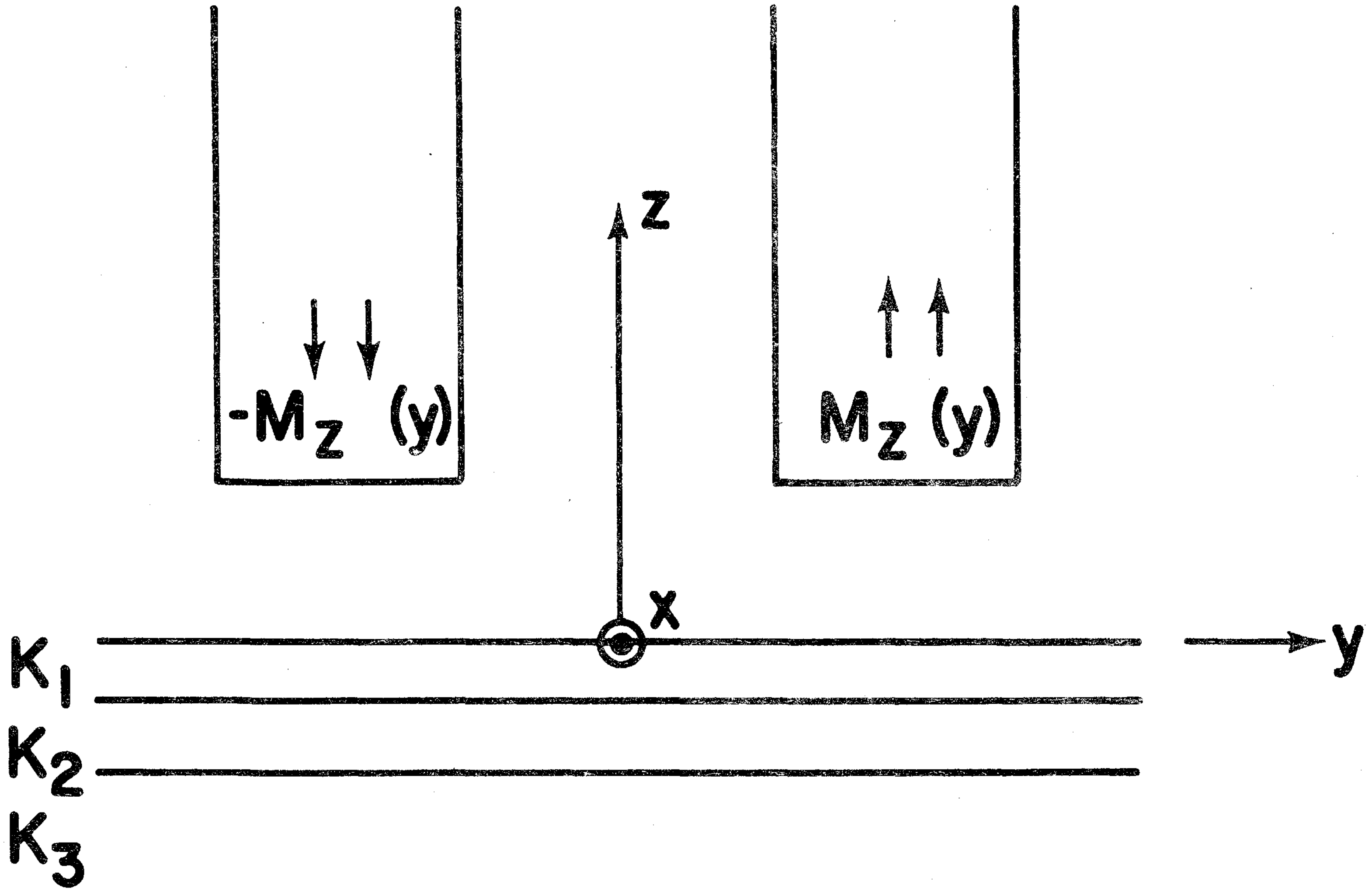

Fig. 2.3. Magnetization and track model.

From Ampere's Circuital Law ($\oint \underline{B}\cdot d\ell = \mu_o I$) and the odd symmetry of δB_y about $z = z'$,

$$\delta B_y(z=z' - 0) = \frac{\mu_o}{2} J_x \, \delta z' \quad . \tag{2.21}$$

From Eqs. (2.19) and (2.20) we find

$$\delta a_y' = -\frac{\mu_o}{\pi^2} e^{-kz'} \delta z' \frac{\sin k_x b}{k_x} \int_o^\infty dy \cos k_y y \frac{dM_z(y)}{dy} \quad . \tag{2.22}$$

Integrating by parts gives

$$\delta a_y' = -\frac{\mu_o}{\pi^2} e^{-kz'} \delta z' \frac{\sin k_x b}{k_x} k_y \int_o^\infty dy \sin k_y y \, M_z(y) . \tag{2.23a}$$

Summing all contributions from $z' > h$ gives

$$a_y' = -\frac{\mu_o e^{-kh}}{\pi^2 k} \frac{\sin k_x b}{k_x} k_y \int_o^\infty dy \sin k_y y \, M_z(y) \tag{2.23b}$$

From Eqs. (2.8a) and (2.11), we find

$$W_1 = \frac{k_x}{k_y} a_y' \tag{2.24a}$$

$$= -\frac{\mu_o e^{-kh}}{\pi^2 k} \sin k_x b \int_o^\infty dy \sin k_y y \, M_z(y) \quad . \tag{2.24b}$$

A straightforward integration of Maxwell's Stress Tensor over the surface of the track ($z = +0$) gives the lift and drag forces on the magnet:

$$F_L = \frac{8\pi^2}{\mu_o} \int_o^\infty dk_x \int_o^\infty dk_y \frac{k^2 |W_1|^2}{k_x^2} \mathrm{Re}\Gamma \tag{2.25a}$$

and

$$F_D = \frac{8\pi^2}{\mu_o} \int_o^\infty dk_x \int_o^\infty dk_y \frac{k |W_1|^2}{k_x} \mathrm{Im}\Gamma \quad , \tag{2.25b}$$

where Γ is obtained from Eq. (2.13a) and the solution of the set of linear equations (2.14).

For N = 2 (i.e., the track composed of two finite layers plus an infinitely thick layer on the back), it can be shown that

$$\Gamma = \frac{(1-\gamma)\kappa_1 + (1+\gamma)\kappa_1}{(1-\gamma)\kappa_1 + (1+\gamma)\beta_1} \tag{2.26a}$$

where $$\gamma = -\gamma_1/\gamma_2, \tag{2.26b}$$

$$\gamma_1 = P_2(Q_3 + S_3 + P_3 - R_3) - R_2(Q_3 + S_3 - P_3 + R_3) \ , \tag{2.26c}$$

$$\gamma_2 = Q_2(Q_3 + S_3 + P_3 - R_3) + S_2(Q_3 + S_3 - P_3 + R_3) \ . \tag{2.26d}$$

The other quantities are defined by Eq. (2.14).

The form of the magnetization used in this study is (the width of the pole face is p = 2a)

$$M_z(y) = M_1(y_1), \quad y > 0 \quad . \tag{2.27a}$$

where $$y_1 = y-c/2 \ , \tag{2.27b}$$

$$M_1(y_1) = M_o \ , \ 0 < y_1 < a_1 \tag{2.27c}$$

$$= M_o \ [1+\alpha(y_1-a_1)], \quad a_1 < y_1 < a \tag{2.27d}$$

$$= 0 \ , \qquad y_1 > a \tag{2.27e}$$

$$M_1(-y_1) = M_1(y_1) \quad . \tag{2.27f}$$

Also, by symmetry

$$M_z(-y) = -M_z(y) \quad . \tag{2.28}$$

The shape of the magnetization is taken to be velocity independent. The magnetization is pictured in Fig. 2.4 for $a_1 = 0.5a$ and $\alpha = 5/a$, the values used for all computations shown in the text of this report.* This justification of such a peaked magnetization rests upon several pieces of information. First of all, the magnetic field near the pole face is experimentally observed to be peaked near the edges. This implies a peaked magnetization. In Fig. 2.5 we show the measured magnetic field and the calculated one for different positions in the gap. The zero in the vertical direction has been shifted for each curve for clarity and hence is arbitrary. Actual magnitudes all were within 10% of one another along a vertical line directly under the pole center. Due to the finite thickness of the Hall probe used to measure the experimental points, the exact position in the gap is not known. Hence, the agreement between theory and experiment is considered satisfactory.

Second, in order to obtain the proper lift force for a given NI (we relate the magnitude of the magnetization to real-ampere turns in the next section), we must have considerably higher flux at the edges. Incidentally, the simple model based upon magnetic circuits described in Sec. 3.2 of Reference 1 assumes uniform flux across the pole face. It underestimates the lift substantially which is somewhat surprising.

---

* The simple form for the magnetization, Eq. (2.27), was chosen for convenience. The specific values for a_1 and α are the result of a parameter study to reproduce field shapes in the gap and the force level of the experimental magnet. These values also made the contour integral, Eq. (2.30), approximately independent of path.

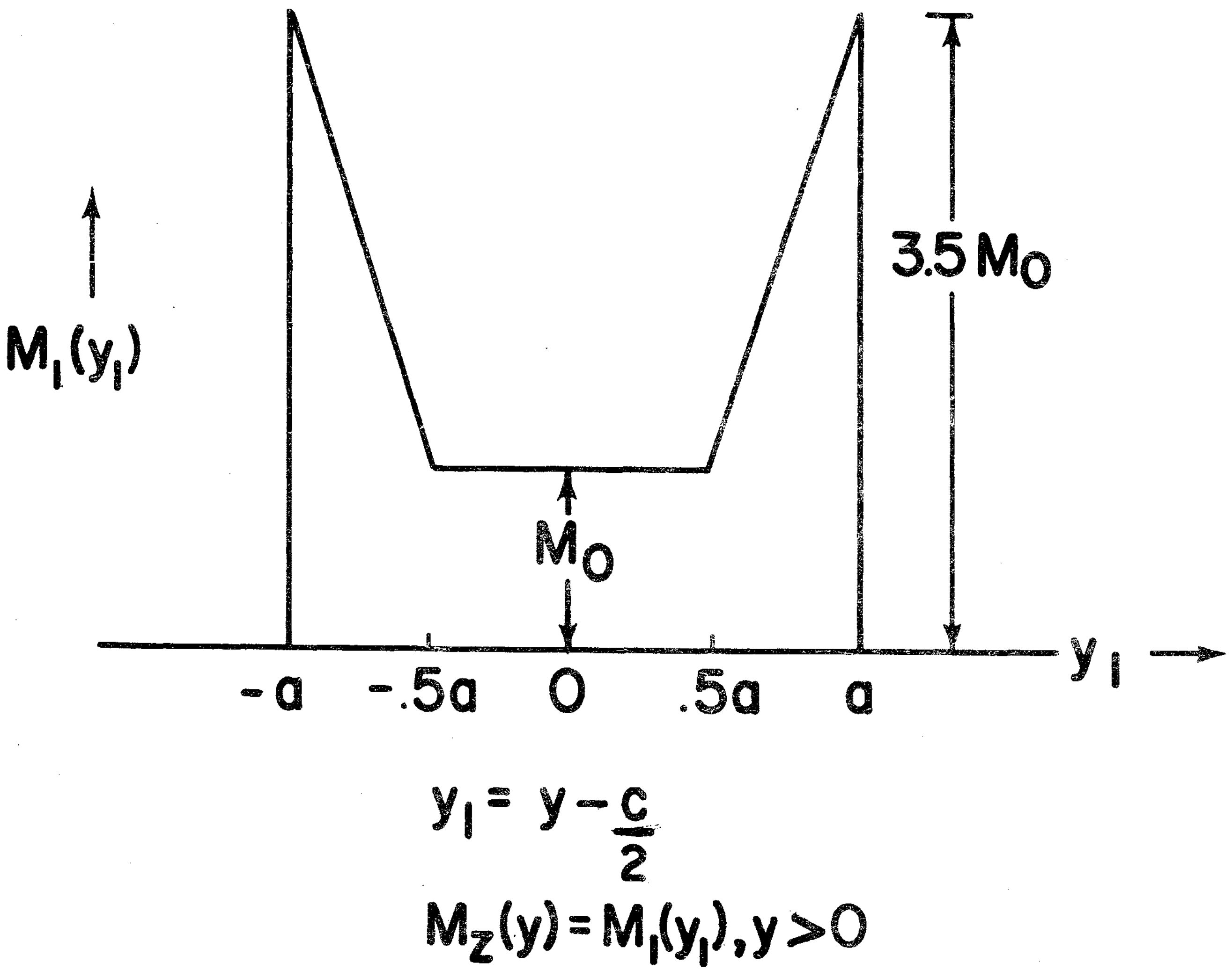

Fig. 2.4. Magnetization $M_z(y)$ for one pole.

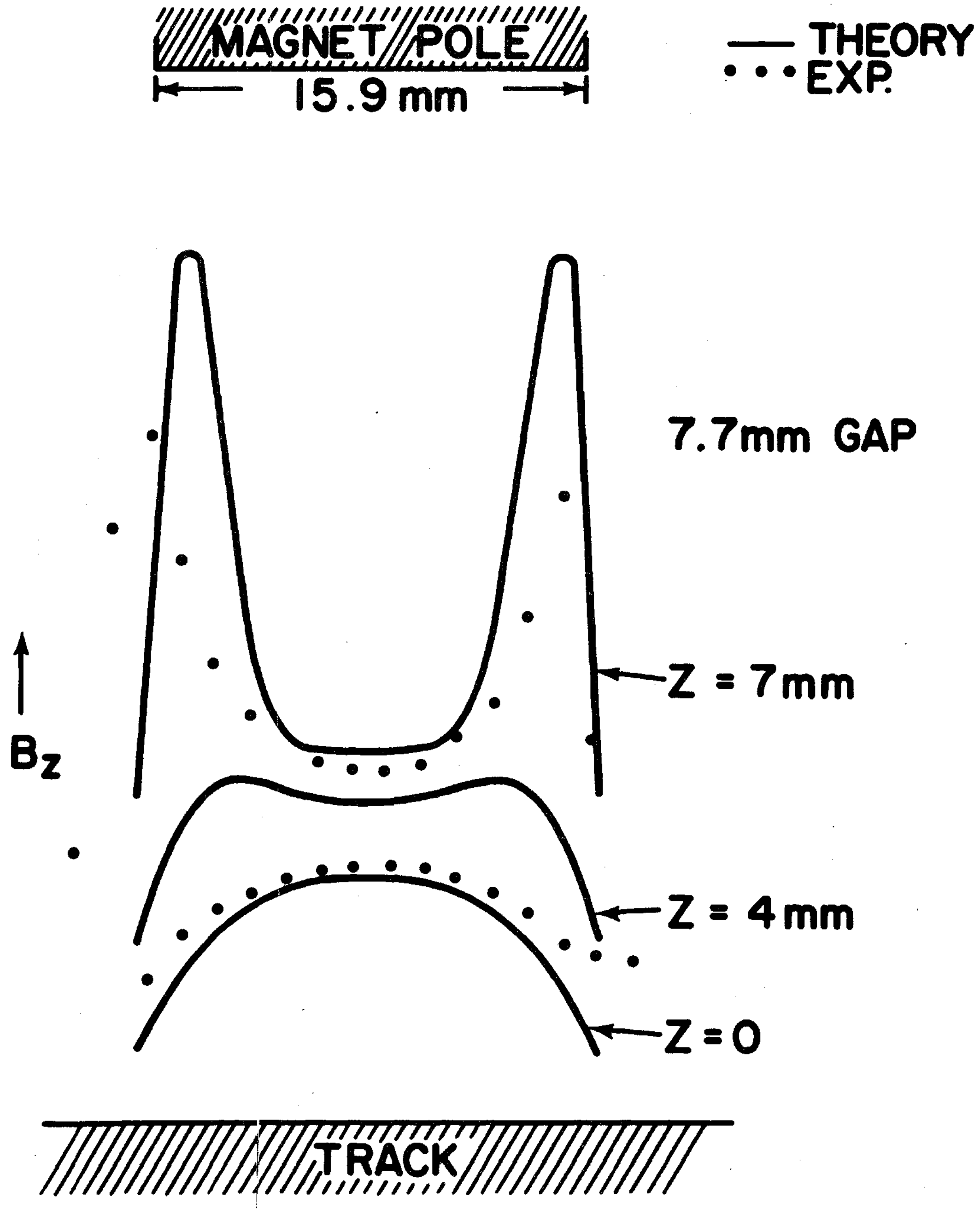

Fig. 2.5. Normal component of the magnetic field in the gap near the magnet center (x = 0). Ordinate is arbitrary for each curve. The velocity is v = 0 and z is measured from the top of the track.

Third, in Appendix A, we describe a two-dimensional model approximately valid for $v = 0$. In that model, $M_z(y)$ can be computed on the basis of requiring certain paths to have equal drop in magnetomotive force. The $M_z(y)$ calculated is quite similar to the one shown in Fig. 2.4. The one shown was chosen for convenience and because it reproduced the experimental data reasonably well.

For the magnetization given by Eq. (2.27), W_1 becomes (see Eq. (2.24b))

$$W_1 = -\frac{2\mu_o}{\pi^2} M_o \frac{\sin k_x b}{k} e^{-kh} \frac{\sin k_y c/2}{k_y} \Big[\sin k_y a \, [1+\alpha(a-a_1)] + \frac{\alpha}{k_y} [\cos k_y a - \cos k_y a_1]\Big] \quad . \tag{2.29}$$

2.1.3 Relationship Between Magnetization and Real Ampere-Turns

In our discussion of the electromagnetic system thus far, the parameter describing the strength of the magnetic field has been M_o which gives the magnitude of the magnetization. It is more convenient to know the real ampere-turns of the magnet windings. So we now find a relationship between the two.

Consider Fig. 2.1 where a model of the magnet is shown. If we integrate $\underline{H}$ around the contour shown, we have according to Ampere's circuital law

$$\oint \underline{H} \cdot \underline{d\ell} = -NI \quad . \tag{2.30}$$

(The minus sign is just a convention.) The portion of the contour which is dashed is through the magnet core and is related to the reluctance of the core R_c by

$$\int_{\substack{\text{dashed}\\\text{contour}}} \underline{H}\cdot \underline{d\ell} = H_c \ell_c = \frac{\Phi_c \ell_c}{\mu_c A_c} \tag{2.31a}$$

$$= \Phi_c R_c \tag{2.31b}$$

where ℓ_c is the length of core, μ_c is the permeability, A_c is the cross-sectional area, and Φ_c is the flux through the core. Usually it is a good approximation to neglect R_c in comparison to the reluctance of the rest of the magnetic circuit. Typically, the neglected portion may be $\lesssim 10\%$ of the remaining part unless the core is saturated where it would be higher. The error made in neglecting this term is more than compensated for by the fact that the model tends (even with the peaking of the magnetization) to underestimate the lift force. Hence,

$$-NI = \int_{\substack{\text{solid}\\\text{contour}}} \underline{H}\cdot d\ell = \frac{2}{\mu_o}\int_0^{c/2} B_y(0,y,+0)\,dy + \frac{2}{\mu_o}\int_0^h B_z(0,c/2,z)\,dz \tag{2.32}$$

The contribution from the left-hand side of the circuit equals that of the right-hand side due to the symmetry of the problem, so we obtain the factor of 2 in the equation above. We have chosen x = 0 and the path indicated for convenience.

From the equations for the magnetic field in the region $h > z > 0$, (Eqs. (2.7), (2.8), (2.11); and (2.12)) it can be seen that

$$\int_0^{c/2} B_y(0,y,+0)\,dy = 2\,\mathrm{Re}\int_0^{\infty} dk_x \int^{\infty} dk_y[-(a_y+a_y')]\,\frac{\sin k_y c/2}{k_y} \tag{2.33}$$

and

$$\int_o^h B_z(0,c/2,z)dz = 2\ \mathrm{Re}\int_o^\infty dk_x \int_o^\infty dk_y \left[-a_z(e^{-kh}-1)/k + a_z'(e^{kh}-1)/k\right] \sin k_y c/2 \quad . \qquad (2.34)$$

Substituting into the equation above the expressions for a_y, a_y', a_z and a'_z, we find that

$$\int_o^{c/2} B_y\, dy + \int_o^h B_z dz = 2\ \mathrm{Re} \int_o^\infty dk_x \int_o^\infty dk_y \ \sin k_y c/2 (W_1/k_x)(\Gamma\ e^{-kh} - e^{kh}) \qquad (2.35)$$

where W_1 and Γ have been given previously.

The final expression is

$$NI = \frac{4}{u_o}\ \mathrm{Re} \int_o^\infty dk_x \int_o^\infty dk_y \ \sin k_y\ c/2\ (W_1/k_x) e^{kh}\ (1-e^{-2kh}\ \Gamma) \quad . \qquad (2.36)$$

2.1.4 Field and Eddy-Current Mapping

Prior to developing the present model, detailed maps of the field and eddy current distributions in the track were obtained for the model of reference 1, Sec. 3.1 (M_z (y) = constant and track with uniform permeability). Although the numerical values will be somewhat different for the newer model, the general features will remain the same. The results are contained in Appendix B. The principal conclusion drawn was that the fields and the eddy currents extend beyond the ends of the magnet a considerable distance. The eddy currents also extend out laterally if they are not confined by a track of finite width. Additional field distributions from a different model are shown in Sec. 2.2.1.

2.1.5 Prediction of High-Speed Performance

Using the model described in the Sections (2.1.1)-(2.1.3), we calculated the performance of full-scale magnets up to speeds of 134 m/s. In Figs. 2.6-2.9, we take $b = 0.5$ m (i.e., the magnet length is 1 m). In Figs. 2.10 and 2.11, various lengths are displayed. In all calculations $a = 2$ cm($p = 4$cm), $c = 18$ cm, and $h = 1.5$ cm. The steel is taken to be unannealed 1020 steel with $\rho = 13.25 \mu\Omega$-cm and a B-H curve as shown in Fig. 2.12. The track was divided into two layers plus an infinitely thick backing. Since the skin depth at 134 m/s is roughly 5 mm, the layer thicknesses were chosen to be 5 mm. Results for more layers of different thicknesses are not significantly different. The self-consistent values of κ_1 are shown in Table 2.1 for different force levels and magnet lengths.

The gap field (normal field) at $v = 0$ along a vertical line under the center of a pole is

$$B_z = 0.44\mathrm{T} \times 10^{-4}\ NI \quad . \tag{2.37}$$

For 10 kN of lift force, $NI = 1.23 \times 10^4$, so $B_z = 0.54$T. The field increases somewhat with increasing velocity for fixed lift force. For example, at $v = 134$ m/s, $B_z = 0.63$T for 10 kN of lift force.

The lift force as a function of magnet current (ampere-turns) is shown in Fig. 2.6 for different speeds. At $v = 0$, the force is quadratic in NI, however, at high speeds the force varies less rapidly with NI due to the saturation of the steel track. For high enough current levels the magnet core will also saturate but this is not included in this model. It is assumed that the magnet will be designed to eliminate core saturation in the region of interest.

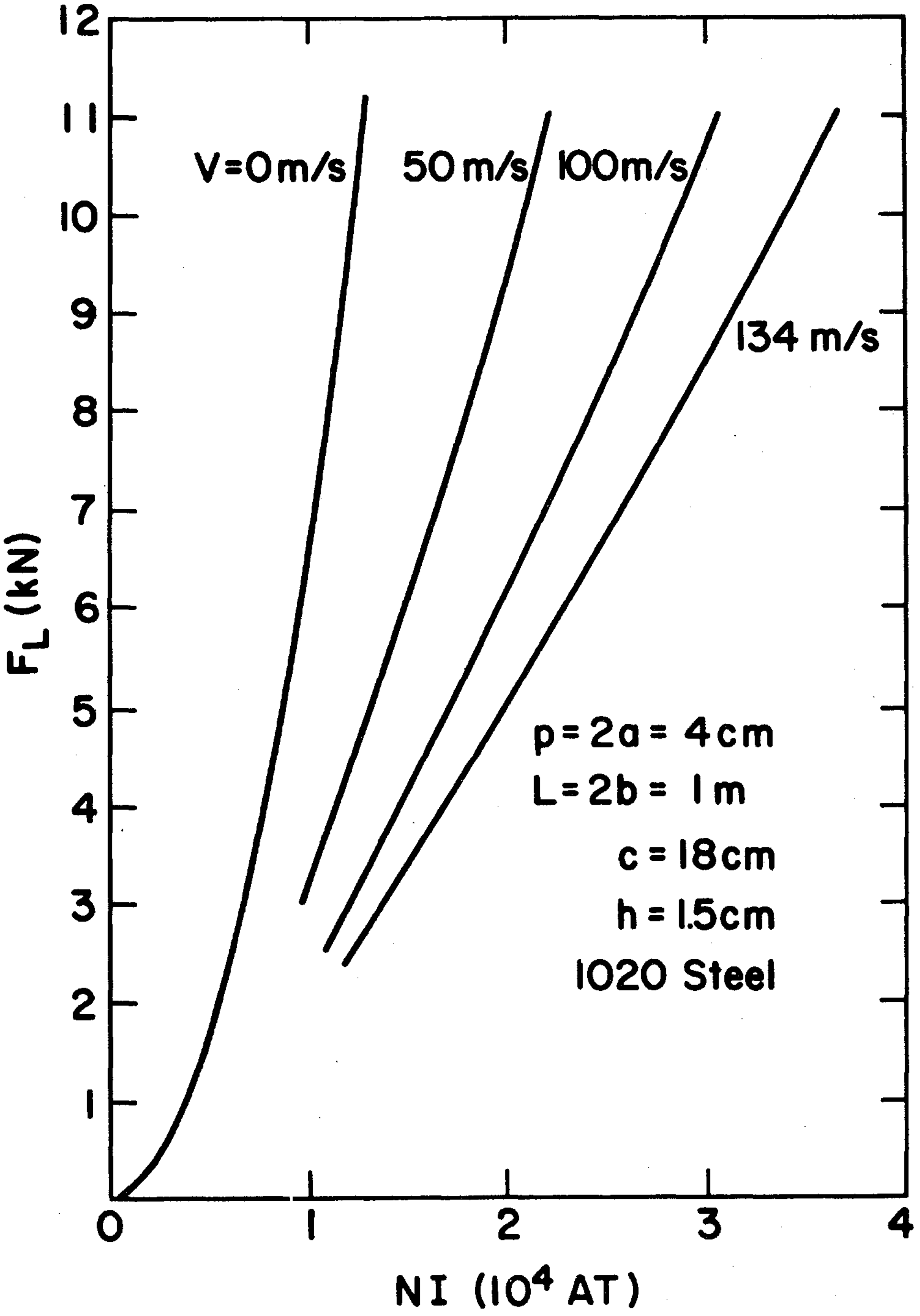

Fig. 2.6. Lift force vs. ampere-turns (MMF) for v = 0, 50, 100, and 134 m/s. The magnet length is 1 meter.

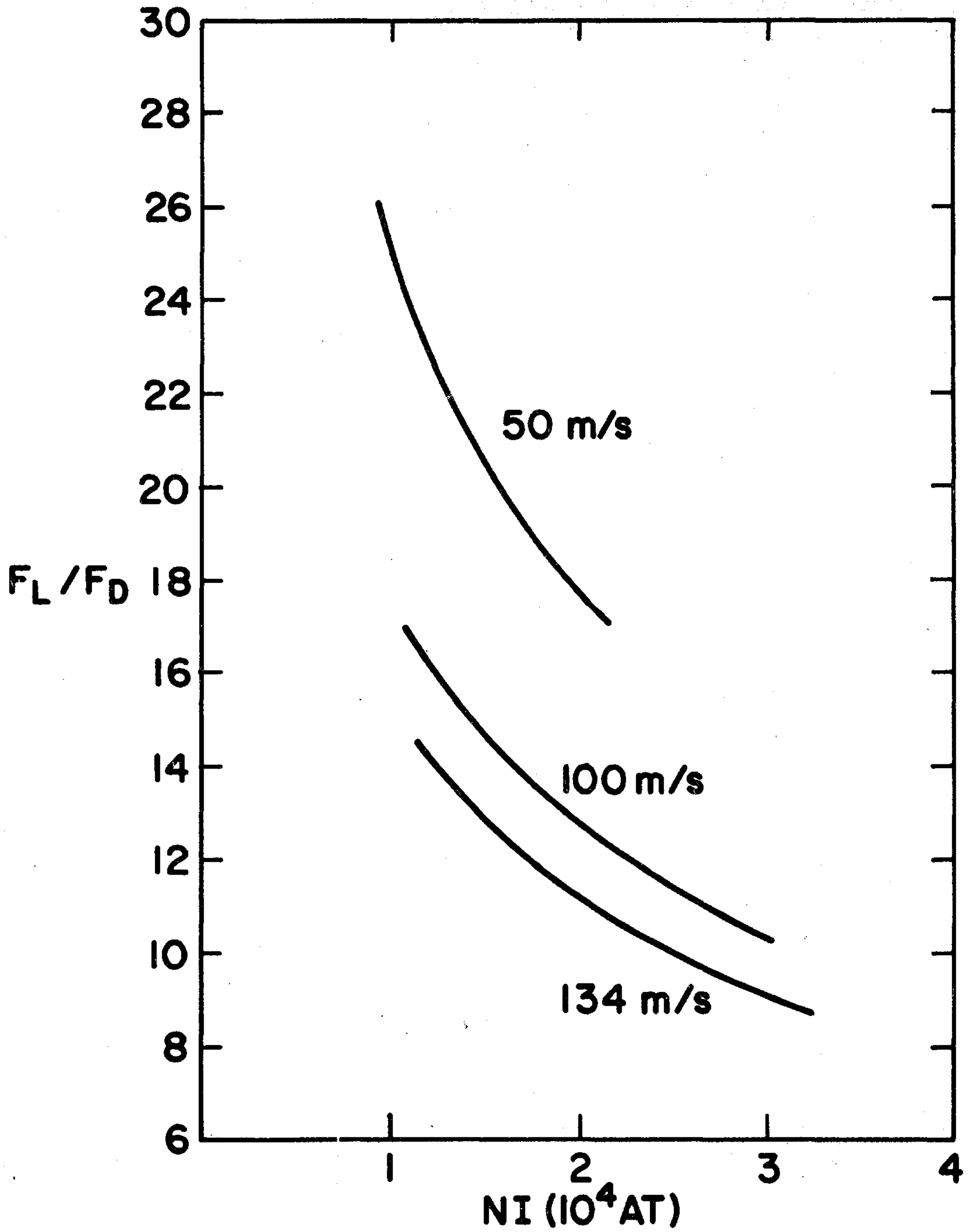

Fig. 2.7. Lift-to-drag ratio vs. ampere-turns (MMF) for v = 50, 100, and 134 m/s. Parameters are the same as in Fig. 2.6.

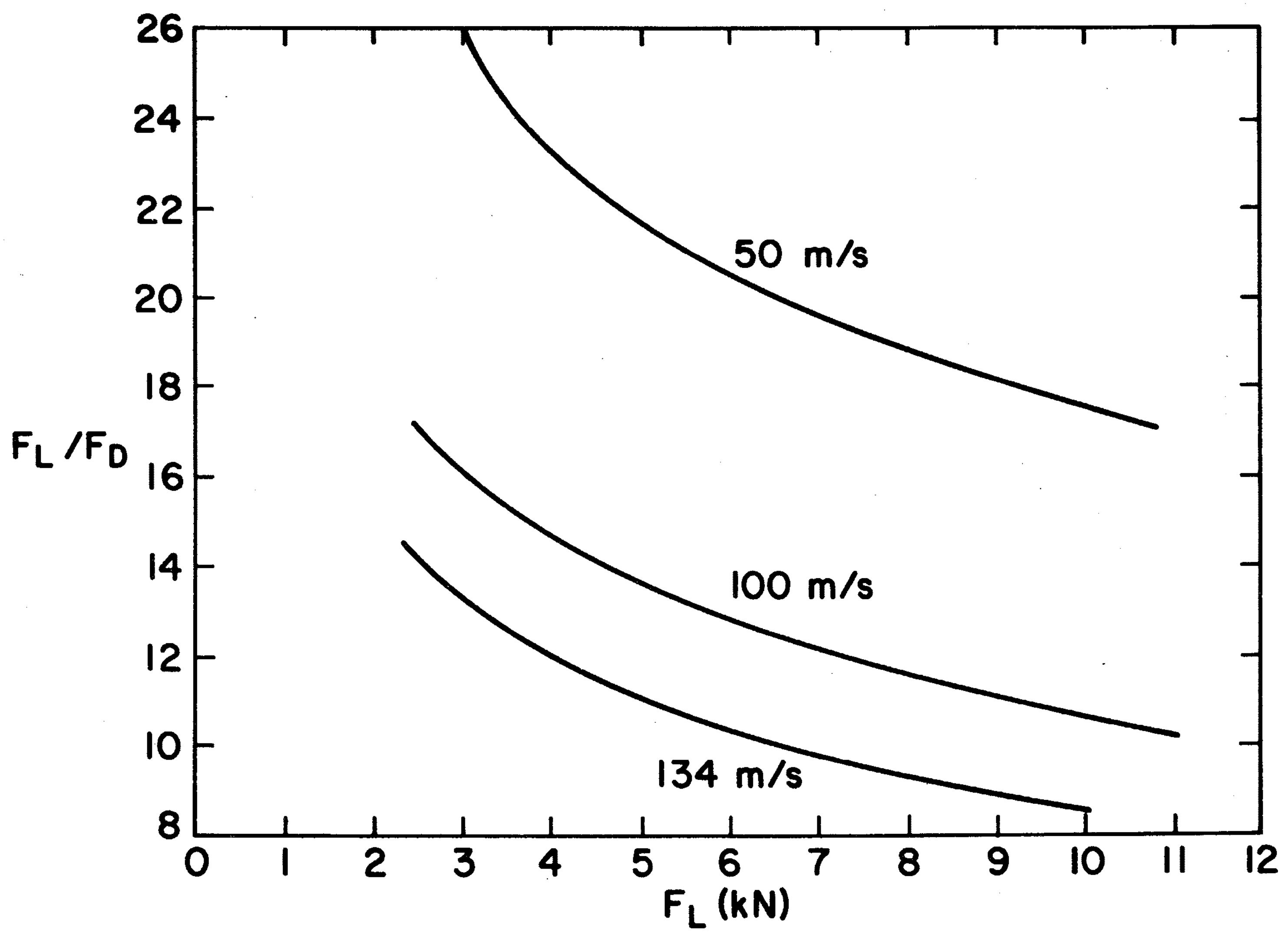

Fig. 2.8. Lift-to-drag ratio vs. lift force for v = 50, 100, and 134 m/s. Parameters are the same as in Fig. 2.6.

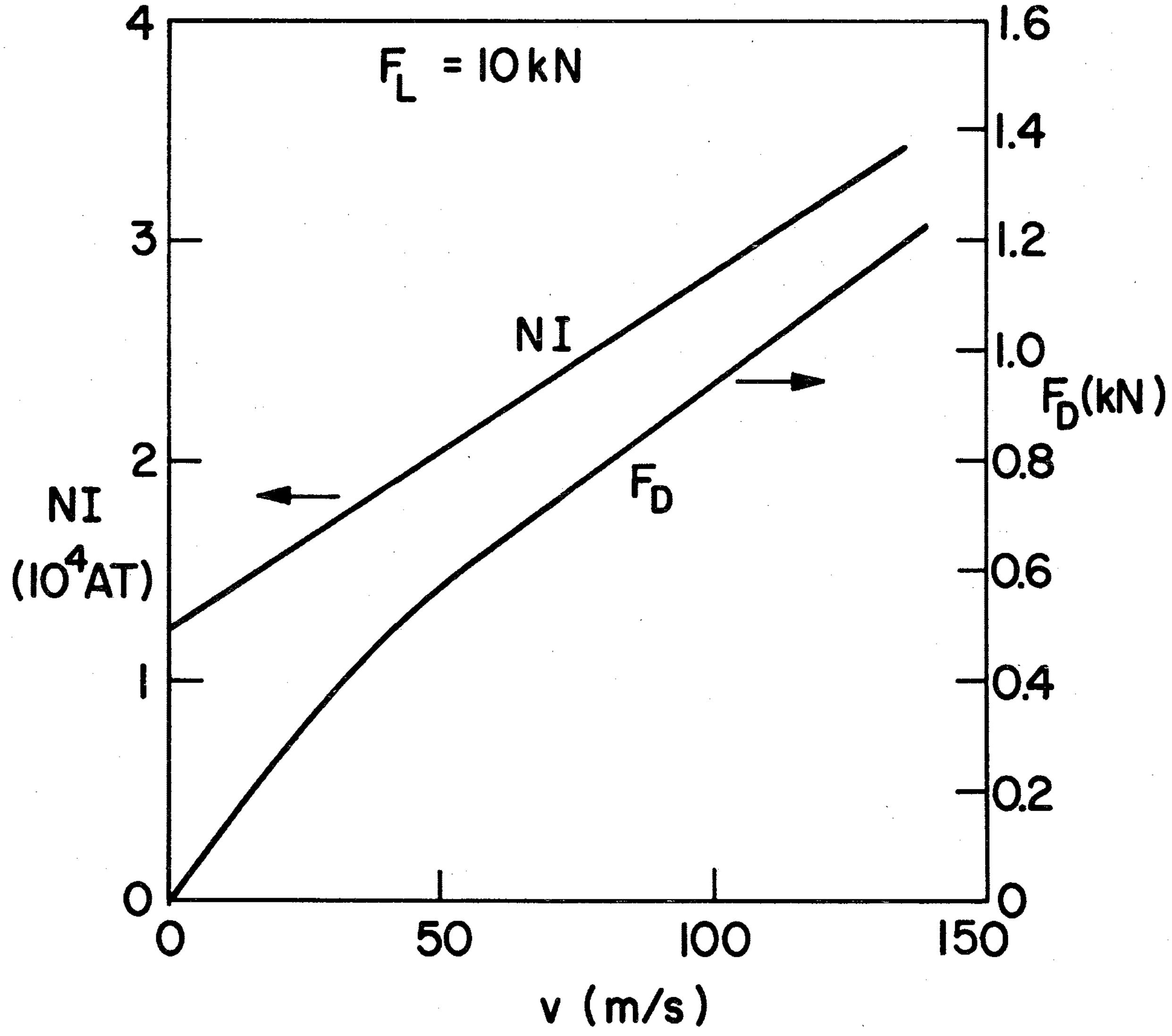

Fig. 2.9. Current and drag force vs. speed for 10 kN of lift. Parameters are the same as in Fig. 2.6.

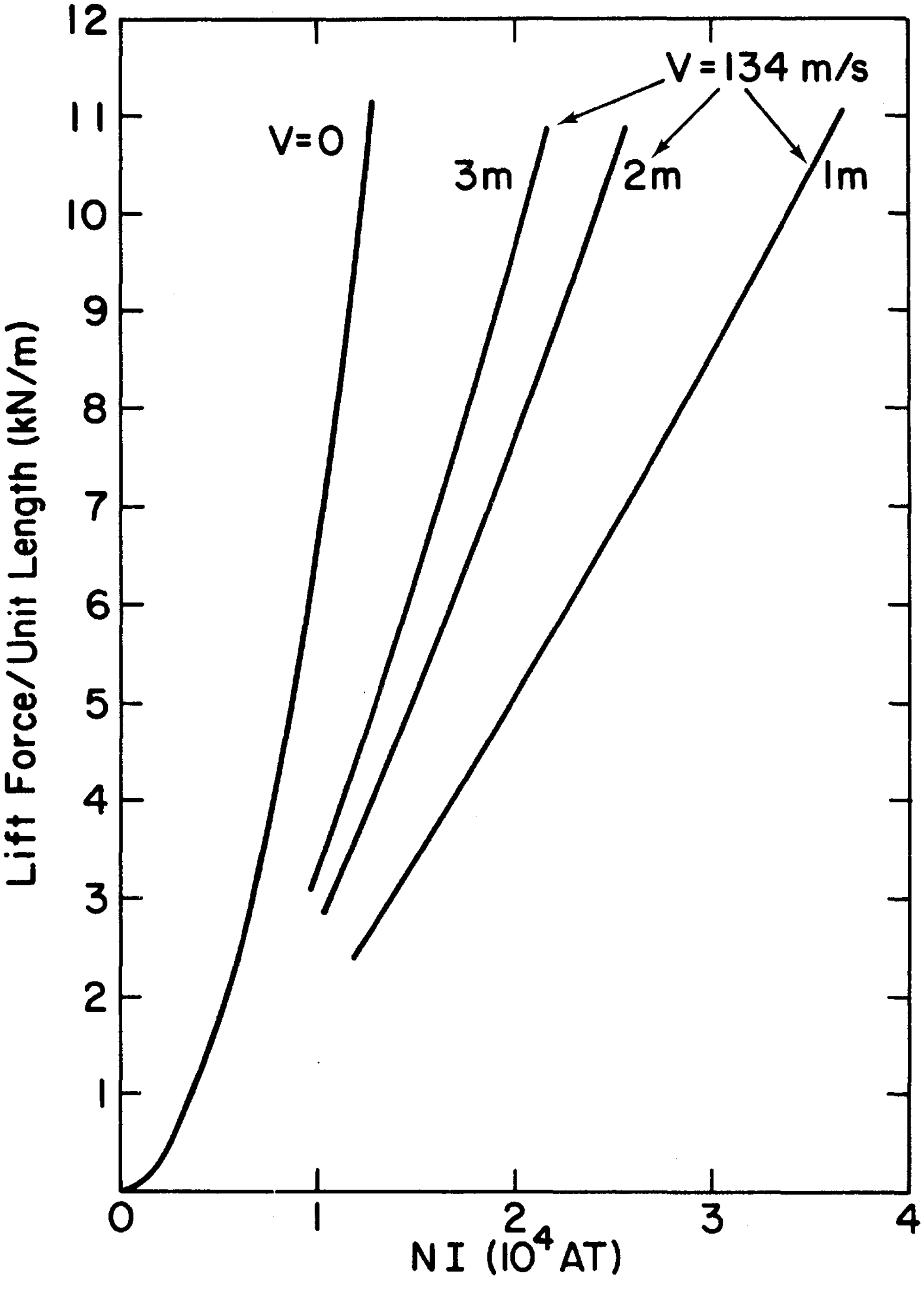

Fig. 2.10. Lift force/unit length vs. NI at v = 0 and 134 m/s for magnet length L = 1, 2, and 3 m. At v = 0, all lengths have approximately the same lift force/unit length. Other parameters are the same as in Fig. 2.6.

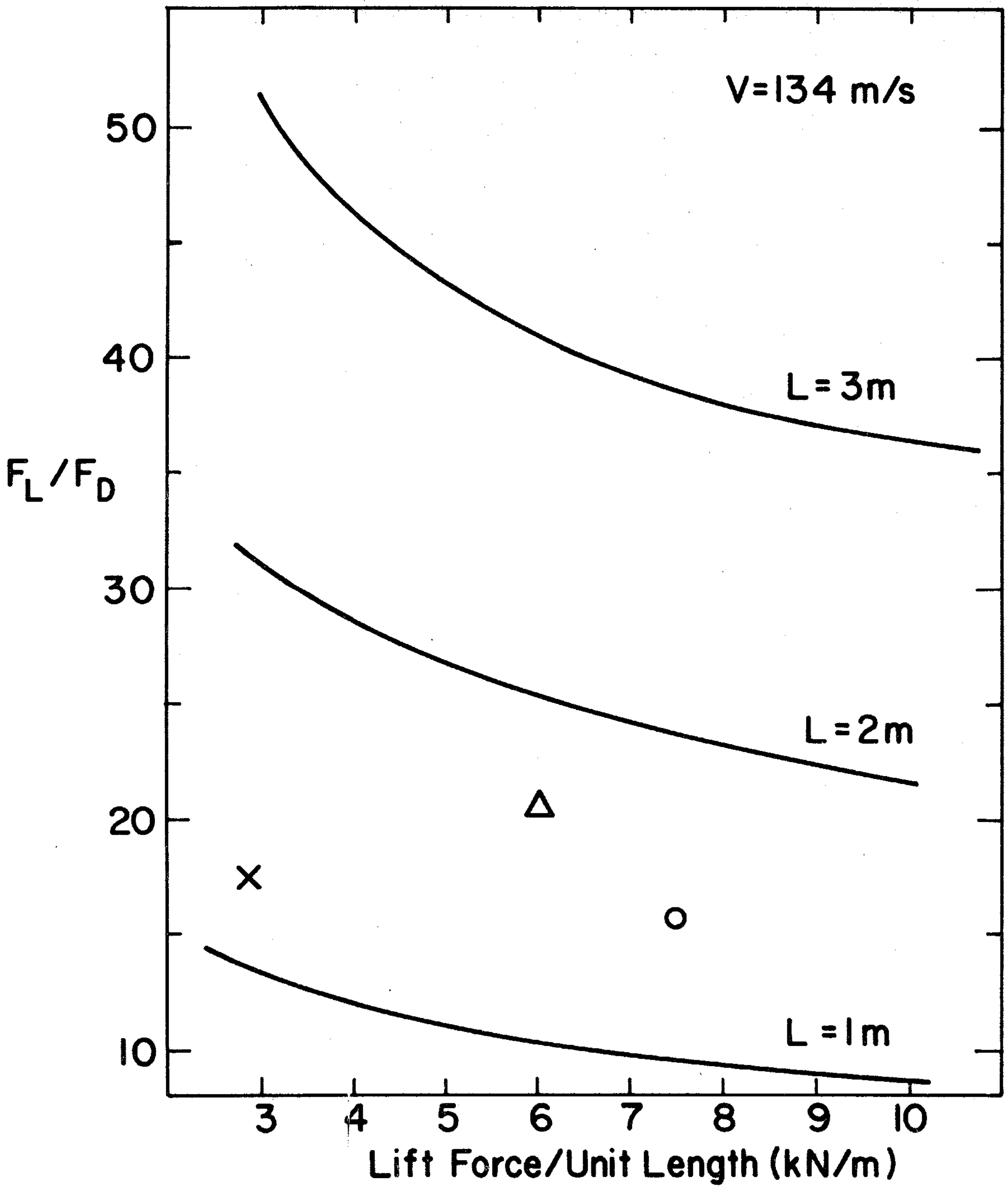

Fig. 2.11. Lift-to-drag ratio vs. lift force/unit length for L = 1, 2, and 3 m. Other parameters are the same as in Fig. 2.6. ×, Δ and O are explained in Section 2.3.4.

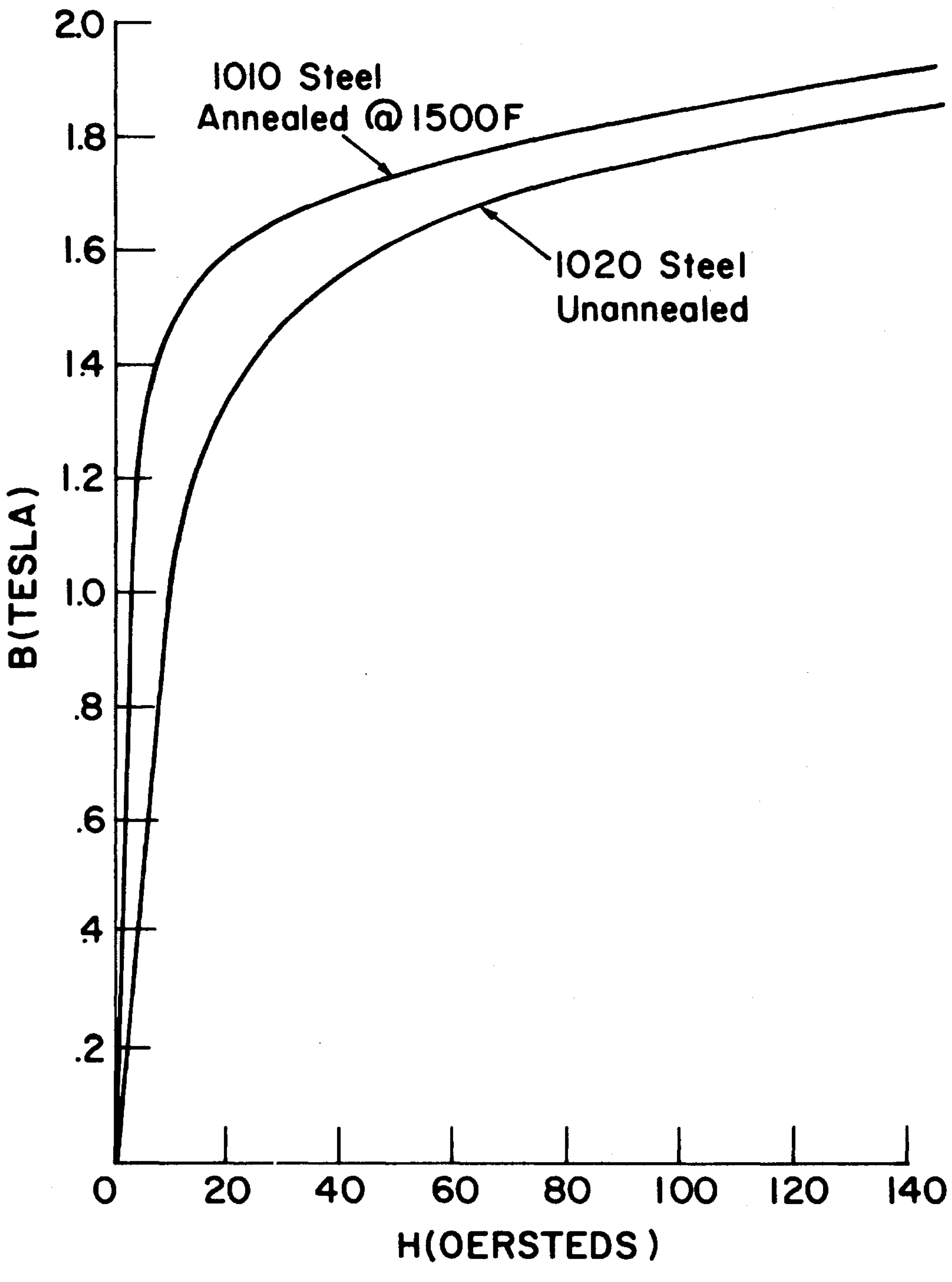

Fig. 2.12. B-H curve for 1010 and 1020 steel.

A typical operating condition would be $F_L = 10$ kN. At $v = 0$, $NI = 1.23 \times 10^4$ AT for this amount of lift. To achieve the same lift at $v = 134$ m/s, $NI = 3.40 \times 10^4$ AT--a substantial increase. This level of force requires approximately 25 magnets on each side of the vehicle for lift. Higher forces can be obtained from the magnets by increasing the current, but the nominal operating point must be well away from the maximum force attainable. For example, if required this magnet should be able to furnish 20 kN at 2.0 cm gap in order to overcome an irregularity in the track or some other perturbation.

In Fig. 2.7, the lift-to-drag ratio is plotted against NI for different speeds. As NI increases for fixed speed, the fields increase causing the permeabilities to drop. This causes the lift-to-drag ratio to drop. We note that for 134 m/s $F_L/F_D = 8.5$ for 10 kN of lift force. Even for only 50 m/s, F_L/F_D is not very large: 17.6. Clearly, isolated 1 m long magnets do not have very good characteristics.

This same data is replotted in Figs. 2.8 and 2.9. In 2.8, F_L/F_D versus the required lift force is shown for different speeds. In 2.9, the data for operating at 10 kN of lift is summarized: NI and F_D (drag force) are shown as a function of speed. As a reasonable rule of thumb, both NI and F_D are linear in velocity for fixed F_L and gap.

Let us now examine the behavior of longer magnets, shown in Figs. 2.10 and 2.11. In 2.10, the lift force/unit length as a function of NI is shown for $v = 0$ and $v = 134$ m/s. (At $v = 0$, the lift force/unit length is nearly the same for all magnets with $L \geq 1$m.). At the higher speed, the longer magnets clearly require less increase in current. For example, at $v = 134$ m/s the 3m long magnet requires $NI = 2.05 \times 10^4$ AT for $F_L/L = 10$ kN/m whereas the 1m long magnet requires $NI = 3.40 \times 10^4$ AT for the same lift/unit length. $F_L/F_D = 36.2$ for the 3m magnet compared to 8.5 for the 1m magnet at $v = 134$ m/s and $F_L/L = 10$ kN/m.

The main conclusion to be drawn is that the magnets on each side of the vehicle should be arranged so that they appear to be one long magnet stretching the entire length of the vehicle. In this case, the increase in current should be small and the drag force minimal. However, if the currents vary widely from magnet to magnet for control purposes, this will tend to break up the uniform flux pattern required for good magnet performance at high speeds. Clearly in the limit of isolated, 1m long magnets, the performance is not good. Magnets 3 meters long are much better but these might be too long for the control system to function properly.

2.1.6 Multi-Magnet Arrays

From our studies of track eddy-current patterns (Appendix B), it is clear that magnets must be widely separated to be considered isolated. Appreciable magnetic field and eddy current intensity extend ~ 0.5m beyond the ends of the magnet (i.e., for a full-scale magnet). In this section we investigate the effects of magnet interactions for two cases: (i) two magnets separated (in the direction of motion) by a small gap and (ii) an infinite periodic array of magnets.

From arguments similar to those given in Sec. 2.1.2, it is straightforward to show that in general (See Eq. (2.11).)

$$W_1 = -\frac{\mu_o}{2\pi^2}\frac{k_x}{k_y k} e^{-kh} \int_{-\infty}^{\infty} dx\, e^{-i k_x x} \int_0^{\infty} dy \cos k_y y \, J_x(x,y) \quad , \qquad (2.38)$$

Table 2.1. Comparison of $\varkappa$ from the model of Task II to the self-consistent calculation of $\varkappa_1$ for the upper layer of the track according to the present model. $\varkappa$ is adjusted to give the correct results at the point indicated by (*). [$\varkappa = (\text{Const})L^2/F_L V$, $p = 4$ cm, $h = 1.5$ cm, $c = 18$ cm, $\rho = 13.25$ $\mu\Omega$-cm]

v(m/s)	L(m)	F_L/L (kN/m)	$\varkappa$	$\varkappa_1$
50	1	3.00	283	180
		7.71	110	89.4
		10.7	79.3	68.3
100	1	2.59	163	124
		6.32	66.8	63.4
		10.95	38.6	39.3
134	1	2.395	132	111
		5.60	56.3*	56.3
		7.47	42.2	43.9
		9.48	33.2	35.6
134	2	2.83	222	151
		7.035	89.6	72.5
		9.64	65.4	55.8
134	3	3.039	310	185
		7.79	121	90.5
		10.8	87.2	69.3

where $J_x = \frac{\partial M_z}{\partial y}$ is the magnetization current density (assumed uniform in z for $z > h$ and zero otherwise). For a single magnet where J_x is uniform in x for $|x| < b$ and zero otherwise, (2.38) reduces to Eq. (2.24b). Making the assumptions in Eq. (2.27) gives Eq. (2.29) for W_1. Let us now call this W_1^S.

If now we add an additional identically shaped magnet with center at $x = x_o$ and magnetization $R\,M_z(y)$, we find for the double magnet configuration

$$W_1 = W_1^D \equiv W_1^S(1+R\,e^{-i k_x x_o}) \quad . \tag{2.39}$$

The reason that we include a scaling factor R in the magnetization is that if we require that the real ampere-turns (NI) of both magnets to be equal, somewhat different magnetizations are needed. This is a result of the different eddy current distributions and intensities under the two magnets.

If we let s be the separation between magnets, then $x_o = \pm(L+s)$ for an extra magnet leading (trailing) the reference magnet. $L = 2b$ is the magnet length. The self-consistent determination of the permeabilities is done as follows. We let the reference magnet be the leading magnet so $x_o = -(L+s)$. By making an initial guess for R and the $\varkappa_j$'s we find the new $\varkappa_j$'s and NI as before but with $W_1 = W_1^D$ (e.g., NI is given by Eq. (2.36) with $W_1 = W_1^D$). Then we repeat the process assuming the reference magnet is the trailing magnet ($x_o = +(L+s)$). By adjusting R and iterating, we can arrive at a ratio which gives the same NI for the two magnets. Typically, the leading magnet has about 20% smaller magnetization. The calculated permeabilities $\varkappa_j$ depend upon whether the leading magnet or the trailing magnet is the reference magnet. Typically, $\varkappa_1$ is about 10% smaller for the leading magnet as compared to the trailing magnet, not a large difference. The permeability for the second layer will vary more, but the results are less sensitive to it. We use the average values of $\varkappa_j$ for the calculation of the lift and drag forces. These forces are given by Eq. (2.25) with $W_1 = W_1^D$. The sign of $x_o = \pm(L+s)$ is irrelevant since only the absolute value of W_1 enters here.

Before discussing the results of calculations with this model, let us generalize it to an arbitrary number of magnets with position x_n and scale factor R_n. The result is

$$W_1 = W_1^S \sum_n R_n \, e^{-i k_x x_n} \tag{2.40}$$

with $R_o = 1$ and $x_o = 0$ ($n = 0$ is the reference magnet). Now for a periodic array, we take the $R_n = 1$ since all magnets are alike and $x_n = n(L+s) \equiv n L_x$, $n = 0, \pm1, \pm2, \cdots$. Clearly W_1 in Eq. (2.40) will be large only for $k_x L_x = m\, 2\pi$ where m is an integer. Detailed analysis shows that all the previous formulas in Sections 2.1.2 to 2.1.4 remain the same except that the integration $\int_0^\infty dk_x \cdots$ is replaced by the summation $\frac{2\pi}{L_x} \sum_{\substack{k_x = m2\pi/L_x \\ m \geq 0}} \epsilon_m \cdots$ for any quantity in which one factor of W_1 appears. $\epsilon_m = 1$ when $m = 1, 2, \cdots$; $\epsilon_o = 1/2$. (For $\int_{-\infty}^{\infty} dk_x \cdots$, m runs over all integer values and ϵ_m is omitted.) For the lift and drag forces per magnet, we find Eq. (2.25) holds with the integration replaced by the summation. No other changes are required; W_1 is still given by Eq. (2.36).

In Table 2.2, the results for several magnet separations s are shown. For s = 0, the results from the analysis of this section and the results from the previous section are compared in the first two lines. The small differences are due to the different methods of calculating the various quantities. In the first line, the magnetization is somewhat less in the leading half of the magnet than in the trailing half. This difference is required since we integrate $\int \underline{H} \cdot \underline{d\ell}$ along two separate paths to find NI. The first path contacts the magnet one

Table 2.2. The effect of magnet separation--two magnet array

($L=2b=1$m, $p=2a=4$cm, $c=18$cm, $h=1.5$cm, $\alpha a=5$, $a_1=0.5a$ $v=134$m/s, $\rho=13.25\mu\,\Omega$-cm, 1020 unannealed steel)†

s (cm)	NI (10^4AT)	F_L (kN)	F_L/F_D
0^*	1.97	14.1	23.0
0^{**}	1.89	14.1	24.1
0^{**}	2.35	19.3	21.9
1.5	1.97	14.0	22.8
14	2.00	13.5	17.2
14	2.48	18.5	15.7
∞	2.17	11.2	10.7

* From analysis of Sec. 2.1.6 with $s \to 0$.

** From analysis of Sec. 2.1.5 for single magnet 2m long.

† α and a are defined in Eq. (2.27d).

quarter of the way back from the leading edge and the second at three quarters the way back. Each path must give the same result. In the second line of Table (2.2), the magnetization is uniform in x with the integration of $\int \underline{H}\cdot d\underline{\ell}$ occurring half way back from the leading edge.

For a small separation, s=h=1.5cm, essentially no change in the results is noted when compared to the results for a 2m long magnet (s=0). For s=c-p=14cm, some changes are observed. We see that a slight reduction in lift has occurred and that the lift-to-drag ratio has been degraded somewhat.

The separation s=c-p is of interest because this is the minimum separation required if the windings were wound around the poles of the magnet in place of the yoke. There would be some advantage to this type of winding from the magnetic circuit viewpoint.

In Table 2.3, similar results are shown for an infinite periodic array of magnets. Quite good performance is found, even for a separation as large as 30 cm. The current required for a given lift per magnet is less dependent upon speed, and the lift-to-drag ratio is considerably better than for an isolated magnet. Clearly, for a large array, say 25 magnets, with spacing s $\simeq$ 14cm only the leading and trailing magnet are expected to contribute drag comparable to that of an isolated magnet. The others probably will behave much like magnets in an infinite periodic array.

Table 2.3. The effect of magnet separation--infinite periodic array (Parameters are the same as in Table 2.2) F_L is force on one magnet.

s (cm)	NI (10^4AT)	F_L (kN)	F_L/F_D
0	1.54	15.7	∞
10	.763	3.58	131
10	1.28	9.92	112
10	1.54	14.2	105
20	.790	3.49	62.0
20	1.34	9.56	50.9
20	1.63	13.7	47.4
30	.820	3.40	43.7
30	1.41	9.20	35.7
30	1.72	13.1	33.4
∞	2.17	11.2	10.7

2.2. Numerical Calculation of Fields and Forces on Two-Dimensional Magnets (TRIM and FORGEY Programs)

Magnetic flux in the ferromagnetic track is limited by magnetic saturation effects in both the track and the magnet. Such saturation effects cannot be treated analytically. In Section 2.1 saturation of the track resulting from a limited skin depth was taken into account in an approximate manner by using a multi-layer model of the track and determining the permeability of each layer self-consistently. To solve the full non-linear problem rigorously appears to involve a 3-dimensional numerical relaxation technique requiring substantially more programming and computational time than was available in the present investigation. It was, however, possible to study a more limited problem (the magnetic circuit at zero speed) by the relaxation technique; this allowed a detailed study of flux saturation in the magnet and a comparison of different rail geometries.

The very long and narrow nature of the electromagnets employed in the ferromagnetic suspension approach suggests that two dimensional calculations would be very useful for prediction of the fields and forces between the magnet and track (at zero speed). Two excellent programs called TRIM and FORGEY have been developed by Argonne National Laboratory[9] for the purposes of calculating the field, forces and energy for arbitrarily placed iron and currents in a two dimensional array. The inclusion of a B-H material table ennables the calculation to be done on any kind of magnetic material. The TRIM program generates a triangular mesh and performs a relaxation calculation of the magnetic field. FORGEY calculates the forces on the steel and on the windings as well as computing the energy stored in the iron and air.

TRIM is available in two versions--a 2500 point single precision version using approximately 420K of core on an IBM 360 and a 5000 point (maximum number of mesh points) double precision version using 720K of core. In both of these versions the output is tabular in form for the fields and forces over the mesh points of the region and also produces a magnetic tape to generate plots of the triangular mesh and the flux lines of the two dimensional problem. As shown in the following sections we have verified the accuracy of TRIM and FORGEY with experimental magnets and find that the programs agree with experimental results to a high degree, and thus may be used to predict the static performance of full-size magnets.

2.2.1. Experimental Magnets - Flat Track (MBB Geometry)

The TRIM and FORGEY programs were used to calculate the fields and forces on the cross section of the experimental magnet and track (see Section 2.3) with the B-H table of hard (unannealed) 1020 steel[10] (see Fig. 2.12). Figure 2.13 shows the flux plot of the experimental problem generated from TRIM, and Figure 2.14 depicts the triangular mesh on which the relaxation calculation was performed. Because of symmetry only one half of the problem needs to be solved, but the forces, energy and ampere turns listed needs to be doubled to obtain the results for the entire magnet.

In addition to the predicted field in the gap (from TRIM) agreeing closely with that experimentally measured, we also found that the experimental variation of the vertical field across both the face of the pole and the track agreed rather well with that predicted by TRIM. This is shown in Fig. 2.15. In this figure, the field "peaks" that exist at

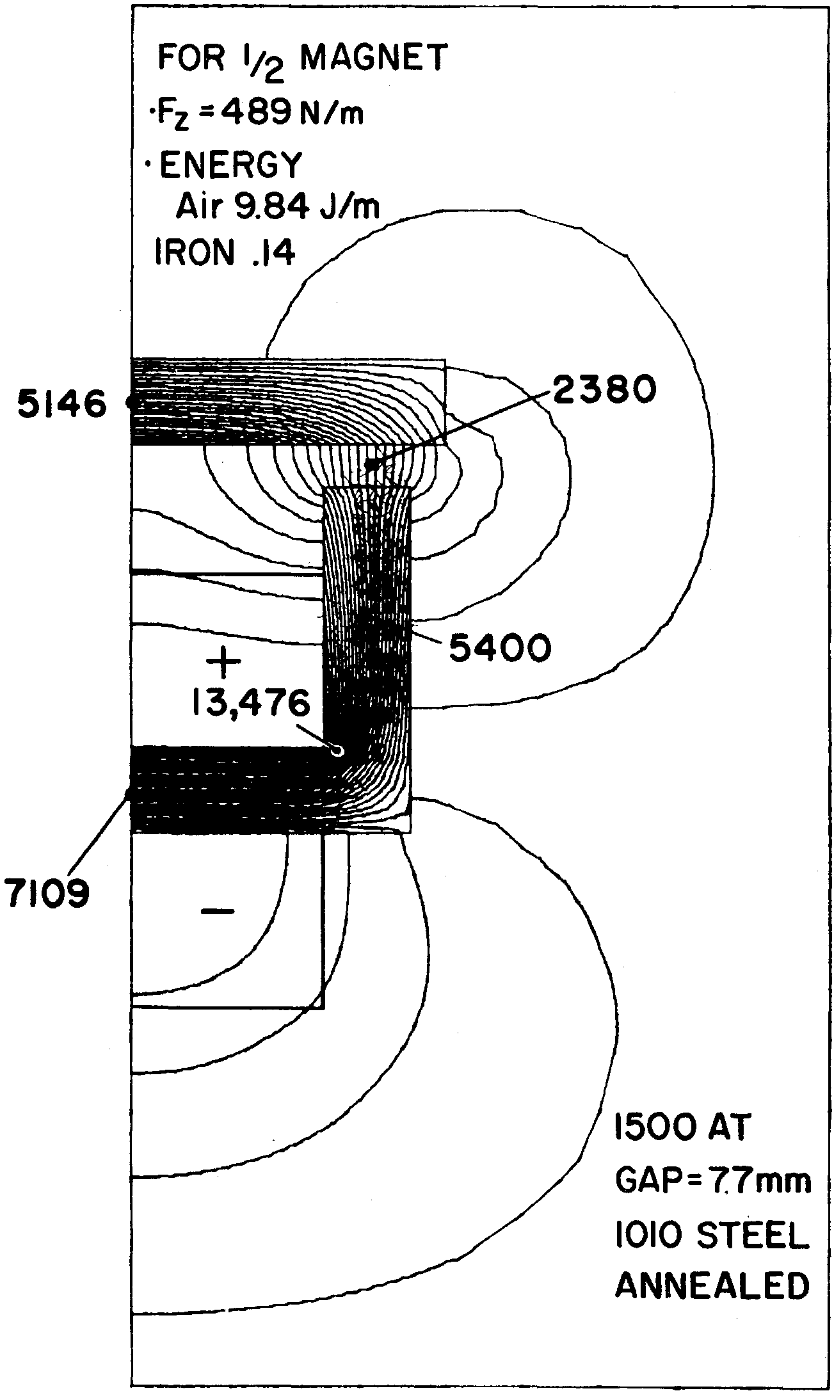

Fig. 2.13. Calculated flux plot for experimental magnet.

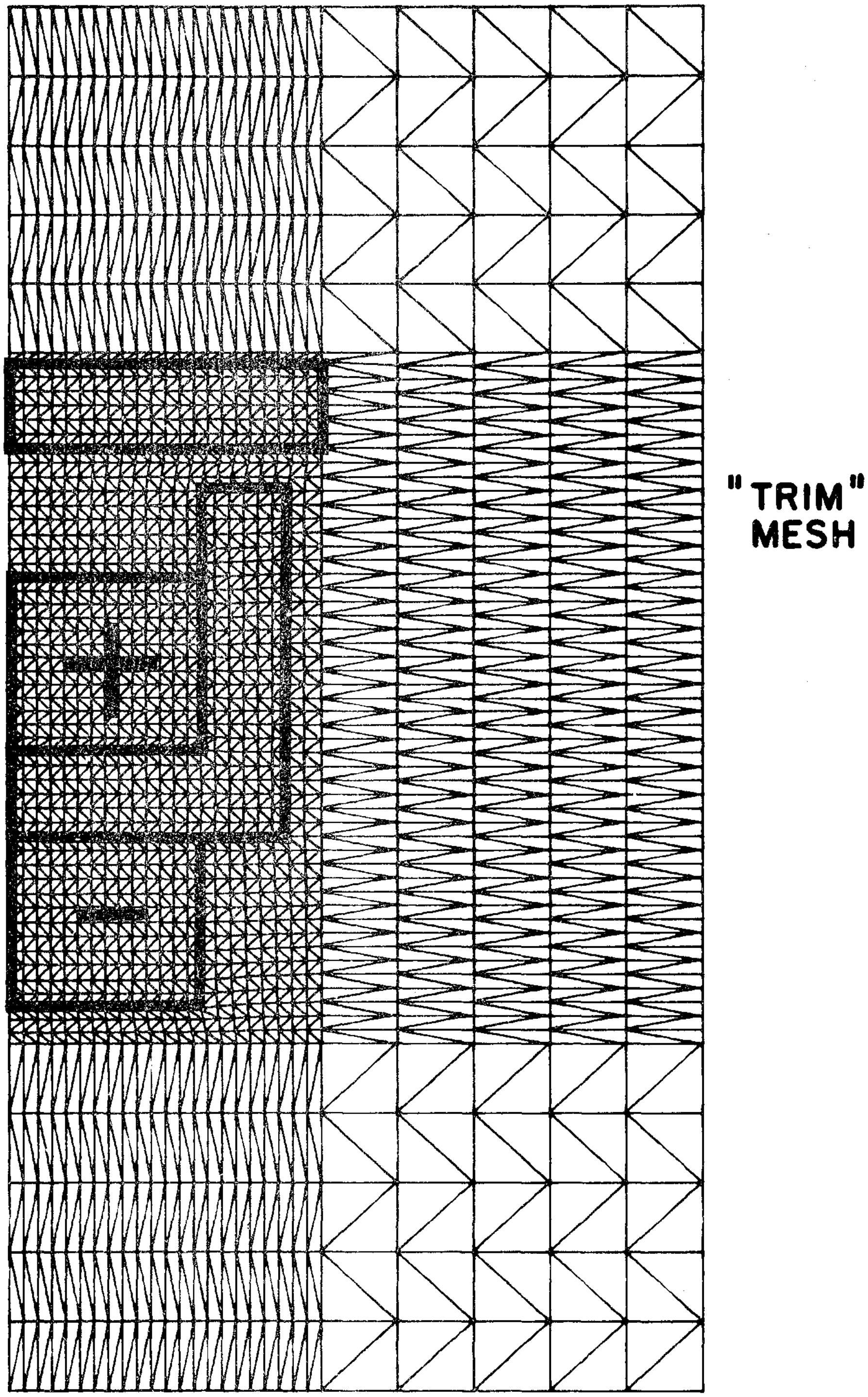

Fig. 2.14. Triangular mesh of TRIM program.

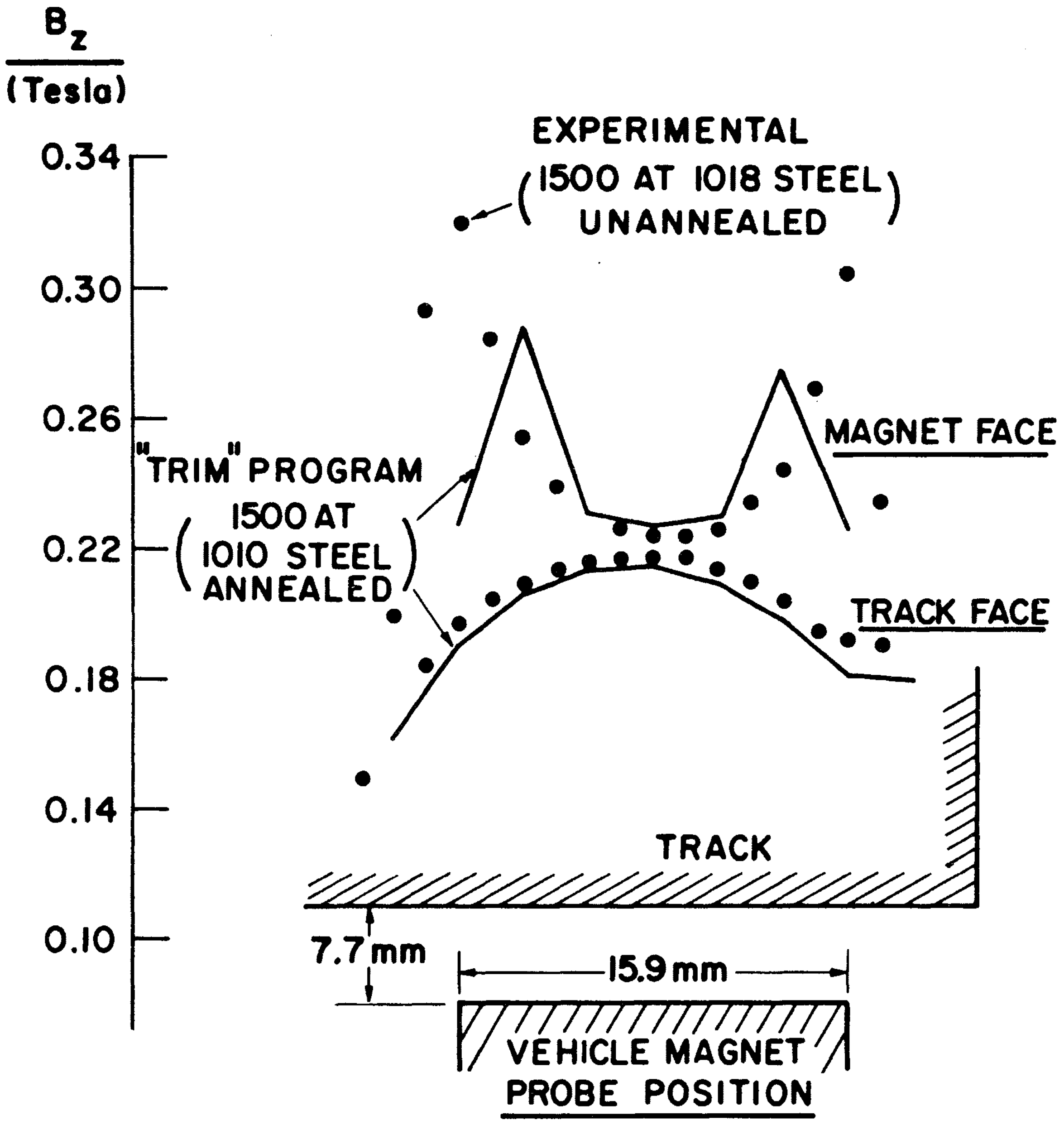

Fig. 2.15. Variation of vertical field in the gap.

the edges of magnet pole are more pronounced than that from TRIM, but it is felt that with a finer mesh the agreement with experimental values would be better.

The vertical forces for several values of current (up to saturation) are shown in Fig. 2.16 with the corresponding isoforce lines of the experimental magnet. Also shown in Figure 2.16 are five calculations done using the TRIM and FORGEY programs,--two at 7.9mm gap and three at 5.1mm gap. Note that because the outer pole piece of the magnet is longer than the inner pole piece (due to the curved design of the experimental magnet; see Figure 2.24), the field values predicted by TRIM and shown in Fig. 2.16 have been reduced by 6.7%, the amount of increased area of the outer pole face.

While the field and force values predicted by TRIM and FORGEY lie close to those actually measured in regions where saturation of the iron has not occurred, the experimental curve at 5.1 mm gap in Figure 2.16 saturates at lower values of current than that predicted by the TRIM and FORGEY programs. The most probable explanation for this is that since the experimental magnet pole pieces are longer than the magnet core there are added constrictions over the two dimensional modes which will force the flux lines together in local areas, increasing the field in these areas and thus causing saturation to occur earlier than if the magnet core and pole face were the same length.

Figure 2.17 shows the flux plot for 4500AT at a gap of 5.1mm. The steel is highly saturated as the field values indicate. This plot should be contrasted to that of 1500AT shown in Figure 2.13. Note the difference in the flux concentrations at the corners of the magnet for both of these figures.

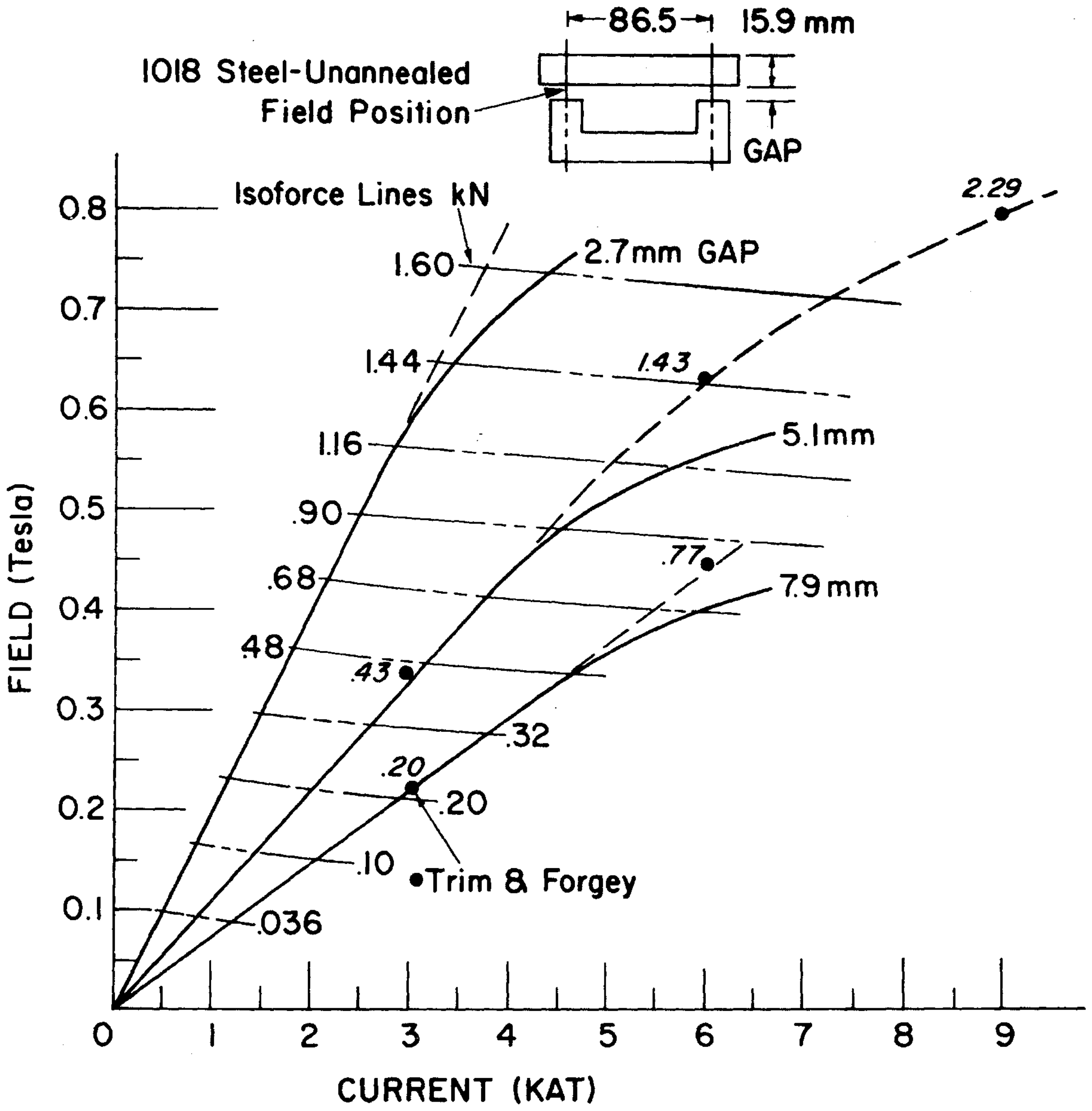

Fig. 2.16. Magnetic field and lift force as a function of current for the experimental magnet for various gaps.

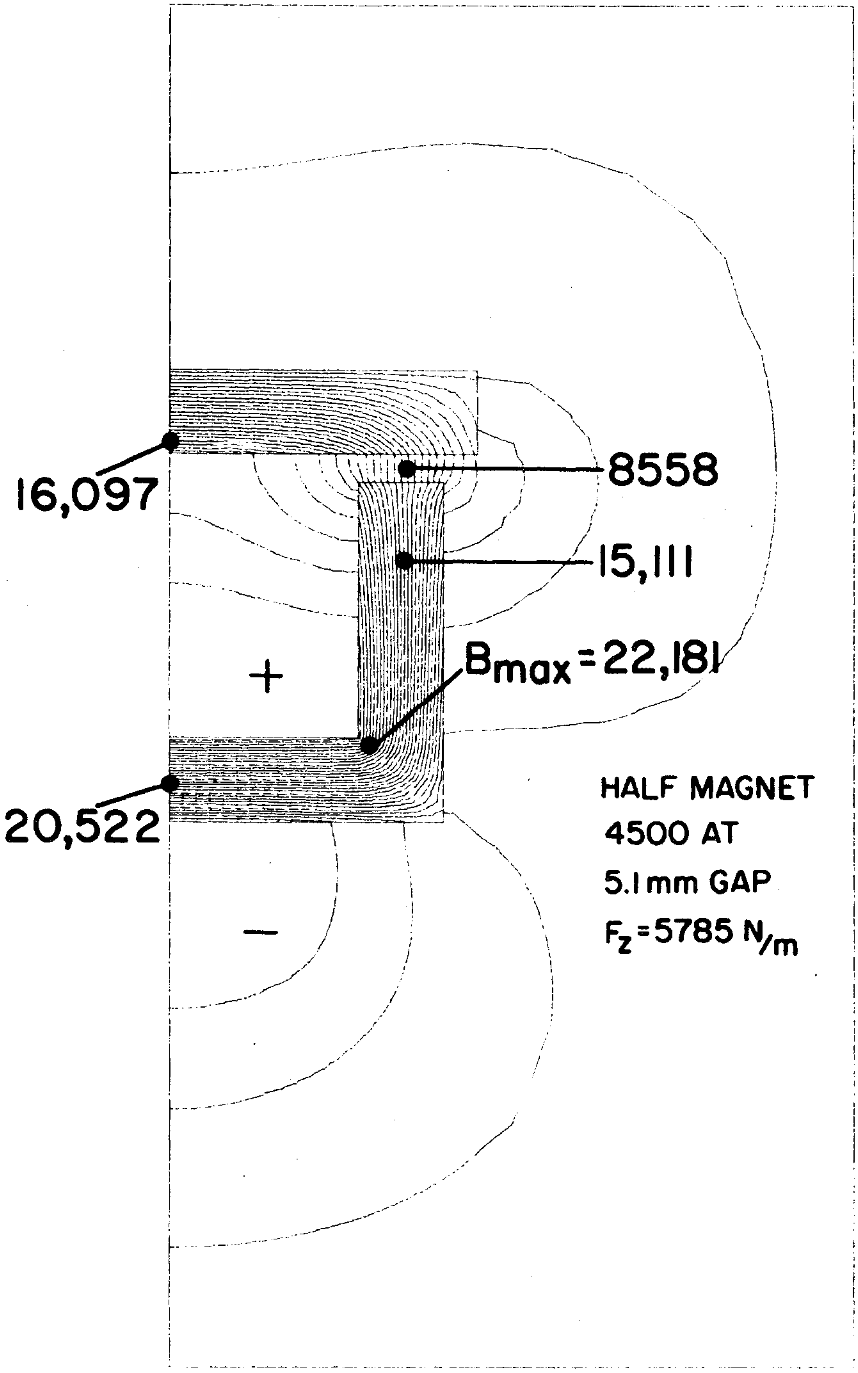

Fig. 2.17. Calculated flux plot (4500 AT; 5.1 mm gap).

2.2.2. Experimental Magnets - U Track (K-M Geometry)

Since the programs TRIM and FORGEY accurately predict the fields and forces on arbitrarily placed iron and currents, we were able to compare the two ferromagnetic suspension systems, i.e., 1) the combined lift and guidance magnets (U track-KM) and 2) the separate lift and guidance magnets (flat track-MBB) for the same magnet. Although the 2500 point version of TRIM and FORGEY was used to give the previous results for the flat track, the 5000 point version is necessary for the U shaped track since displacement of the magnet from the centerline of the track will destroy the symmetry of the problem. Such a displacement is a necessary requirement for guidance.

Using a constant 3000AT for the magnet and a constant gap of 7.9mm the results from TRIM and FORGEY are summarized for three magnet displacements in Fig. 2.18. The flux plots for these three displacements are shown in Figures 2.19, 2.20 and 2.21. These results lead us to the following conclusions:

- Lift force for the U shaped track (K-M design) always lies below that for the flat track (MBB design). This holds true even when the current density is increased in the K-M design to provide the same maximum field in both magnets. (This is not a valid assumption for comparison since one coil shouldn't be allowed to heat up more than the other.)
- Because of its inherent design (desire for both lift and guidance forces from the same magnet) leakage flux is a more serious problem in the K-M design than in the MBB design.

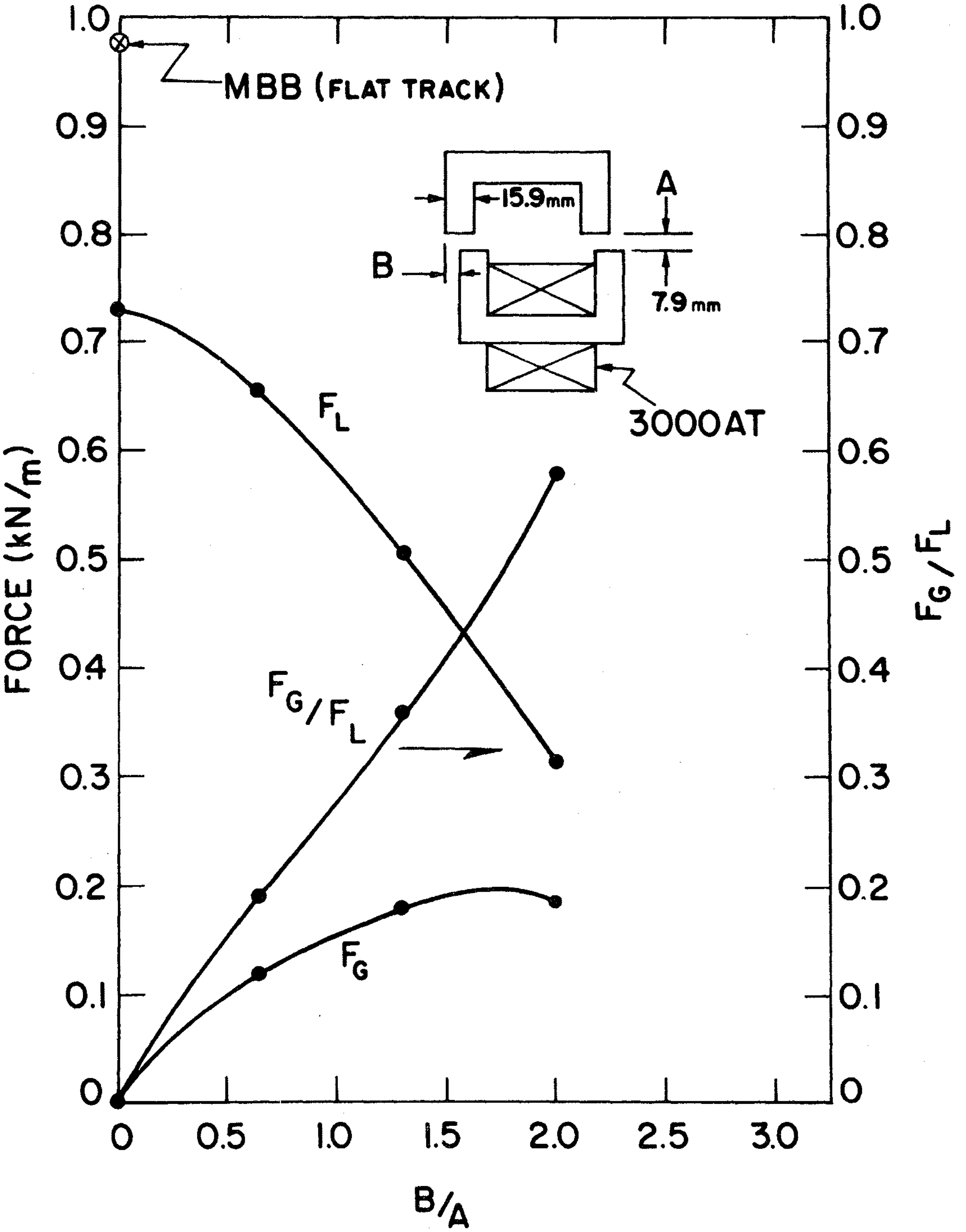

Fig. 2.18. Lift and guidance forces for the K-M geometry.

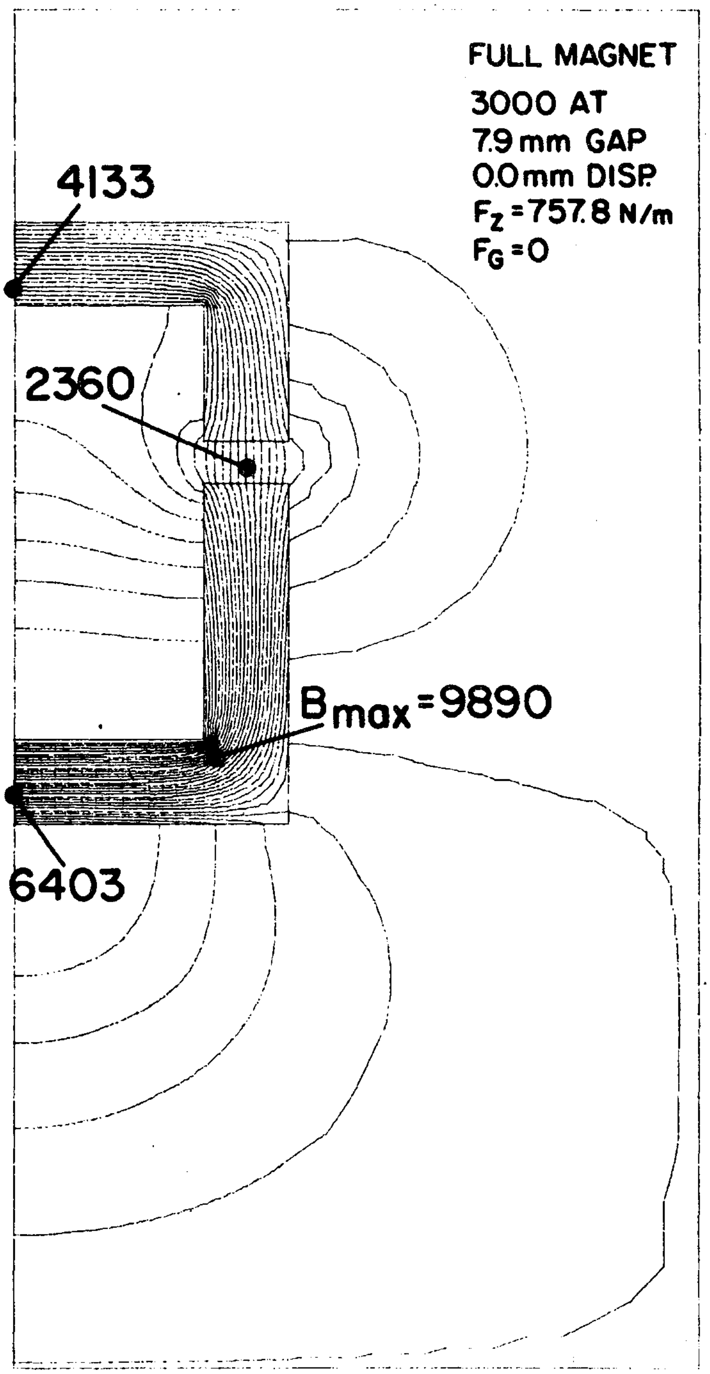

Fig. 2.19. Calculated flux plot for K-M geometry.

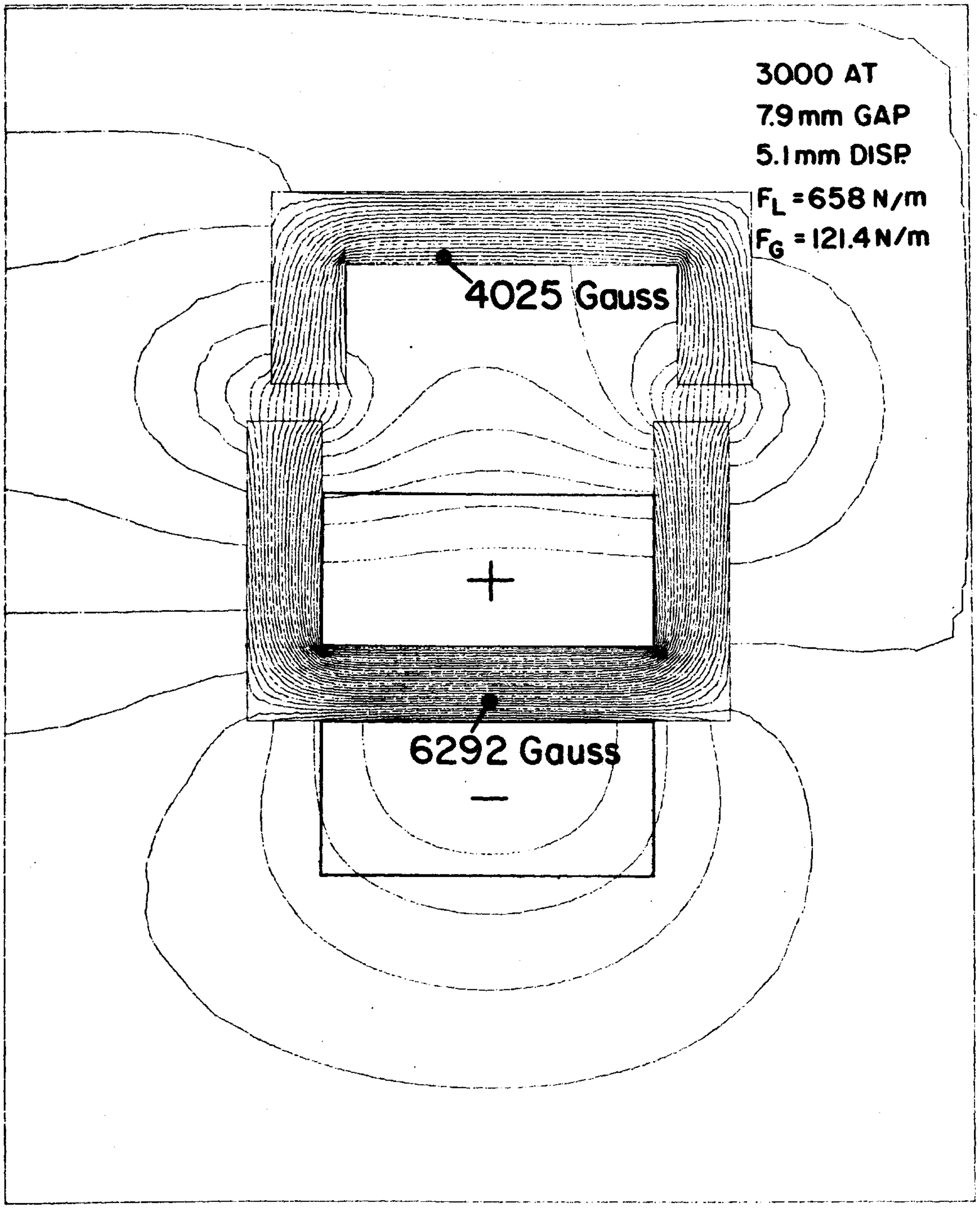

Fig. 2.20. Same as Fig. 2.19; 5.1 mm displacement.

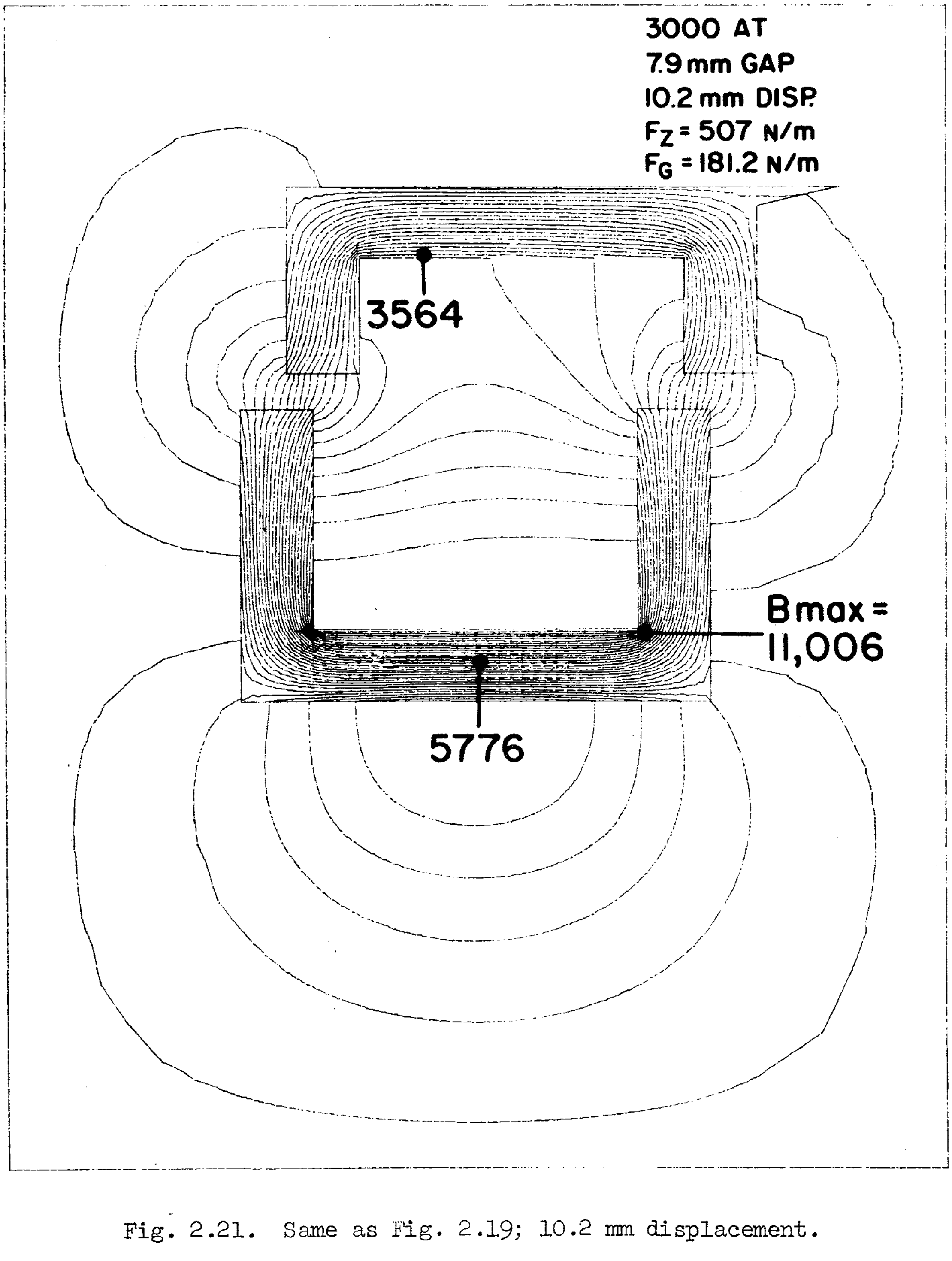

Fig. 2.21. Same as Fig. 2.19; 10.2 mm displacement.

2.3. Experimental Studies

The raison d'etre for the experimental part of the electromagnetic suspension program is to serve as a base to which theoretical models can be compared. This is necessary since the laboratory magnets are smaller than the full size magnets that would be used on a passenger-carrying vehicle. Once a good theoretical model is found to agree with the experimental results, then the performance of full-size magnets can be predicted. The reason for this approach is primarily economic in nature; i.e., it is cheaper to perform experiments in the laboratory on a small scale, and use an accurate theoretical model to predict the full scale results. Also it may be the quickest approach to get the most significant results.

We were fortunate to have had a great deal of success with this approach in the previous programs (Tasks I and II) using small superconducting magnets over a rotating aluminum wheel. Because of this past success we felt that the experiments in this present program had to show the magnetic lift and drag forces as a function of velocity and magnet current, and, as parameters, the width and length of the magnet and the conductivity and permeability of the track. A good theoretical model would then be able to consider these parameters and be able to predict the results.

In designing the experimental program we used our experience from an early experiment in which an attempt was made to measure the lift and drag forces of an electromagnet above a small rotating steel wheel (reference 1, Section 3.2.1). The results from this experiment were inconclusive because the gap field was found to increase along the length of the magnet at higher speeds, causing a mixing of the lift and drag forces seen by the force transducers. For this reason we felt that a flat track was imperative for "good" measurements. Since we had the 1.5 m diameter aluminum wheel, it was suggested that the flat track be mounted on the side of the wheel as a continuous circular ring and that the magnets have curved pole pieces to fit the track. See Figures 2.22, 2.23 and 2.24. Four magnets were required for this experimental program and the parameters of these magnets are listed in Table 2.4.

Table 2.4. Parameters of Experimental Magnets

Magnet	Width (mm)	Avg. Pole Length (mm)	Number of Turns	Weight of Iron (kg)	Weight of Copper (kg)
1	86.5	195	322	5.0	5.5
2	"	"	265	4.4	4.5
3	"	"	"	"	"
4	71	"	214	4.7	3.6

All magnets have pole thicknesses of 15.9 mm and are made from 1018 hot rolled steel.

Since the forces between the magnet and track become quite large ($> 10^3$N) for realistic fields on these magnets, it was necessary to build a rugged frame utilizing linear bearings to allow motion in the three orthogonal directions for measuring lift, drag, and, for future experiments, guidance. This frame and support system can be seen in Figures 2.22 and 2.23. A feedback control system, developed in Task II of the program; was utilized in one part of the experimental program to verify that the control system would work with $v \neq 0$. That is, with increasing

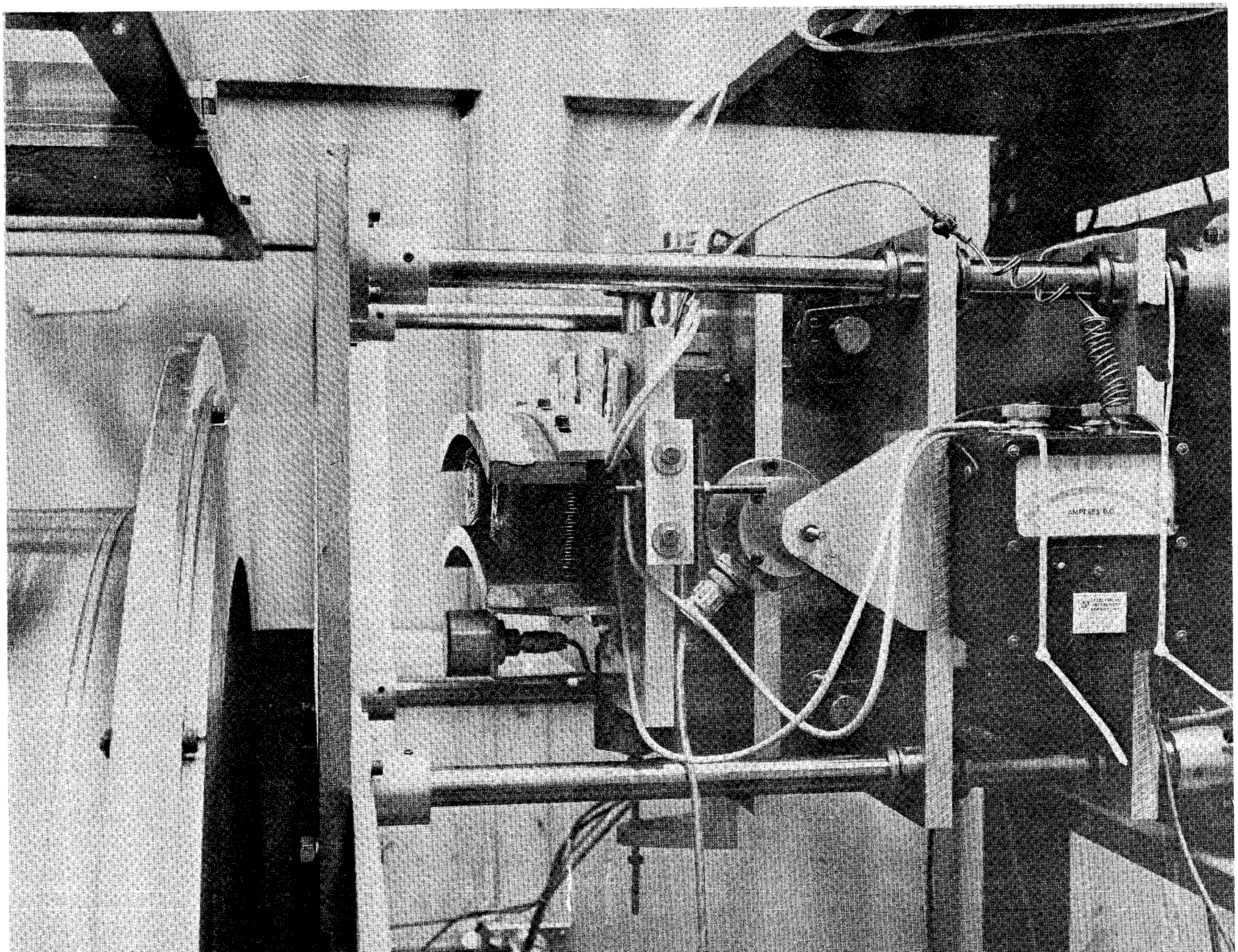

Fig. 2.22. Magnet frame for use with rotating wheel facility.
See also Figure 2.23.

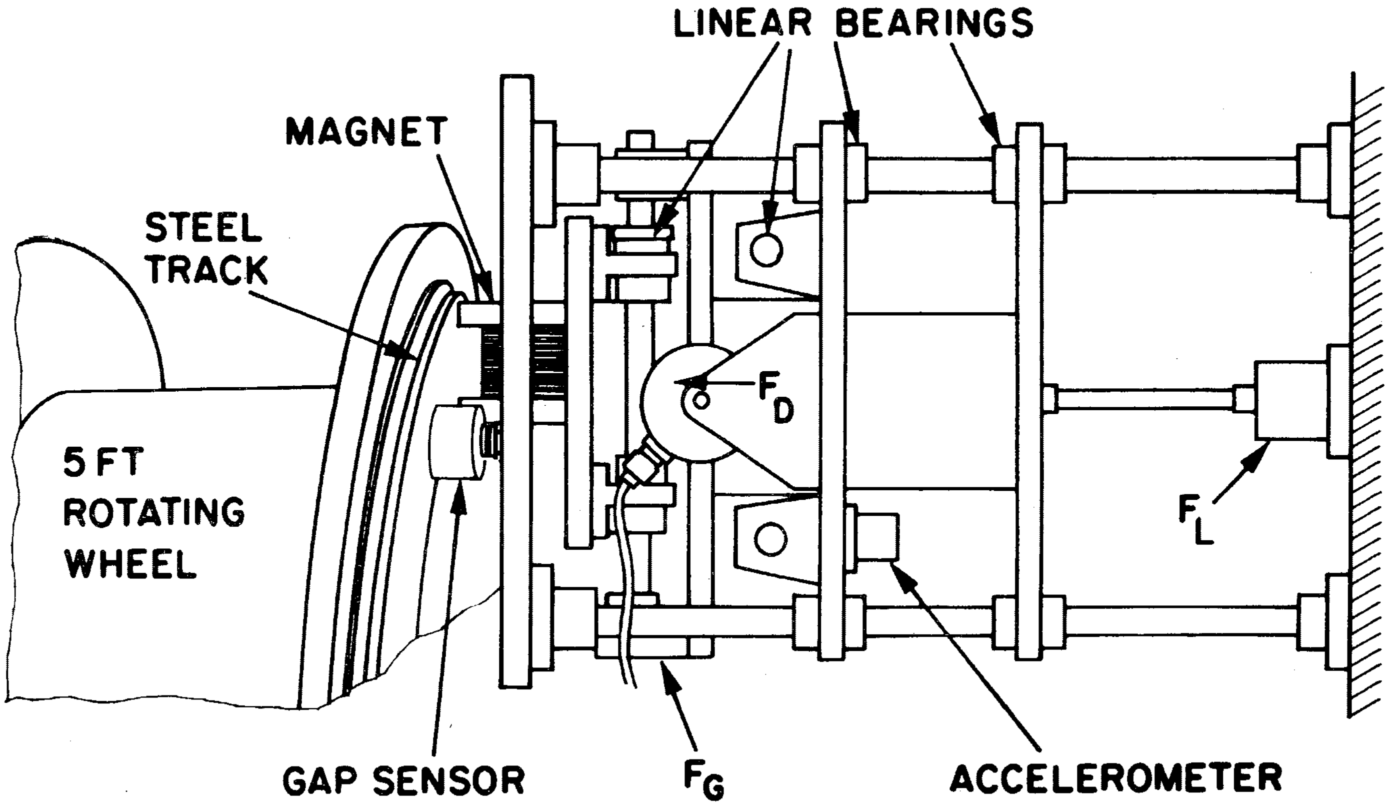

Fig. 2.23. Schematic of magnet frame shown in preceding figure.

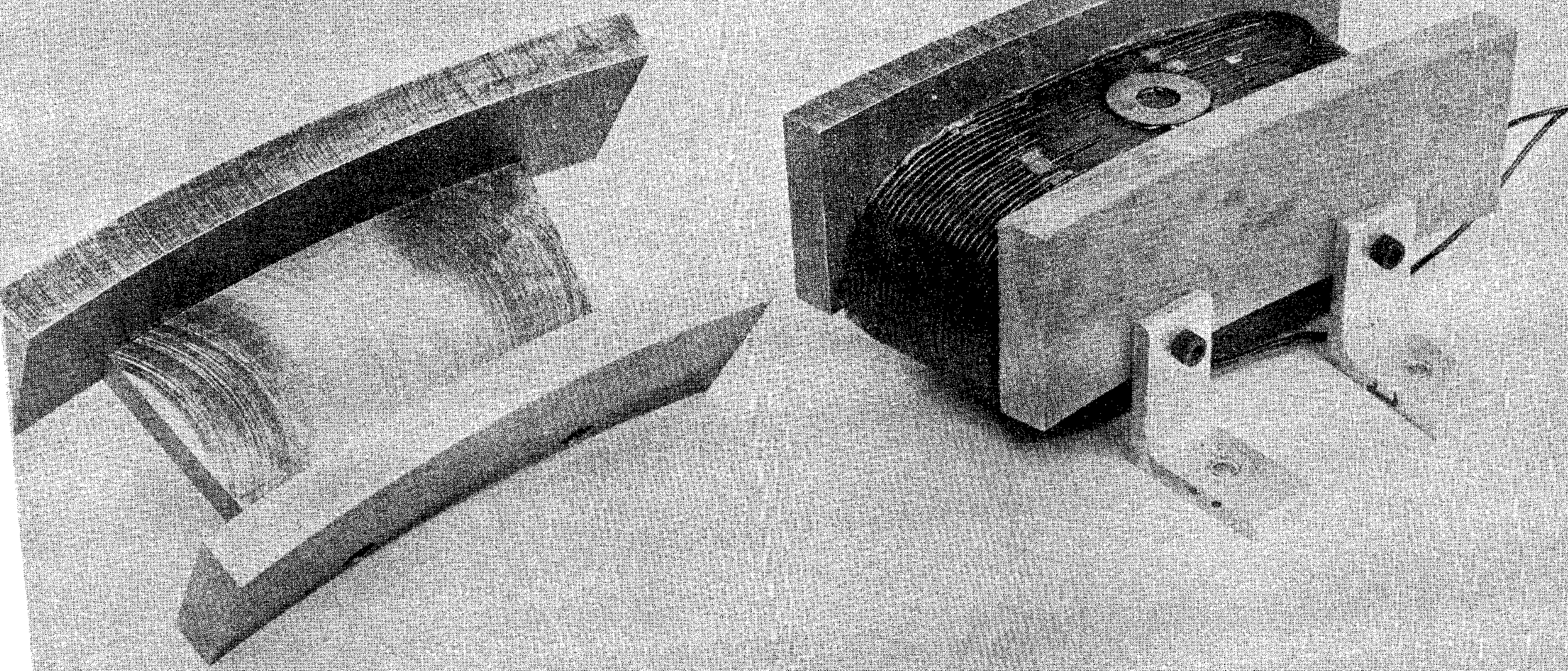

Fig. 2.24. Electromagnet and yoke. Note curved pole pieces.

velocity, current would increase to maintain a constant gap and force. In this experiment in which current and drag force were measured as a function of velocity, a spring served as a link between the magnet and the lift transducer providing an almost constant load over small displacements of the magnet. The gap sensor can be seen in Figs. 2.22 and 2.23.

The other experiments can be divided into two types: zero velocity involving a single magnet and finite velocity in which magnet width and length were parameters.

2.3.1 Zero Velocity Measurements

The measurements made at zero velocity were to record (i) the lift force and magnetic field as a function of magnet current for a constant gap and, (ii) the measurements of magnetic field across the pole face. These results are shown in Figs. 2.15 and 2.16, compared with predictions of the two-dimensional magnet TRIM and FORGEY programs. The first of the two figures (Fig. 2.15) showing the variation of the z component of the field across the pole face of the magnet pointed the way to an improvement in the theoretical model (see Section 2.1.2) giving closer agreement to experimental results. The other figure, 2.16, shows the field at the pole face as a function of the magnet current. In this figure the onset of saturation can be easily seen. Saturation is occurring in the magnet core, not the rail, as is evident from the flux plot (Fig. 2.17). The region up to saturation defines the linear domain of the magnet over which the velocity-dependent model should be valid. (The velocity-dependent model developed in Section 2.1 takes into account saturation of the track iron but not saturation of the magnet iron.)

2.3.2 Velocity Dependent Measurements: Single Magnets

The most direct velocity-dependent measurements would be those showing the decrease in the lift force with increasing velocity for constant magnet current. While this type of measurement does not correspond to actual application (where average lift force remains constant for increasing velocity as magnet current is increased to provide the constant lift force) it could be used to check the theoretical calculations. However, because of the large forces that exist between the magnet and the track, small deformations of the magnet supporting structure occur, such that if the force were not kept constant the magnet-track gap would change. Since this problem is easily eliminated by making measurements at constant lift force, this was the procedure used.

While the field, B_z, in the gap is uniform along the length of the magnet at zero speed, there is a decrease in this field at $v \neq 0$ since a back mmf is created from the induced eddy currents. This change in field is shown in Fig. 2.25.

Figs. 2.26 and 2.27 show the velocity dependence of the drag force and magnet current for a magnet-track gap of 7.9 mm and constant lift force. For these measurements active feedback control was used. Note also that the narrower magnet shows a higher F_L/F_D than the wider magnet consistent with the similar results obtained for the superconducting magnetic suspension (see reference 1). This result implies that the ferromagnets should be made as narrow as possible in order to have a high F_L/F_D. Practically, what prevents the use of very narrow U-shaped magnets is the need to have a sufficient number of ampere turns ($\sim 2 \times 10^4$ AT) at a current density ≤ 2 A/mm^2 (unless forced cooling is used) surrounding

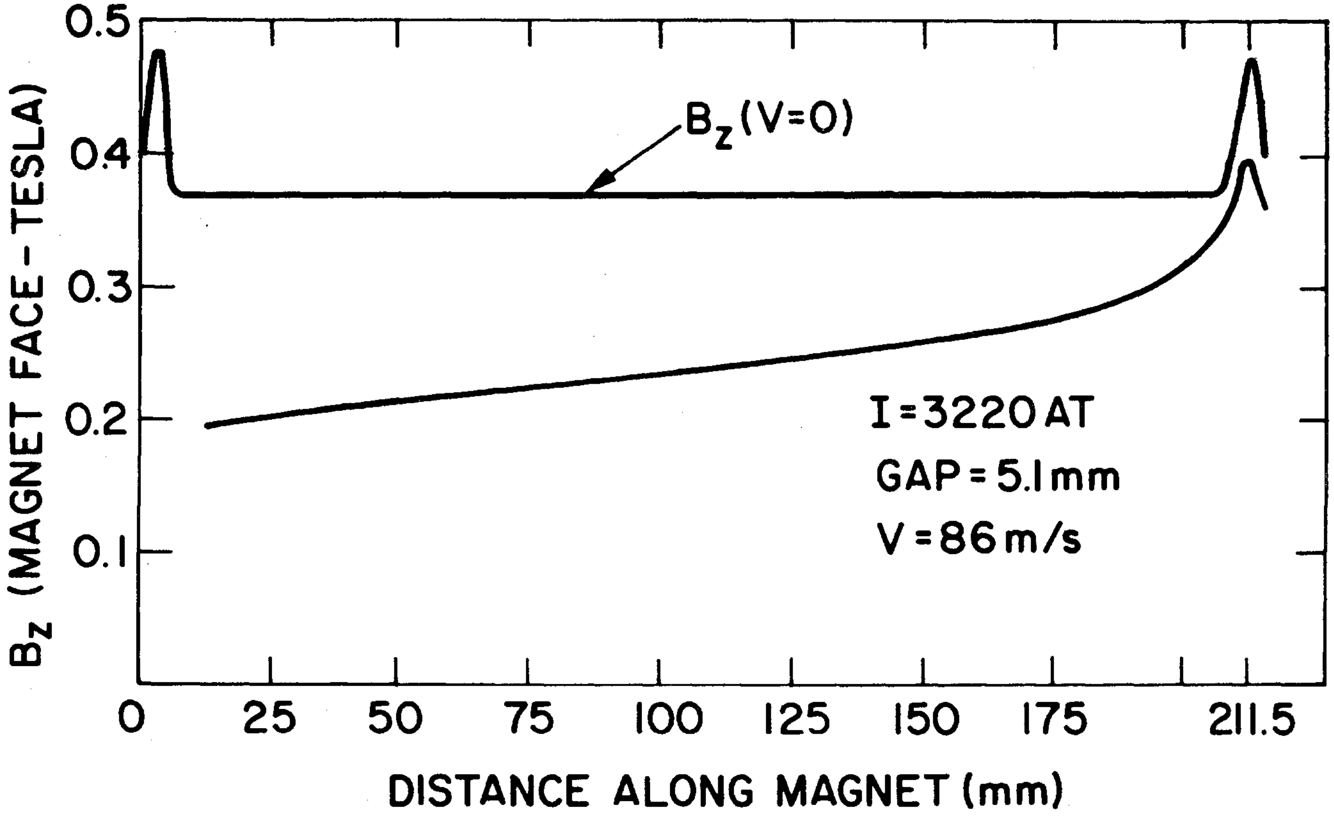

Fig. 2.25. Magnetic field in the gap for two different vehicle speeds.

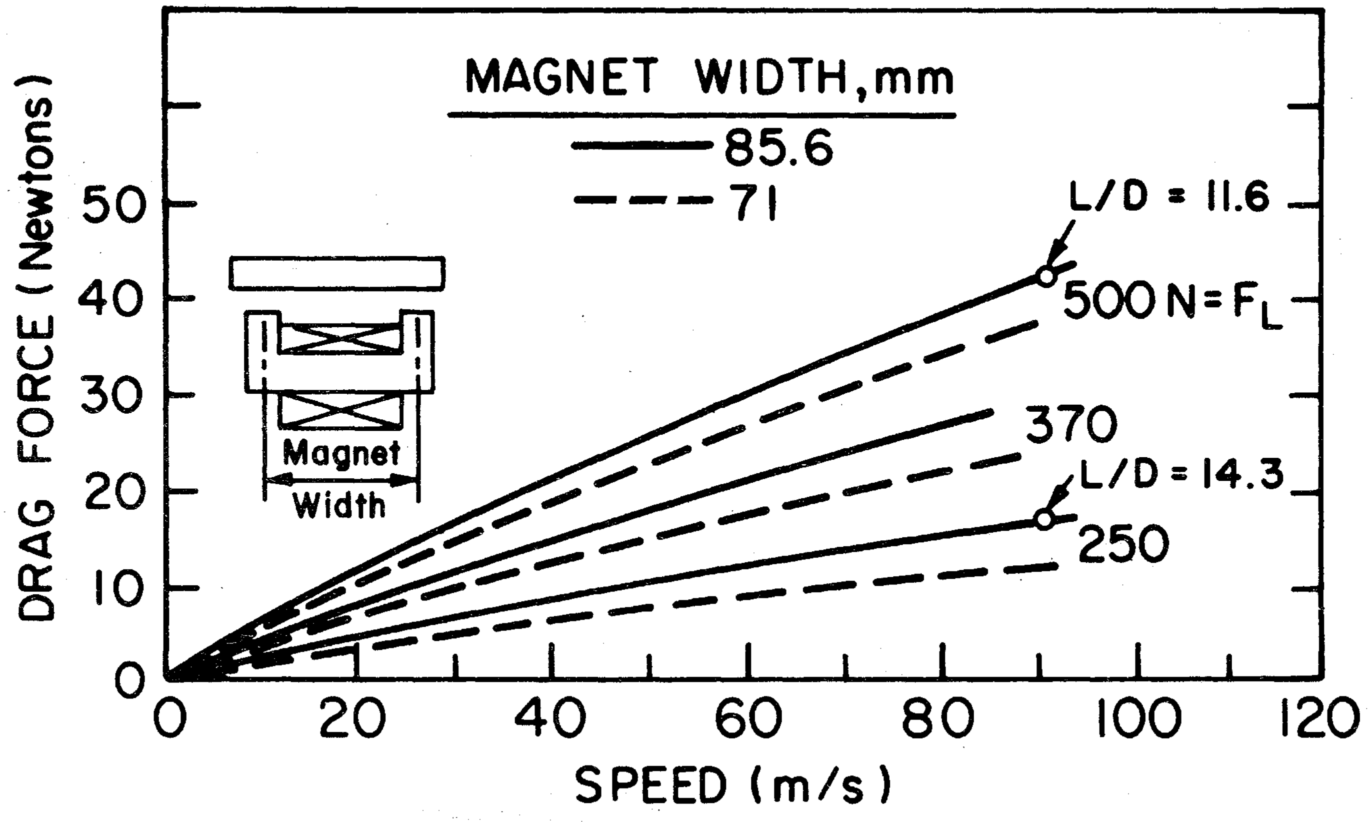

Fig. 2.26. Velocity dependence of drag force for fixed lift.

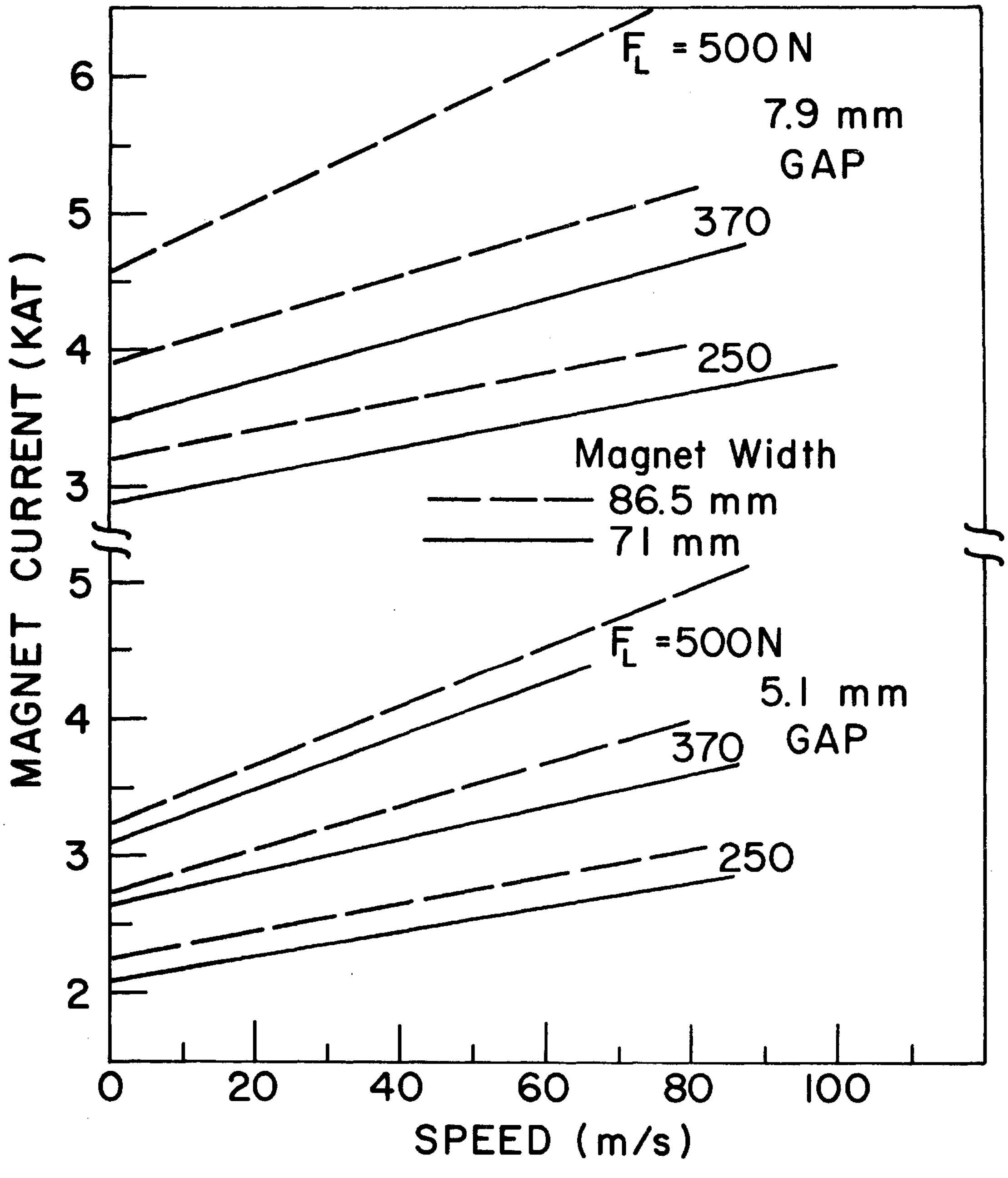

Fig. 2.27. Velocity dependence of magnet current for fixed lift.

the iron. To design a narrow magnet, one might design a magnet in the shape of a narrow, deep "U" but this will tend to increase the leakage flux, particularly at large magnet track gaps. The use of the computer programs TRIM and FORGEY should enable one to optimize this part of the magnet design.

2.3.3. Double Magnets

To investigate the effect of magnet length on F_L/F_D, two identical magnets were made such that they could be put in the form of a "train" - with or without any spacing between the magnets. In this manner not only could the effect of magnet-length doubling be examined but also the important practical effect of how F_L/F_D depends on the magnet separation.

That the length dependence of the magnet could be obtained from adding an additional magnet implies that the magnetic field be uniform along the length of the pole piece. This was not at all obvious from the appearance of the magnet, as shown in Fig. 2.24, where it is seen that the pole pieces extend beyond the magnet core. That the field was found experimentally to remain uniform along the length of the magnet as shown in Fig. 2.25 enabled these measurements to be made.

The experimental results are listed in Table 2.5 for three experiments of (a) single magnets and (b) two magnets--with zero separation and an average separation of 2.75 cm. A cursory examination of these results indicate that (i) with a doubling of magnet length F_L/F_D doubles (for equal lift force per unit length), (ii) separating the magnets by a small amount does not appreciably affect F_L/F_D.

Table 2.5 Experimental Results for Double Magnets

SINGLE MAGNET (#1) (322 Turns) Gap = 5.1 mm

F_L	F_D	I(v=0)	I(v=80m/s)	F_L/F_D
778N	73 N	13.2 A	23.7 A	10.7
584	51.5	11.2	17.3	11.3
389	31.4	9.1	13.5	12.4
195	13.1	6.6	8.7	14.9

TWO MAGNETS (#2 and 3) (265 Turns ea.) Gap = 5.1 mm

SEPARATION	F_L	F_D	I(v=0)	I(v=80m/s)	F_L/F_D
0	1170 N	54 N	14.6 A	21.5 A	21.7
"	778	32.1	10.4	14.3	24.2
"	584	22.5	8.85	11.85	27.1
"	389	13.5	7.25	9.25	28.8
2.75 cm	1170 N	54.9 N	14.75 A	24.25 A	21.3
"	778	32.7	10.4	14.4	23.8
"	584	22.6	9.95	11.8	25.8
"	389	13.8	7.25	9.37	28.0

This is an important conclusion for it ennables the magnet windings to be placed around the pole pieces resulting in a more efficient magnet design--i.e., greater lift to weight ratio and less leakage. Another consequence of these experiments are guidelines for practical current densities. Without forced cooling, r.m.s. values of 2.0A/mm^2 appear to be the upper limit because of magnet heating. With forced cooling these values could be increased to greater than 3 A/mm^2.

2.3.4. Comparison of Experimental and Theoretical Results

In the previous sections we discussed the experimental results and the theoretical model separately as though they were independent. In reality, the initial experiments helped guide the "construction" of the theoretical model and in turn the model was used to indicate what experimental measurements should be important.

To compare the experimental and theoretical results we chose the velocity dependence of the drag force and the magnet current (for constant lift) for two different width magnets, and the high speed F_L/F_D dependence on lift force for two different length magnets. These results are shown in Figures 2.28 and 2.29 respectively.

In Figure 2.28, the magnet current is seen to be overestimated by the theory at all speeds while the drag force prediction is less than that of the experimental model at higher speeds. This undoubtedly, is one of the reasons for the ~ 15% higher theoretical estimate of F_L/F_D shown in Figure 2.29. Also, note that the results in Figure 2.28 are at 5.1 mm gap while those in Figure 2.26 are at 7.9 mm.

Experimentally F_L/F_D is found to approximately double when the magnet length is doubled. This important feature is predicted correctly by the model, which gives us confidence that our estimates of the behavior of full-scale magnets is reasonable. Probably, we overestimate the magnet current (for fixed lift) at all speeds and underestimate the drag force at high speeds by amounts comparable to those shown in Figs. 2.28 and 2.29, i.e., ~ 15%.

Comparison of theory and experiment at the 7.9 mm gap gives essentially the same kind of agreement.

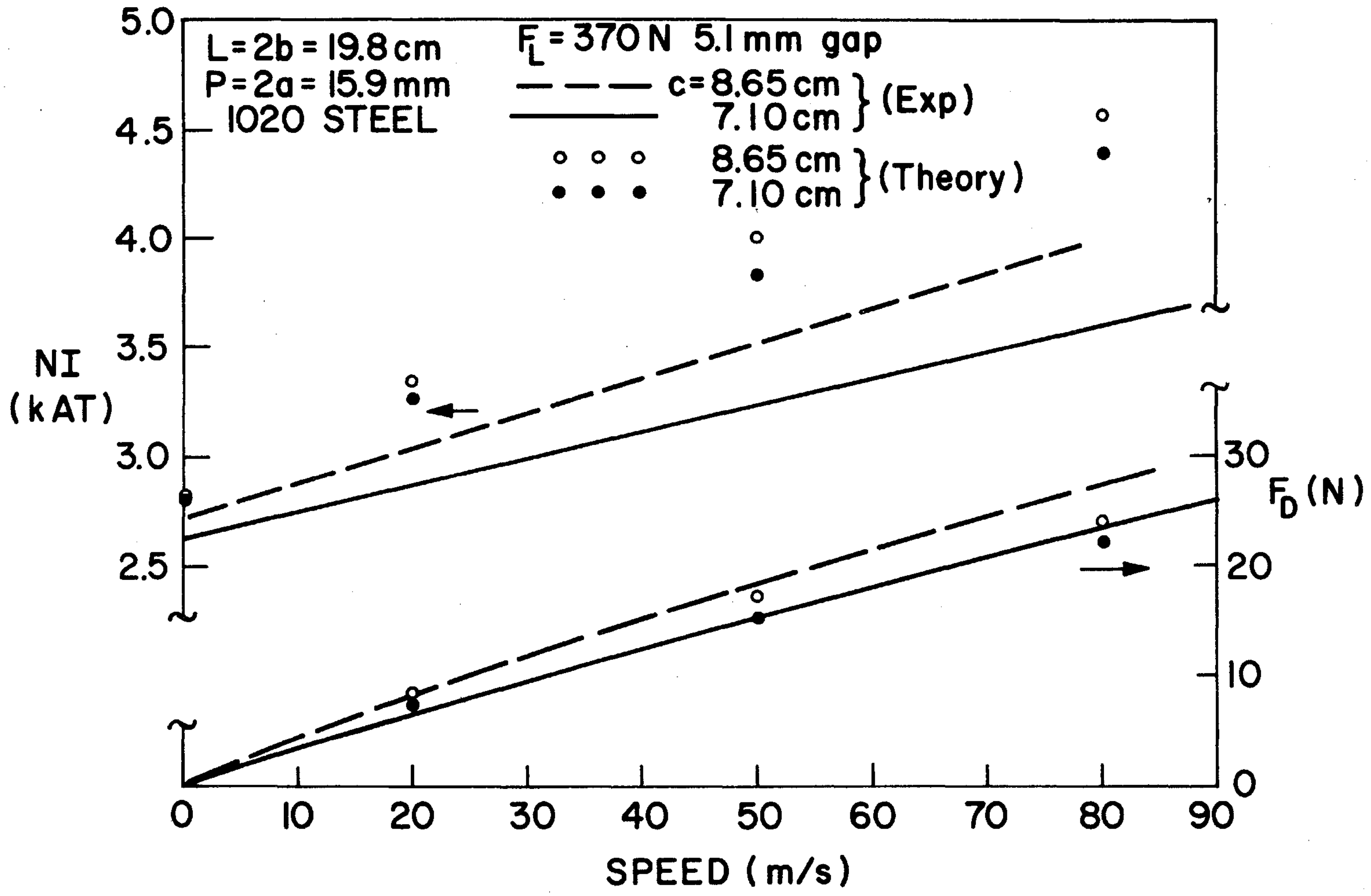

Fig. 2.28. Velocity dependence of drag and of magnet current. Comparison of theory and experiment.

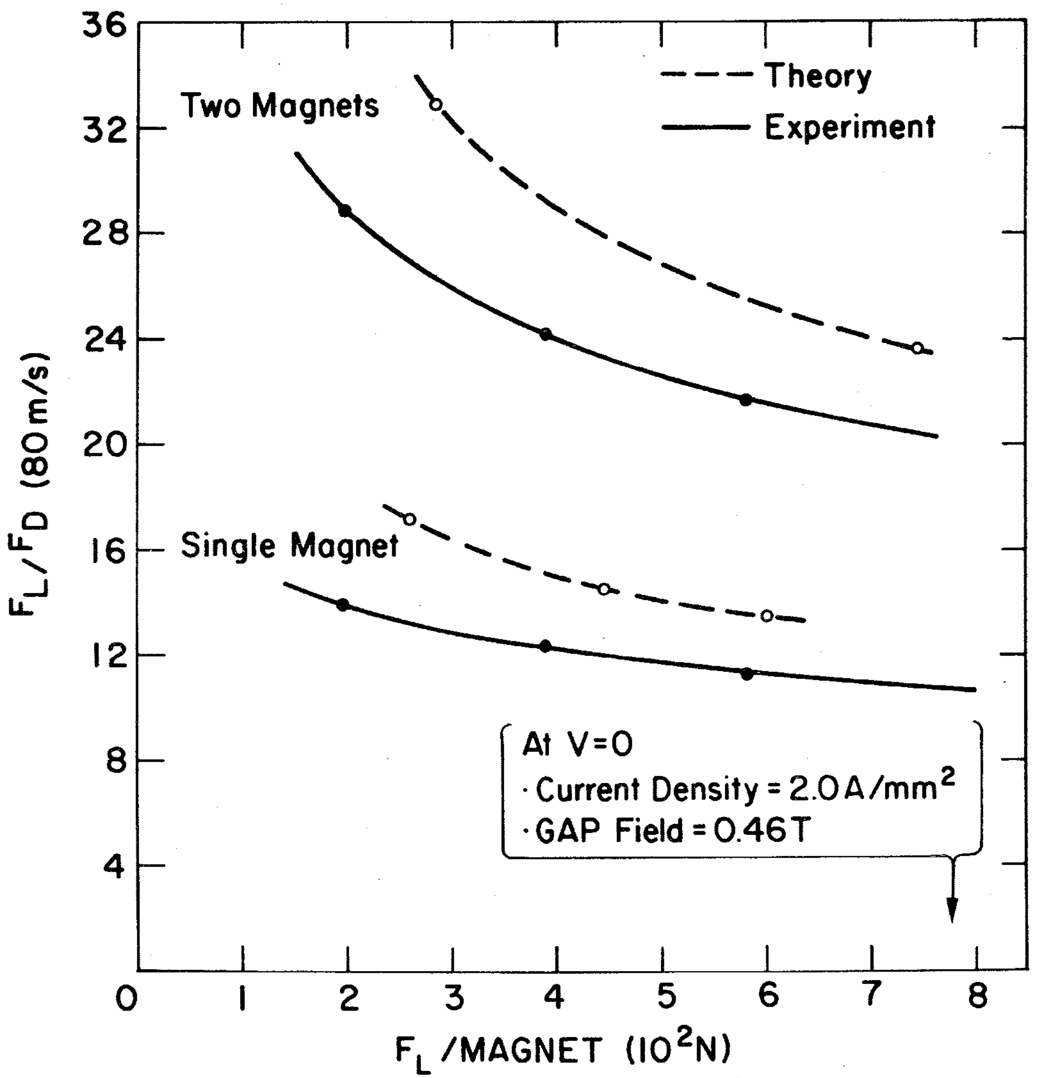

Fig. 2.29. Lift-to-drag ratio versus lift force for two different magnet lengths.

The calculations for full-scale magnets, presented in Sections 2.15 and 2.16, were concerned with magnet performance as a function of vehicle speed, force level, and magnet length. Changes in magnet geometry, except for length, were not considered. The magnet width (c = 18 cm)* and the pole width (p = 4 cm) are of the same order as designs proposed by MBB and Krauss-Maffei; these dimensions are determined primary by practical considerations. The pole width is a compromise between adequate flux-handling capacity and low magnet weight, whereas the c dimension was chosen to accommodate a practical coil in a low-reluctance, low-weight yoke. The experimental results on model magnets (Figs. 2.26 and 2.28) show, however, that narrower magnets can give a larger F_L/F_D, and this observation is borne out by calculation.

It was felt desirable to repeat some of the full-scale magnet calculations to accommodate changes in magnet geometry. The results are shown in Fig. 2.11 as the points ×, △, and O; all three points correspond to a magnet length L = 1 m. The point O is for c = 9 cm, p = 4 cm. F_L/F_D is increased about 60%, a substantial amount; concurrently, the magnet current is reduced about 26%. Presumably, the flux is able to penetrate deeper into the track with the narrower pole separation, thus increasing the skin depth. Since the c dimension is cut in half, either the coil must be wound with thinner wire (thereby increasing its resistance) or the depth of the yoke must be increased (thereby increasing its reluctance and weight); in either case the efficiency of the system (at low speed) is impaired, but the potential gain in F_L/F_D may justify this.

The point × is for c = 18 cm, p = 2 cm. F_L/F_D is increased by about 27%; concurrently the magnet current is increased about 16%. But the calculation ignores core reluctance, and the narrow pole face (p = 2 cm) is bound to

---

* See Fig. 2.1 for definition of c and p

saturate, particularly at the higher current levels. Thus it is not clear that this option will increase F_L/F_D in the practical case. The point Δ corresponds to $c = 9$ cm, $p = 2$ cm; this shows the best improvement in F_L/F_D, but again reservation must be taken because of possible saturation in the poles.

In summary it appears that some improvement in F_L/F_D can be obtained through changes in magnet geometry (in addition to changes in length). It would appear that for lift forces in the range of 10 kN per meter length an optionally designed, 3 m - long magnet might have a F_L/F_D in the range of 45 to 50.

3. ELECTRODYNAMIC (REPULSIVE) SUSPENSION

Work directed toward the repulsive-force suspension was of limited scope and had essentially three basic objectives. These were: (1) an evaluation of the slotted-track configuration relative to possible improvement in lift/drag ratio; (2) an evaluation of finite-height, corner guideways relative to their lift and guidance potential; and (3) the effect of canted (or inclined) levitation coils. Items (1) and (3) were not considered in our basic report (reference 1), and although item (2) was discussed, it was felt that some additional studies were needed.

3.1. Effect of Slotted Track

Two types of metallic guideways, or tracks, are currently being considered for use with repulsive-force type suspension magnets in high-speed vehicles. These are the discrete-loop track, originally proposed by Powell and Danby,[11] and the continuous sheet track (see, e.g., reference 1). A variant of the discrete-loop track is the ladder track in which the individual loops are joined together into a rigid ladder-type structure. The advantages of discrete-loop or ladder tracks are that they appear to use less metal for a specified F_L/F_D ratio, they can possibly be loaded with external inductances to improve F_L/F_D, and they may integrate more easily with the propulsion track of a linear synchronous motor (LSM). We have generally felt[1] that the increased fabrication costs of the discrete-loop or ladder track outweigh any material savings; furthermore, these tracks have the disadvantage of producing a pulsating lift component. Inductance loading is not now being considered, because of the high cost of the inductors. In addition, skin-depth considerations, which have not been adequately treated, may reduce the F_L/F_D ratio for tracks of this type below the optimistic values reported from simplified model calculations.

Another type of track which has been proposed is the slotted track. Essentially, this is a ladder track in which the "holes" in the ladder are reduced to narrow transverse slots. Such a track would not have an a priori appeal because the material savings are minimal while the additional fabrication costs are significant, but experiments by Byer, Begley and Stewart[12] indicated an improved F_L/F_D for this configuration.

We have, therefore, undertaken a series of experiments to compare the lift, drag and transverse forces on a levitation magnet suspended above a sheet track, a slotted track, and a conventional ladder track. Several different-sized levitation magnets were used, and lateral displacement of the magnet from the track centerline was also studied. A series of calculations was undertaken to support these experiments. Unfortunately, the only tractable analytic model for this analysis is the lumped-constant, ladder track model; although this model can be applied to any rung spacing, it clearly breaks down in the limit of wide rungs and narrow slots. Furthermore, the lumped-constant model ignores skin depth; this is probably not important for the thin track used in the experiments (0.635 cm), but does affect results for full-scale systems. Nevertheless, it was felt that the calculations would help in the interpretation of the experimental results.

3.1.1. Extension of Ladder Track Model

Previous calculations employing the ladder track model have been made by Ohno, Iwamoto and Yamada[13] and a simplified, single-Fourier-coefficient calculation was treated by us (see reference 2, Section 2.2.4). These treatments were for a periodic train coil moving over a ladder track with a gauge equal in magnitude to the width of the train coil. The objectives of the present calculations are to study the effects of ladder rung spacing and track gauge on levitation and drag forces and to provide a basis for analysis of the experimental results. It appeared at the outset that a calculation for an isolated, rectangular train coil would be more useful than that for a periodic train coil in the design studies of track systems using widely separated levitation coils. Furthermore, the single-levitation coil arrangement is the type of experiment which was contemplated. Accordingly, an analysis of a single rectangular coil moving at constant speed at constant elevation above a ladder track, the gauge of which is not necessarily the same as the width of the moving coil, is formulated.

A schematic of the ladder track is shown in Fig. 3.1. The equations describing the induced currents in the track loops, I_n, I_{n+1}, etc. are

$$M_o \frac{dI_n}{dt} - \sum M_k \frac{dI_k}{dt} + 2R_{\parallel} I_n + R_{\perp} [-I_{n-1} + 2I_n - I_{n+1}] = - \frac{d\Phi_n}{dt} . \tag{3.1}$$

Here M_o is the self-inductance of one track loop (loop n), and the other M_k represent mutual inductances between the k^{th} and n^{th} loops (the sign of these terms has been chosen so that the M_k are positive numbers). $R_{\parallel}$ is the resistance of one of the longitudinal elements of

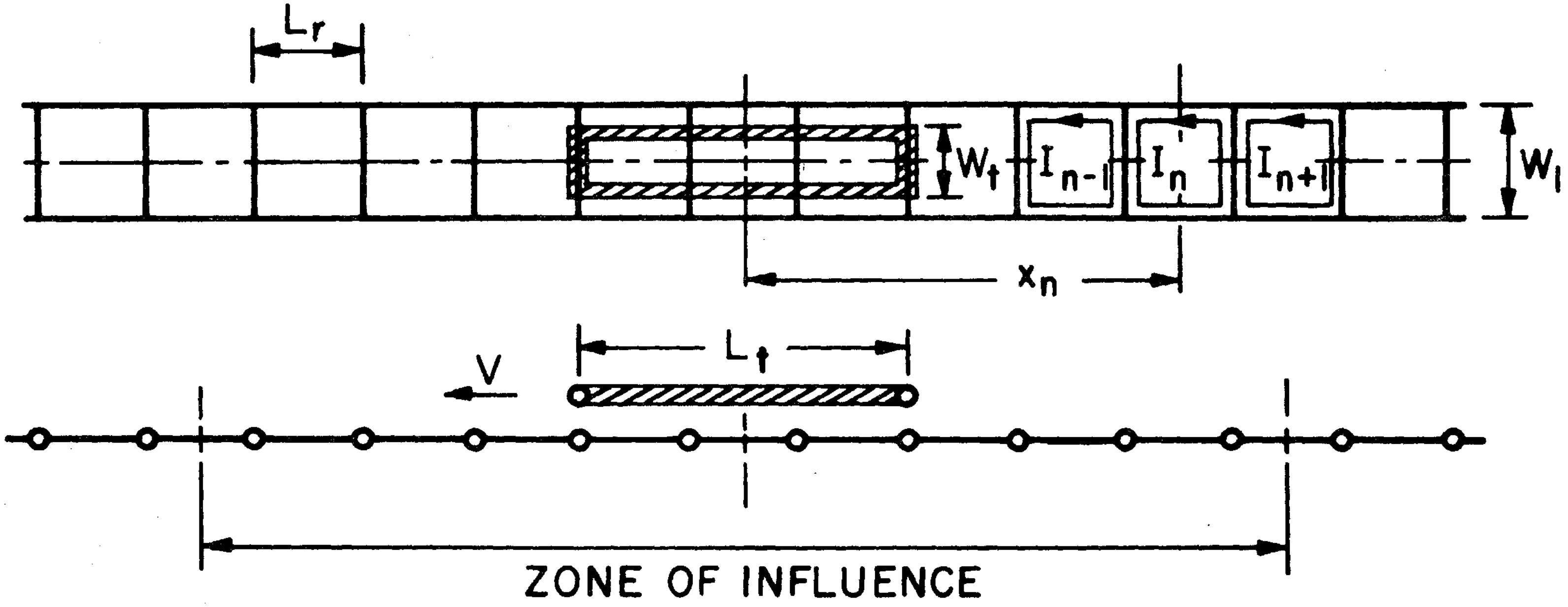

Fig. 3.1. Schematic diagram of the train coil and the ladder track.

a track loop, $R_\perp$ is the resistance of one of the rungs, and $-d\Phi_n/dt$ is the change in flux linkage of the n^{th} loop due to the moving train coil. A transformation from the time coordinate to a spatial coordinate is introduced by virtue of the constant speed condition:

$$x = vt \quad , \tag{3.2}$$

where v is the speed. Thus

$$\begin{aligned} M_o \frac{dI_n}{dx} - \sum M_k \frac{dI_k}{dx} + v^{-1} \quad [2R_{\parallel} I_n + R_\perp \{2I_n - I_{n-1} - I_{n+1}\}] \\ = - d\Phi_n/dx \\ = I_t \, dM_{tn}/dx \quad , \end{aligned} \tag{3.3}$$

where I_t is the current in the train coil and M_{tn} is the mutual inductance between the train coil (t) and loop n. dM_{tn}/dx is a known function once the geometry is prescribed, so that (3.3) represents a set of coupled equations for the I_n. For a given geometry, the solution (I_n/I_t) depends on a single parameter, ρ/v, where ρ denotes the resistivity of the track material. In general the I_n/I_t depend on $\rho/(vM_o)$, the M_k/M_o, and on dM_{tn}/dx.

In order that appropriate initial conditions be employed for the solution of (3.3), the infinite track system is replaced by a semi-infinite strip, the leading edge of which is placed at a point beyond the zone of influence of the moving coil, i.e., beyond a point where the x-component of the interaction force between the leading track loop and the moving train coil may be considered negligible. The track is moved forward each integration cycle until the desired geometry is obtained and a steady state is achieved. By virtue of this zone of influence concept, it is only necessary to retain those track loops within the zone during the numerical integration. This amounts to reindexing the track loops each time the trailing rung of a loop passes out of the zone of influence.

Since the matrix of coefficients based on self and mutual inductances is invariant throughout the entire computing process, the actual solution involves only a sequence of matrix multiplications and additions. Lift and drag force components, as well as lateral force components in the case of a lateral offset of the moving coil, can all be determined concurrently with the integration process. The lift force is given by

$$F_L = \langle I_t \sum I_n (dM_{tn}/dz) \rangle \quad , \tag{3.4}$$

and the drag F_D by

$$F_D v = P_{loss} = \langle \sum (2R_{\parallel} I_n^2 + R_{\perp} (I_n - I_{n-1})^2) \rangle \quad , \tag{3.5}$$

where the sum is over the zone of influence. $\langle \ldots \rangle$ denotes a time average which, because of the constant speed condition, may be replaced by a space average. The transverse force F_T can be calculated from an equation similar to (3.4). A program,[14] named LADDER, was prepared in BASIC language, for use on time sharing terminals, for solution of (3.3) and calculation of the forces.

A. Results for the Test Model

A fairly extensive series of calculations has been completed for a model representing the experimental setup used for this research program. A composite sketch of the track geometry is shown in Fig. 3.2. In the experiments the ladder track forms the rim of a wheel which rotates beneath the stationary levitation coil. The composite sketch shows three different sized slots; of course, during any single run the slots are all the same size. For the purpose of numerical analysis, the centerline of all linear elements are used to define coil dimensions.

Inductance calculations were carried out using standard expressions for the inductance between line elements as given by Grover.[15] During the course of this study it was noted that extreme care must be exercised in estimating the mutual inductance between track loops when they share a common element. Expressions for the self inductance (M_o) are fairly well standardized, but problems exist in the calculation of M_1. A procedure was followed which treats the contribution to M_1 from the flux in the common element on the same basis as for that in M_o. This procedure seems satisfactory but may be in error for very small rung spacings. A plot of the inductance values is shown in Fig. 3.3.

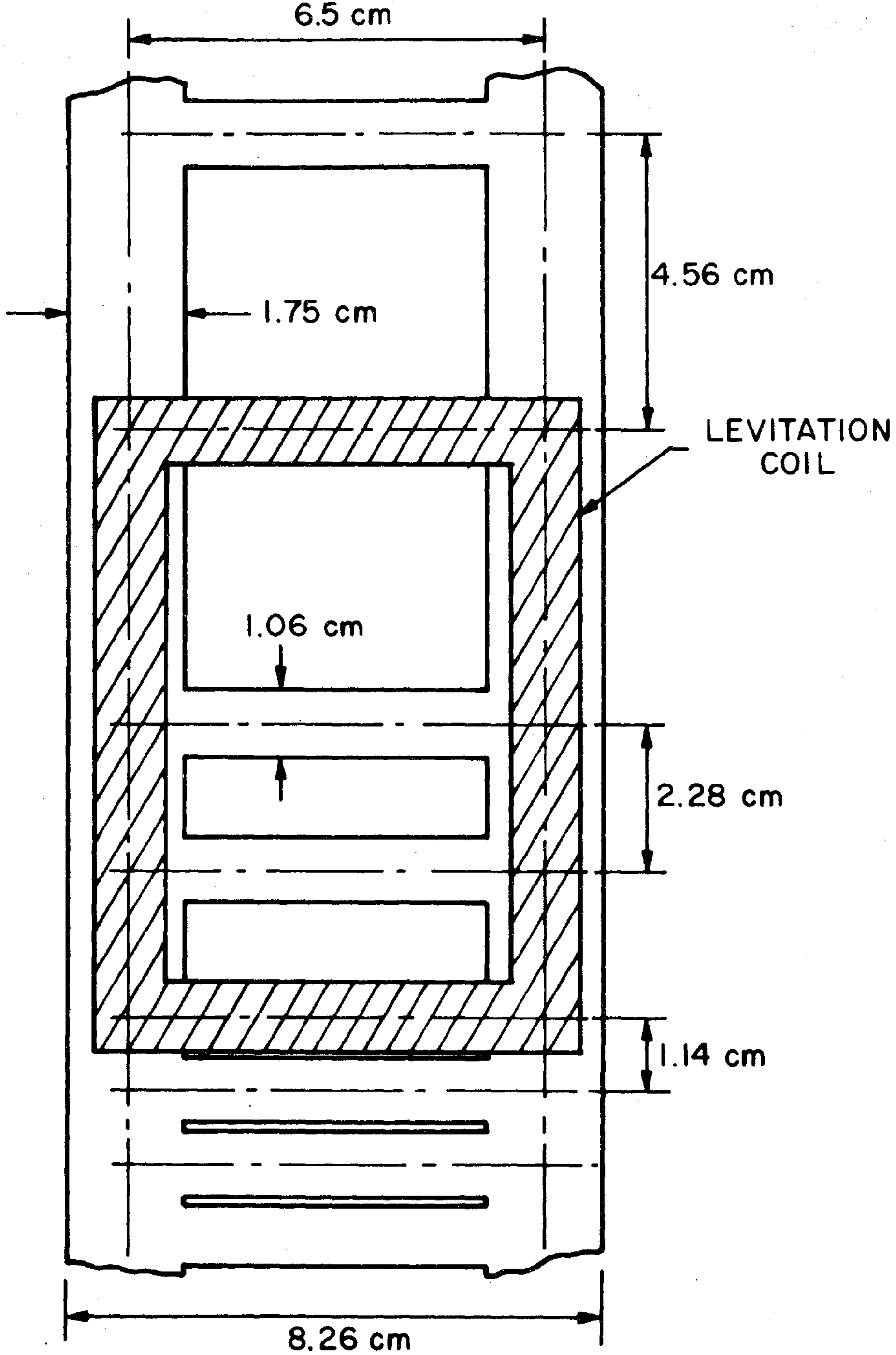

Fig. 3.2. A composite sketch of the track geometry used for the slotted and ladder tracks. Three different sized track holes, corresponding to different rung spacings, are shown.

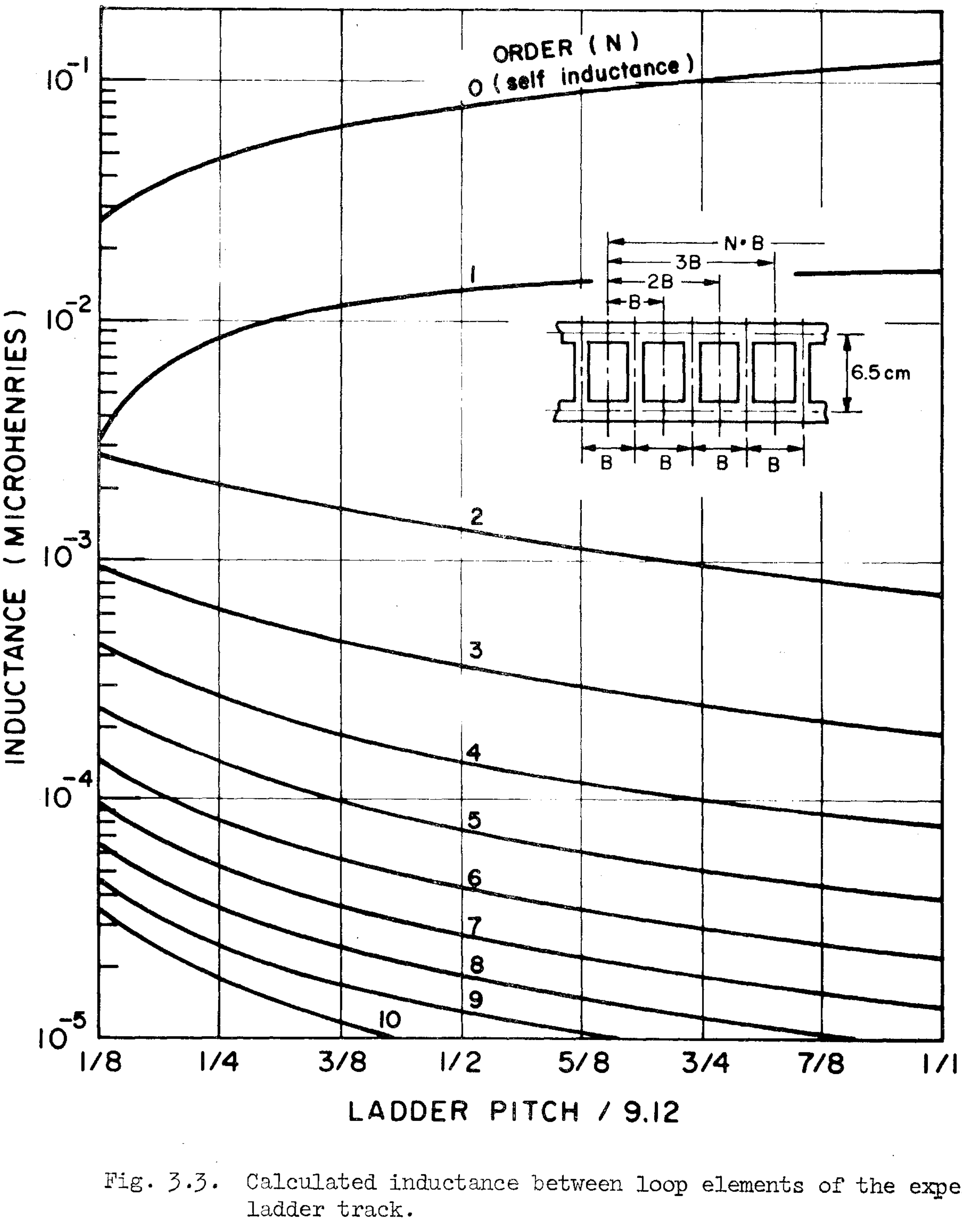

Fig. 3.3. Calculated inductance between loop elements of the experimental ladder track.

Table 3.1 Summary of Levitation Force Characteristics for a Rectangular Coil Moving at Constant Elevation over a Ladder Track

Train Coil: 9.12 cm long and width as shown
Ladder Track: 6.5 cm gauge with rung spacing as shown. (6061-T6 aluminum alloy)
Longitudinal member: 1.75 x 0.635 cm
Transverse member: 1.064 x 0.635 cm
Train Coil Elevation: 2.54 cm
Speed: 100 m/s

Coil Width (cm)	Rung Spacing (cm)	Lateral Offset (cm)	F_L/F_D	F_T/F_L	F_L (*)	Pulsation in Lift (%)
3.96	4.56	0	3.88	0	0.1527	13.3
	2.28	0	4.85	0	0.1814	0.8
	1.14	0	6.44	0	0.1820	0.1
6.50	4.56	0	3.89	0	0.3220	13.6
		0.51	3.82	0.182	0.3055	13.8
		1.27	3.51	0.457	0.2366	14.8
6.50	2.28	0	4.86	0	0.3833	0.9
		0.51	4.78	0.176	0.3639	0.6
		1.27	4.41	0.440	0.2833	0.9
6.50	1.14	0	6.47	0	0.3848	0.1
		0.51	6.36	0.174	0.3654	0.1
		1.27	5.88	0.436	0.2847	0.1
9.04	4.56	0	3.28	0	0.3382	15.5
	2.28	0	4.14	0	0.4072	1.0
	1.14	0	5.54	0	0.4096	0

*Newtons per $(kNI)^2$

Referring to Table 3.1 it may be noted that the lift coefficient tends to a limiting value as the rungs are moved closer to each other. Also, higher lift coefficients are generated by a wider moving coil. For the range of values studied so far a saturating tendency is also noted. For example, the lift coefficient varies from 0.1527 newtons per (kilo-ampere-turns)^2 for coil of width 3.96 cm, to 0.322 for a coil width of 6.50 cm, and to 0.3382 for a coil width of 9.04 cm (for a rung spacing of 4.56 cm). Also of interest is the fact that the transverse force F_T is a destabilizing force.

The fraction of material in the ladder track relative to that of a solid track varies from 0.559 for a rung spacing of 4.56 cm to 0.962 for a 1.14 cm rung spacing. For full scale working systems this factor must be included in optimization studies.

B. Results for a Full Scale System

Calculations have also been made for a representative full scale track system with the following characteristics:

Train Coil: 3.0m long by 0.5m
Track Gauge: 0.75m
Rung Spacing: 1.50, 1.00, 0.75, 0.60m
Track Element: 0.08m square (for both longitudinal and transverse elements). 6061-T6 Al alloy
Coil Elevation: 0.3m

Two speeds were considered: 10 m/s and 134 m/s. Results for lift, drag, and pulsation are summarized in Table 3.2. These exhibit features similar to those obtained for the smaller size configuration described in Table 3.1, except for the F_L/F_D ratio which shows the opposite trend as the rung spacing is varied. Additional studies show, however, that F_L/F_D goes through a minimum at intermediate rung spacings, and that

Table 3.2 Summary of Lift and Drag Forces on a 3.0 x 0.5m Rectangular Coil Moving at Constant Speed over a Ladder Track

Speed m/s	Rung Spacing m	F_L/F_D	F_L $N/(kNI)^2$	Pulsation (%) in Lift	Pulsation (%) in Drag
10	1.50	2.50	0.1103	66.5	54.2
	1.00	2.36	0.1327	35.7	40.8
	0.75	2.20	0.1454	20.8	28.6
	0.60	2.03	0.1525	13.2	19.4
134	1.50	36.0	0.5247	23.0	377.5
	1.00	32.3	0.6261	11.1	223.0
	0.75	28.9	0.7184	6.1	126.6
	0.60	25.7	0.8148	3.7	74.3

F_L/F_D increases again at very small rung spacings, although it is not found to be better than the solid track. Thus, to get good F_L/F_D performance one must go either to very small rung spacings where the material savings are small, or to relatively large rung spacings where the loss of lift is substantial and the pulsation component rather large.

The fraction of material in the ladder track relative to a solid track varies from 0.236 for the 1.50 m rung spacing to 0.300 for a 0.60 m rung spacing.

3.1.2. Experimental Studies

In designing the experiments for the slotted and ladder track we tried to utilize the experimental equipment developed in previous programs.[1,2] In this manner not only could the overall cost of the program be kept low, but since we were familiar with the equipment we knew its limitations and were able to obtain meaningful results in a shorter period of time.

To this end we settled on a 61 cm diameter, 6061-T6 aluminum rim, 6 mm thick and 82.6 mm wide, designed to be used with the previously wound coils.[2] The aluminum rim was fastened to a phenolic laminate wheel (49 cm dia.) and powered by a 3 hp variable speed d.c. motor. (The previous solid aluminum wheel was 24 inches in diameter;[2] thus all previously developed experimental apparatus, including dewar and superconducting coils could be employed.) In the test program, measurements were first made on the aluminum rim, then slits were machined through the rim, and finally the aluminum between every other pair of slits was removed, converting the slit track to a ladder track (with 2.28 cm rung spacing).

A composite sketch of the track configurations is shown in Figure 3.2, and a picture of the slit track is shown in Figure 3.4. In this latter figure, the dewar is removed, showing the coil curved to fit the rim. The rod to which the coil is mounted is freely suspended from the lift transducer so that both lift and drag forces are transmitted by the rod. The drag is measured by this support rod pressing against the drag transducer (partially hidden, near the top of the figure).

The experimental procedure followed for each of the three tracks (sheet, slit, and ladder) consisted of measuring the velocity dependence of the lift and drag forces for a given height (or heights) for each of the two coils (67.8 × 93.4 mm and 42.4 × 93.4 mm). Some of the

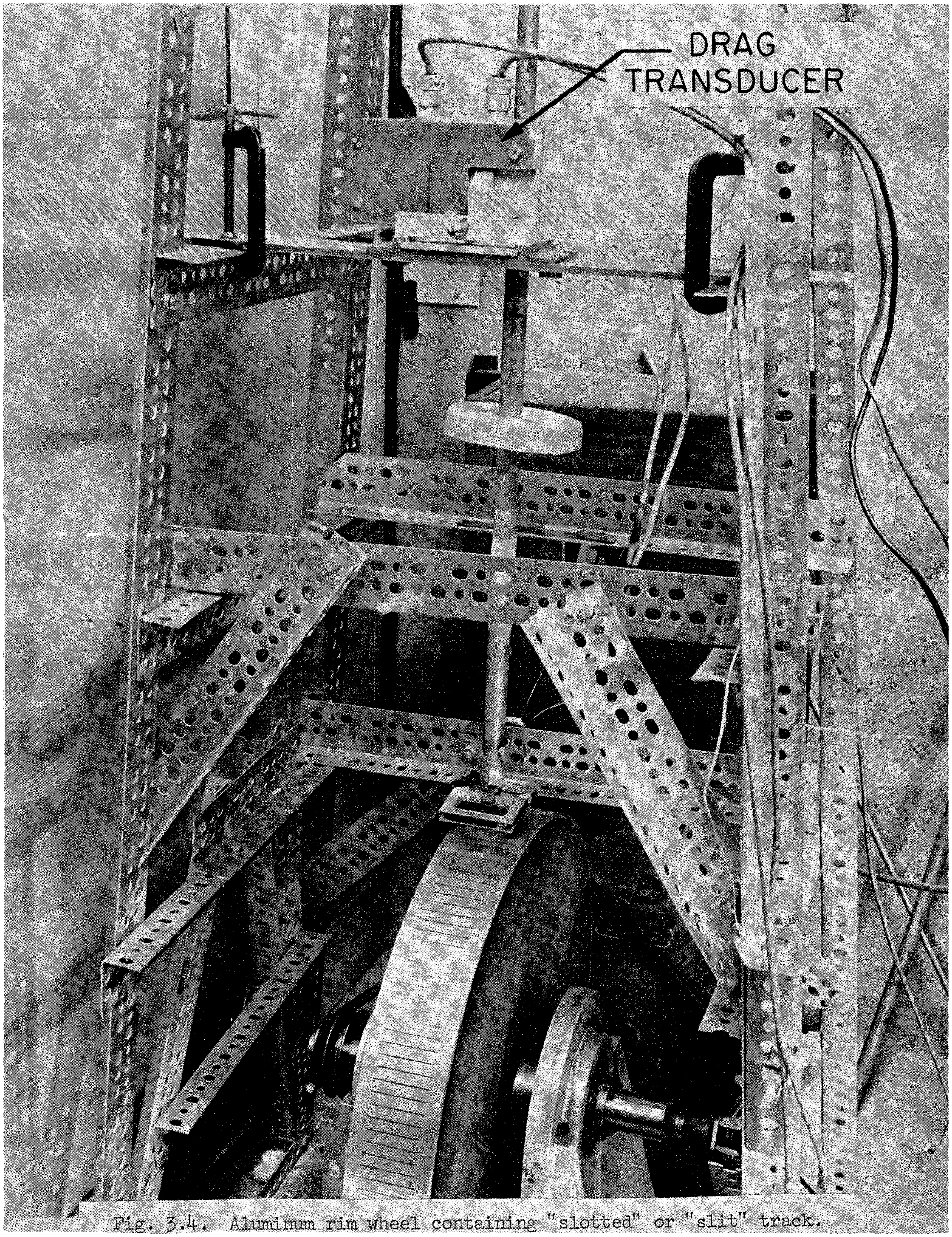

Fig. 3.4. Aluminum rim wheel containing "slotted" or "slit" track.

results of these measurements are shown in Figures 3.5 to 3.8, and the high-speed results are summarized in Table 3.3. For the slit and ladder tracks the optimum train coil is one with approximately the same width as the track; a wider coil has a poorer F_L/F_D whereas a narrower coil gives a reduced lift (See Tables 3.1 and 3.3).

TABLE 3.3. Experimental Study of the Sheet, Slit, and Ladder Tracks

Coil A: 67.8 × 93.4 mm

Coil B: 42.4 × 93.4 mm

Track: 6061-T6 Aluminum

Speed: 100 m/s

Train Coil Elevation: 26.9 mm

Track	Coil	F_L $[N/(kNI)^2]$		F_L/F_D	
		Experiment	Theory⁺	Experiment	Theory⁺
Sheet	A	*	0.389	6.35	7.8
	B	0.223	0.205	7.75	7.8
Slit	A	0.318	0.344	5.5	6.47
	B	0.137	0.163	5.43	6.44
Ladder (2.28 rung spacing)	A	0.293	0.342	4.4	4.86
	B	0.144	0.162	4.55	4.85

* Coil operated in persistent mode. Exact current level unknown.

⁺ Theory for sheet track is for an infinitely wide plate. Theory for slit and ladder track from Table 3.1 (adjusted for small changes in coil dimensions and height).

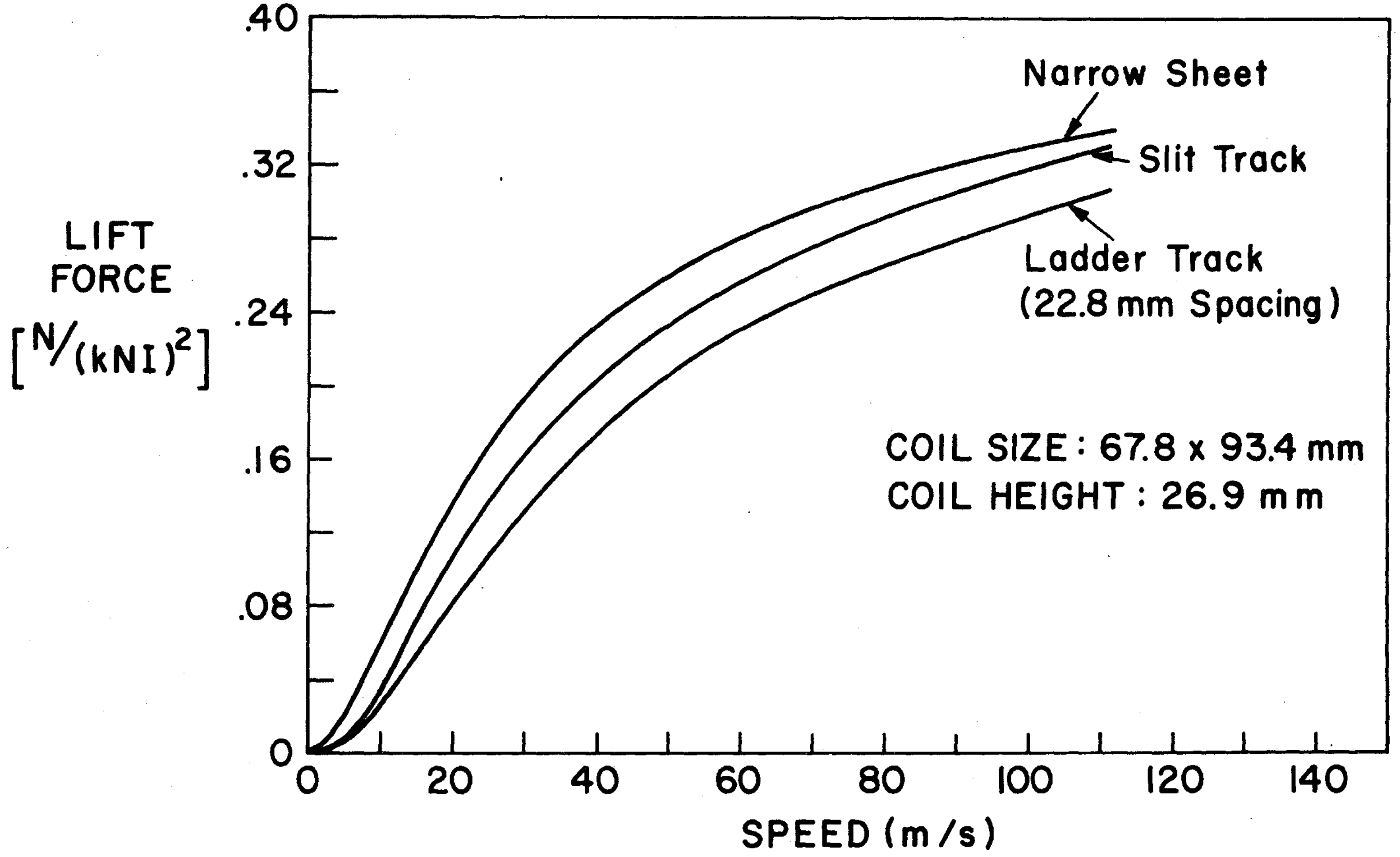

Fig. 3.5. Lift force versus speed for three different tracks.

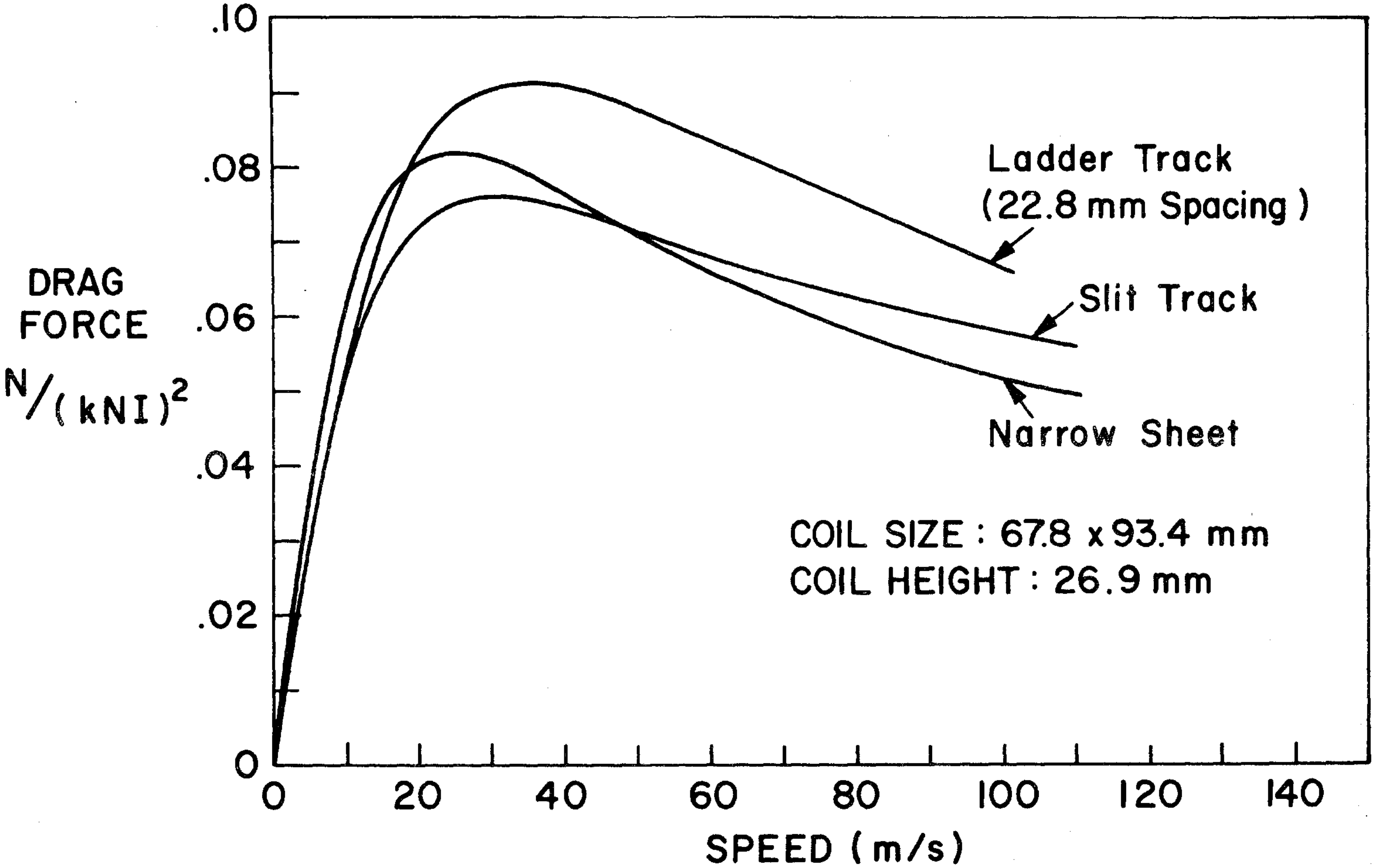

Fig. 3.6. Drag force versus speed for three different tracks.

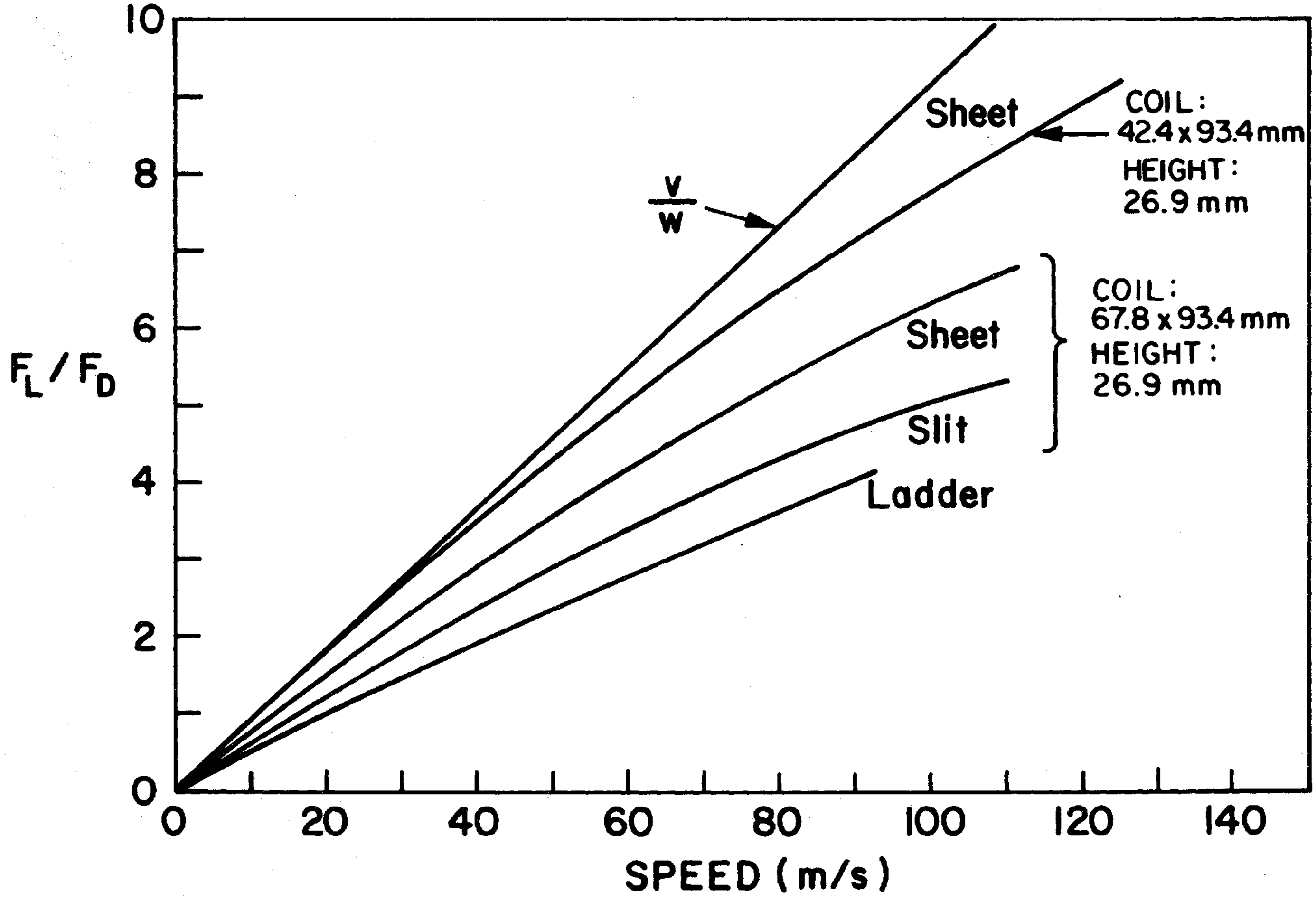

Fig. 3.7. Lift-to-drag ratio versus speed for three different tracks.

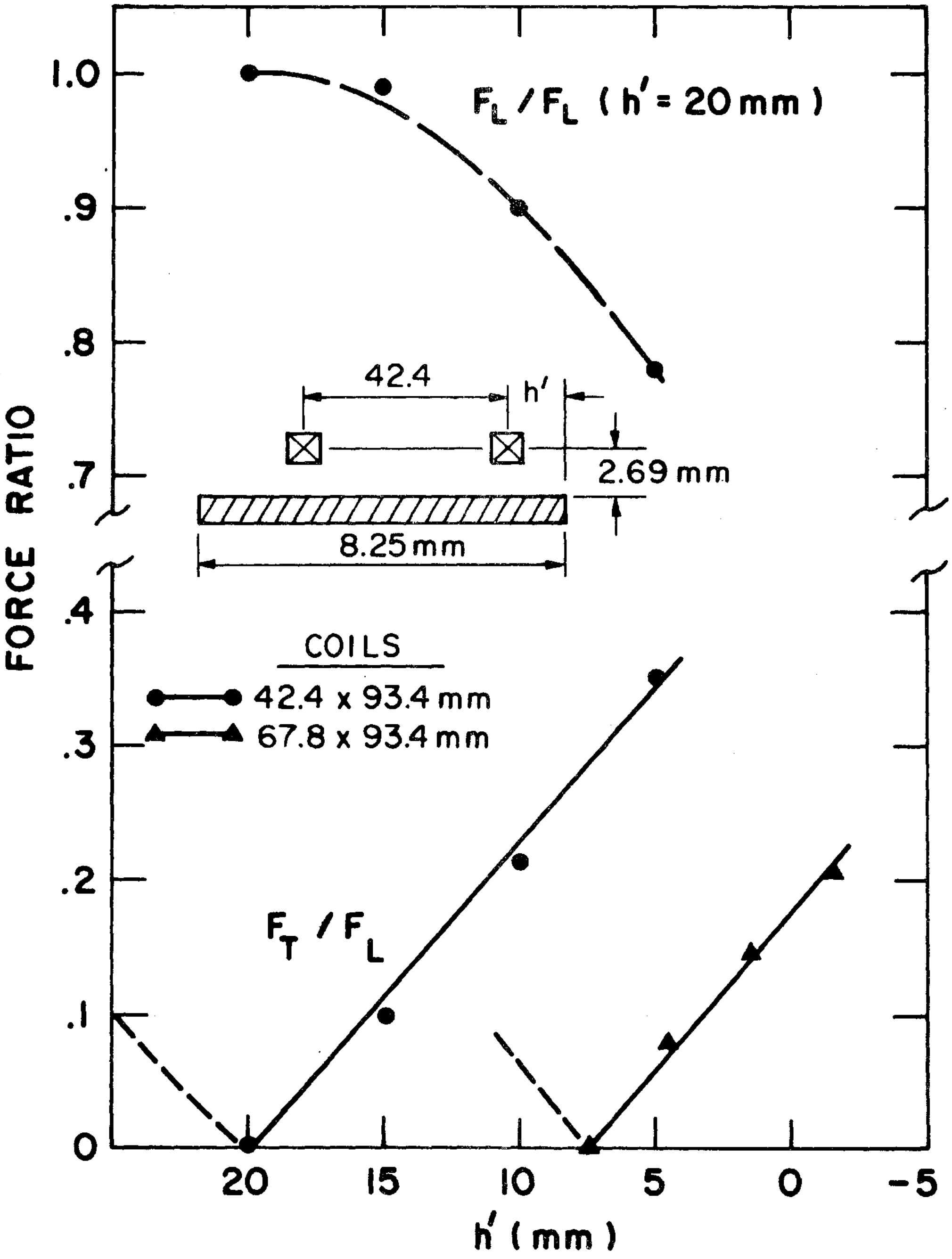

Fig. 3.8. Transverse force on a displaced coil above the sheet track (experimental).

TABLE 3.4. The Effective w Parameter of Various Tracks (Using Coil A)

Track	w (m/s)
Infinitely-wide, thin plate	11.0
Experimental (finite-width) plate	13.2
Slit track	16.0
Ladder track (2.28 cm rung spacing)	19.6

The lift and drag force results of Figures 3.5 and 3.6 show that as the track is successively converted from the thin plate, to the slit, and to the ladder, there is a shifting of the drag peak to higher speeds, and the lift force curve also is displaced toward higher speeds. These are characteristics of a larger w parameter ($w = 2/\mu_o \sigma T$ in thin plate theory[2]). To the extent that these experimental results can be interpreted in this manner, the effective w corresponding to each of the tracks is easily obtained from the F_L/F_D curves of Fig. 3.7. These results are tabulated in Table 3.4. Note that for the larger of the two coils the finite width of the track causes an increase of w (decrease of F_L/F_D) over that of the infinitely-wide, thin plate, in contrast to the narrow coil where hardly any decrease of F_L/F_D from that of the infinitely wide plate is noted (see Fig. 3.7).

The ratio of w's for the plate versus ladder, 0.67, is very close to the 0.69 value which is the ratio of the amounts of aluminum in these two tracks. In other words, instead of making the complicated ladder track, similar results could have been obtained from using a thinner sheet track with the same amount of aluminum! For the smaller of the two coils the agreement between the w ratio and the aluminum ratio of the two tracks is not so good; here (for coil B) a thinner sheet track with an equivalent amount of aluminum gives better performance than the ladder track.

3.1.3. Comparison of Theory and Experiment

Table 3.3 summarizes the experimental results at high speed (100 m/s) for each of the coils above each of the three tracks (sheet, slit, and ladder), and compares these results with theoretical predictions. The theory for the sheet track is that for an infinitely-wide plate[2] whereas the experiment deals with a finite-width track; it appears, however, that the track width is adequate for the narrow coil (coil B). The theory for the slit and ladder tracks is that developed in Section 3.1.1; although this model can be applied to a ladder track of any rung spacing, it is not a particularly good model for the "slotted" (or slit) track. Experimentally as well as theoretically, the performance of the sheet track (as measured by F_L/F_D) is better than that of the slit track. This result is in conflict with preliminary results of Byer, Begley and Stewart;[12] however, in the published version of their report these authors only claim similar F_L/F_D ratios for their slotted and sheet discs. They also mention that their drag force measurements are not highly accurate since "...the apparatus drag force is an order of magnitude larger than the induced magnetic drag force."

We also find that the performance of the slit track is better than that of the 2.28 cm rung-spacing, ladder track. The conclusion that one is drawn to as a result of this work is that when aluminum is taken out of the track, the performance of the system is degraded. If we renormalize the sheet and ladder tracks to the same amount of aluminum per unit length, we find that the performance of the two tracks are about the same. On the other hand, previous calculations[13] for ladder tracks indicate that at large rung spacings the performance of a ladder track can be superior to that of a sheet track* (when compared on an equal aluminum basis); of course, such a ladder track has the disadvantage of a substantial pulsating component in the lift force.

Fig. 3.8 shows the transverse force obtained through lateral displacement of the coil from the track centerline for the sheet track. This measurement was not made for the slit or ladder tracks, but calculations for the ladder track are given in Table 3.1. The slope of the F_T/F_L curve from the Table is about 50 percent larger than the corresponding slope in Fig. 3.8. The transverse force is a destabilizing force for the slit and ladder tracks, as well as for the flat, sheet track.

---

* Although Table 3.2 shows relatively modest lift-to-drag ratios (26 to 36) for 134 m/s operation, F_L/F_D can be increased substantially by going to track elements of larger cross-section.

3.2. Corner Guideway Studies

In this and the following sections we return to studies of the continuous, sheet-type track. In this section we are concerned with the guidance forces produced by L-shaped, corner guideways on standard levitation coils in the vehicle. This topic was treated in our earlier report (reference 1, Section 2.2), but some aspects of that study were felt to be incomplete. In particular, we wished to determine how the guidance force depends on coil aspect ratio (ratio of length to width) and how it depends on height of the side panel of the guideway. The latter determination is particularly important because it affects the amount of aluminum required for the guideway, and ultimately guideway cost.

In reference 1 there appeared to be some discrepancies between theoretically-calculated guidance forces and those determined experimentally from inductance measurements for a coil moving in a right-angle, corner guideway. Specifically, Fig. 2.4 of that report showed that the guidance force, F_G, on a 1/2 x 3 m coil is substantial and will exceed the lift force under some conditions. On the other hand the guidance force on a 2 x 4 inch coil as determined from inductance measurements (Fig. 2.12 of reference 1) appeared to be rather meager. There are a number of differences between the two situations: the coils have a different aspect ratio, and the height of the vertical sections of the corner guideway are different (infinite for Fig. 2.4 and quite limited for Fig. 2.12).

The situation has now been fairly well resolved although there are still some differences between theory and experiment. Calculations of lift and guidance force for various aspect-ratio coils in a corner guideway have been carried out (for the high-speed limit). The ratio of F_G/F_L is much larger for long coils (6:1 aspect ratio) than for shorter coils (2:1 aspect ratio). Long coils are preferred for a suspension system because they produce a better F_L/F_D ratio; as a side benefit they also produce a higher F_G/F_L.

3.2.1 Inductance Measurements on Finite-Height Corner Guideways

Inductance measurements on a 39 x 89 mm coil in a aluminum corner guideway were carried out as described in Sect. 2.2 of reference 1. The first guideway measured had a vertical panel 150 mm high, which is quite large compared to the suspension height (~ 18 mm). These data are shown in Fig. 3.9. The agreement between theory and experiment is fairly good when h and h′ are both greater than 18 mm, but there are significant deviations when one of these distances is small.* Note that because of the finite bundle size of the coil, the smallest gaps (h or h′ = 7.2 mm) corresponds to the coil almost making contact with the guideway. The disagreement at close gaps is believed to be due to this finite bundle size, since the calculations are for coils with infinitesimal bundle size. At the larger gaps, the inductance measurements give slightly lower F_G/F_L values than one obtains from calculation; however, these discrepancies appear to be within the combined error of measurement and graphical differentiation.

Fig. 3.10 shows the dependence of coil inductance on the guidance gap for several different side panel heights. The guidance force is proportional to the slope of these curves. We note that there is very little change in guidance force between the case with the 150 mm high side panel and the 25 mm one. However, when the side panel is reduced to 19 mm (only slightly higher than the mid-plane of the coil) the guidance force is reduced by about a factor of 2. It thus appears that our earlier suggestions for truncating the side panel height were adequately conservative.

The results of this study give no indication that theoretically <u>derived values</u> of F_G/F_L are in serious error provided, of course, that the

---

* h and h′ are defined in Fig. 3.9.

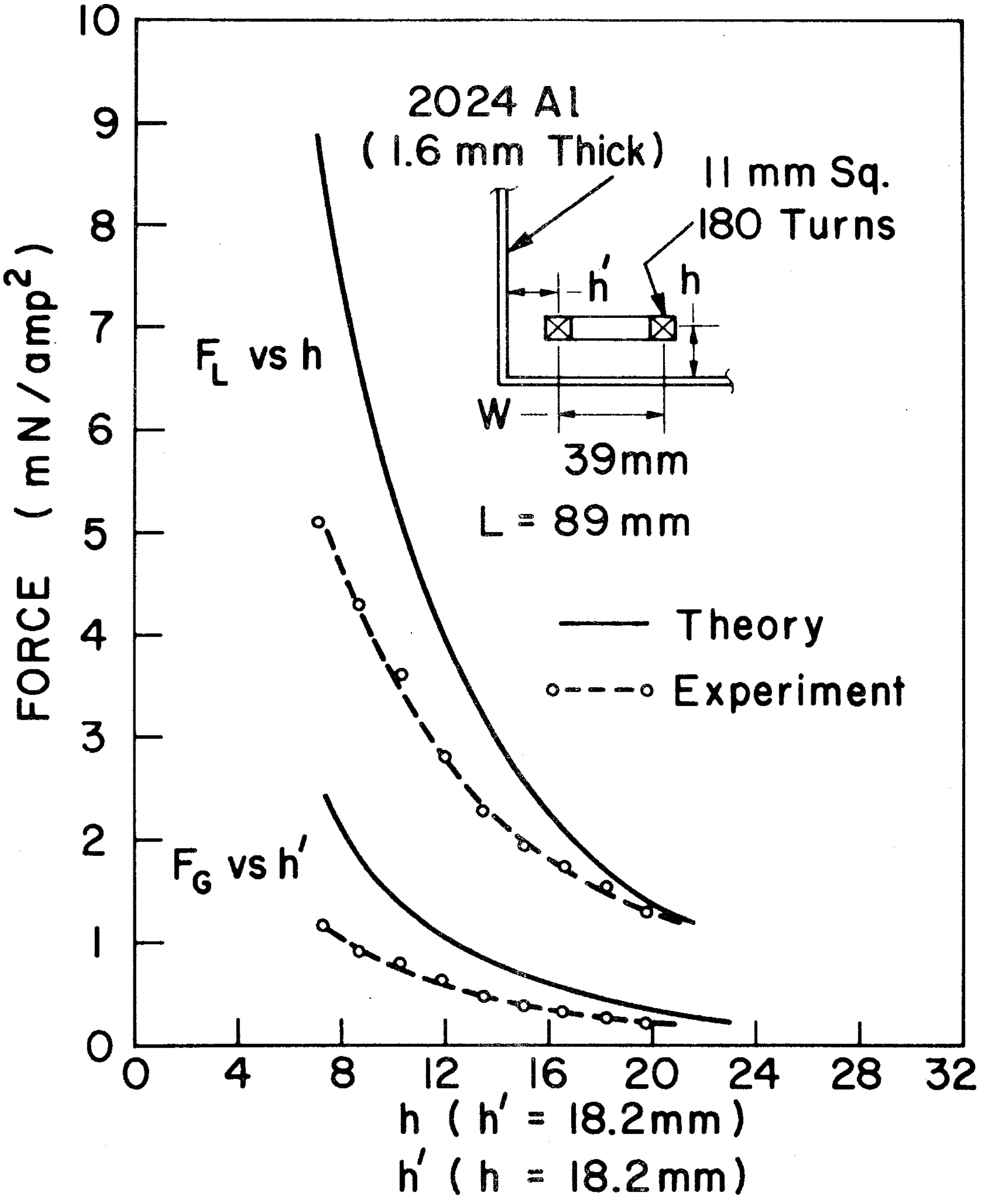

Fig. 3.9. Force from inductance measurements on a coil in a corner guideway.

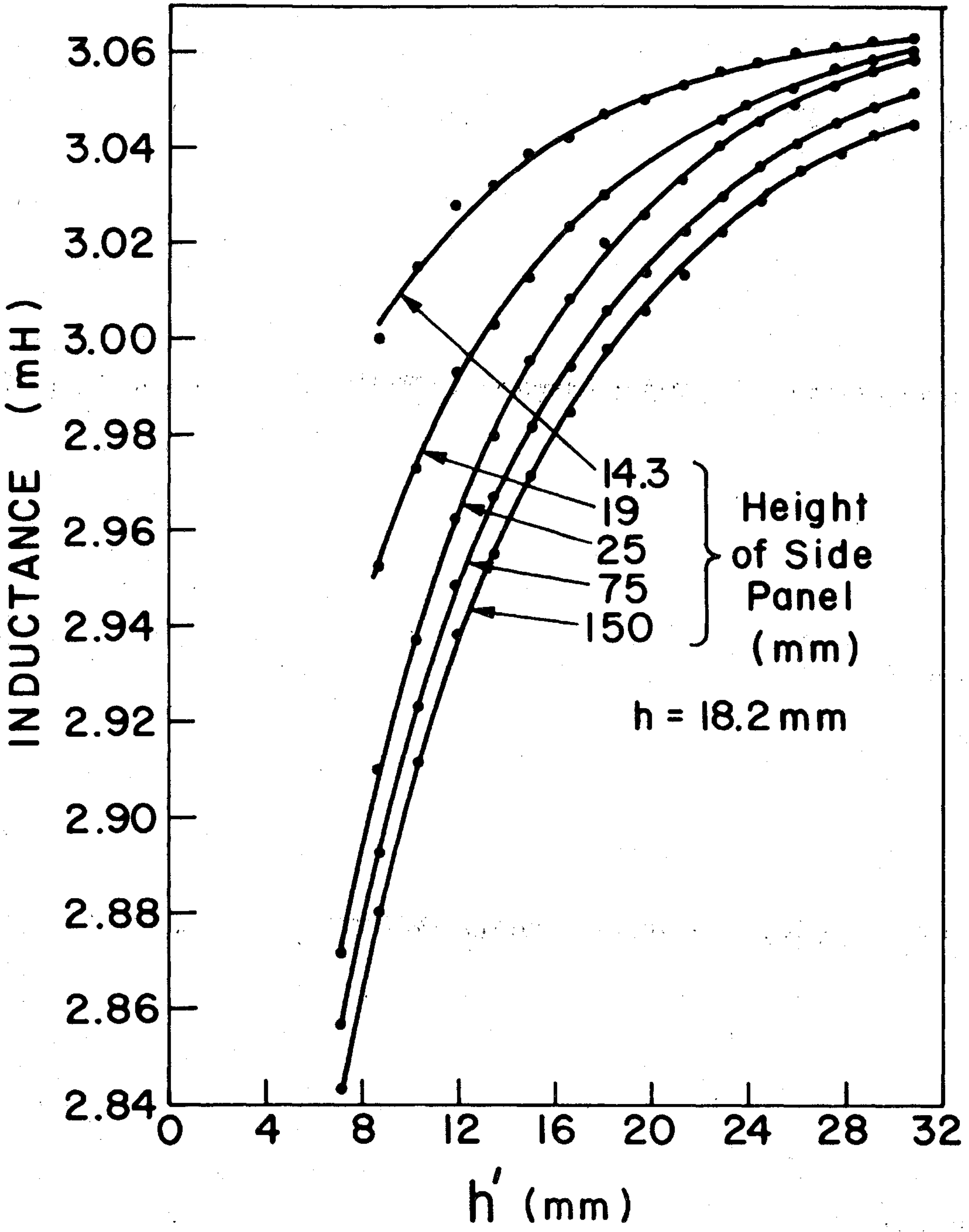

Fig. 3.10. Inductance measurements in a corner guideway. Dependence on side panel height.

side-panel height is not made too small. Thus, the design information provided in our earlier report[1] should be satisfactory.

3.3. Use of Canted Levitation Coils

Previous calculations of lift, guidance, and drag forces on flat, rectangular levitation coils have been applied to situations where the levitation coil moves in a plane parallel to one of the guideway surfaces. This geometry has been favored for levitation coils because it provides the maximum levitation force for a fixed magnet clearance. It has occasionally been suggested that canted coils may provide advantages in some situations (such as increased guidance from a single coil in a corner guideway). Furthermore, dynamic excursions of the vehicle will produce small-angle canting of the coils.

We have, therefore, made calculations of the force on a rectangular coil moving above a conducting surface when the coil is canted about one of the coil axes. The results presented Figs. 3.11 - 3.13 are for an infinitely-wide, flat, conducting-plate guideway and are for the high-speed limit. For this geometry there is no lateral force, and in this limit the drag force is zero. The levitation force was obtained by first finding the mutual inductance between the coil and its image (using standard expressions for the inductance between line elements as given by Grover[15]) and then numerically differentiating the inductance vs. distance to find the force. Fig. 3.11 shows the lift force F_L on a 0.5 x 3 m coil when it is canted about the long axis of the coil. Each curve is for a constant height h of the cant axis. The results are normalized to 1000 ampere turns. We note that in the small angle region the effect of canting is a small effect. For h in the neighborhood of 0.3 m the effect of canting the coil is to increase the lift; however, this results from the fact that the cant axis is held at constant

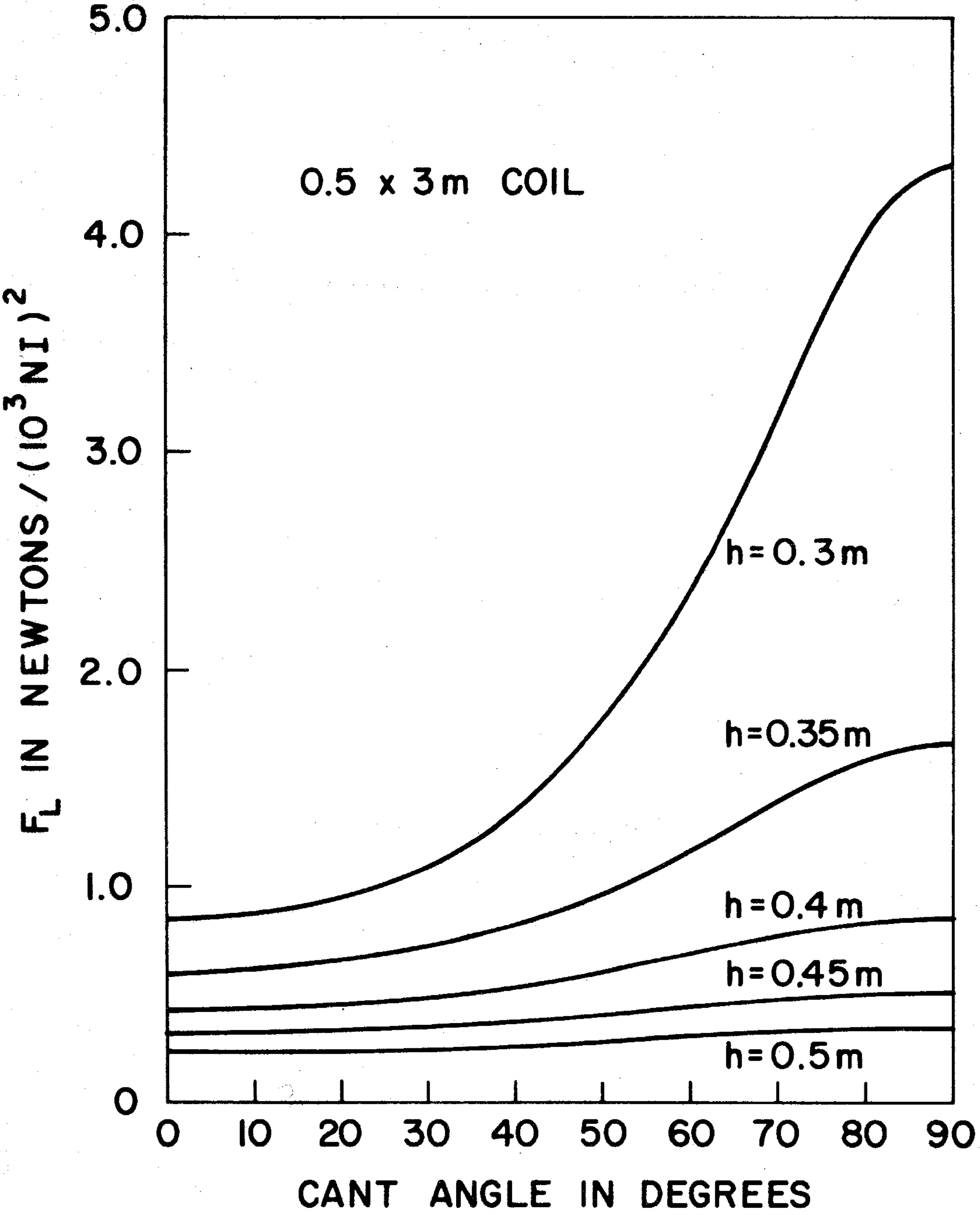

Fig. 3.11. Force on a canted coil above a flat guideway.

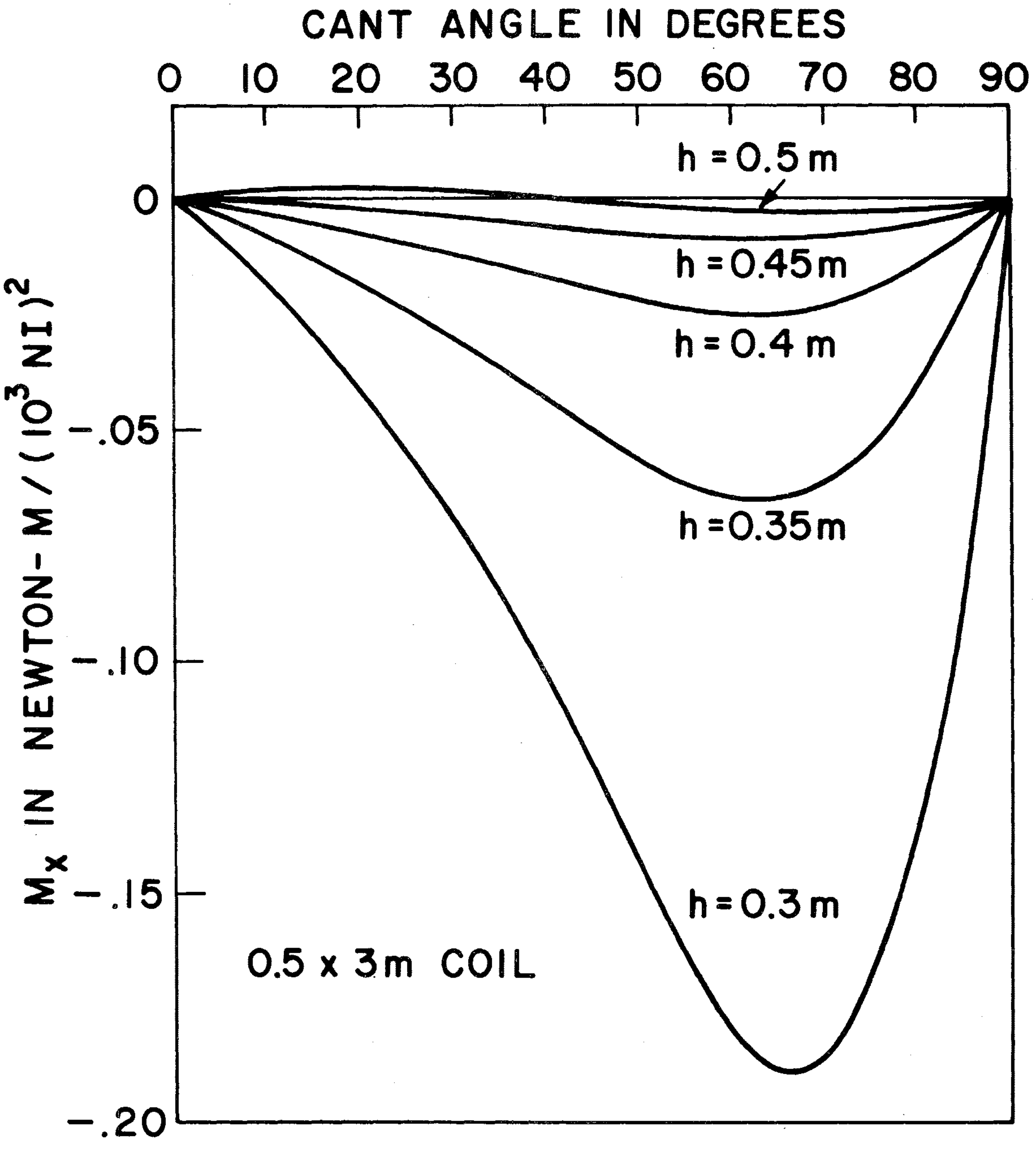

Fig. 3.12. Torque on a canted coil above a flat guideway.

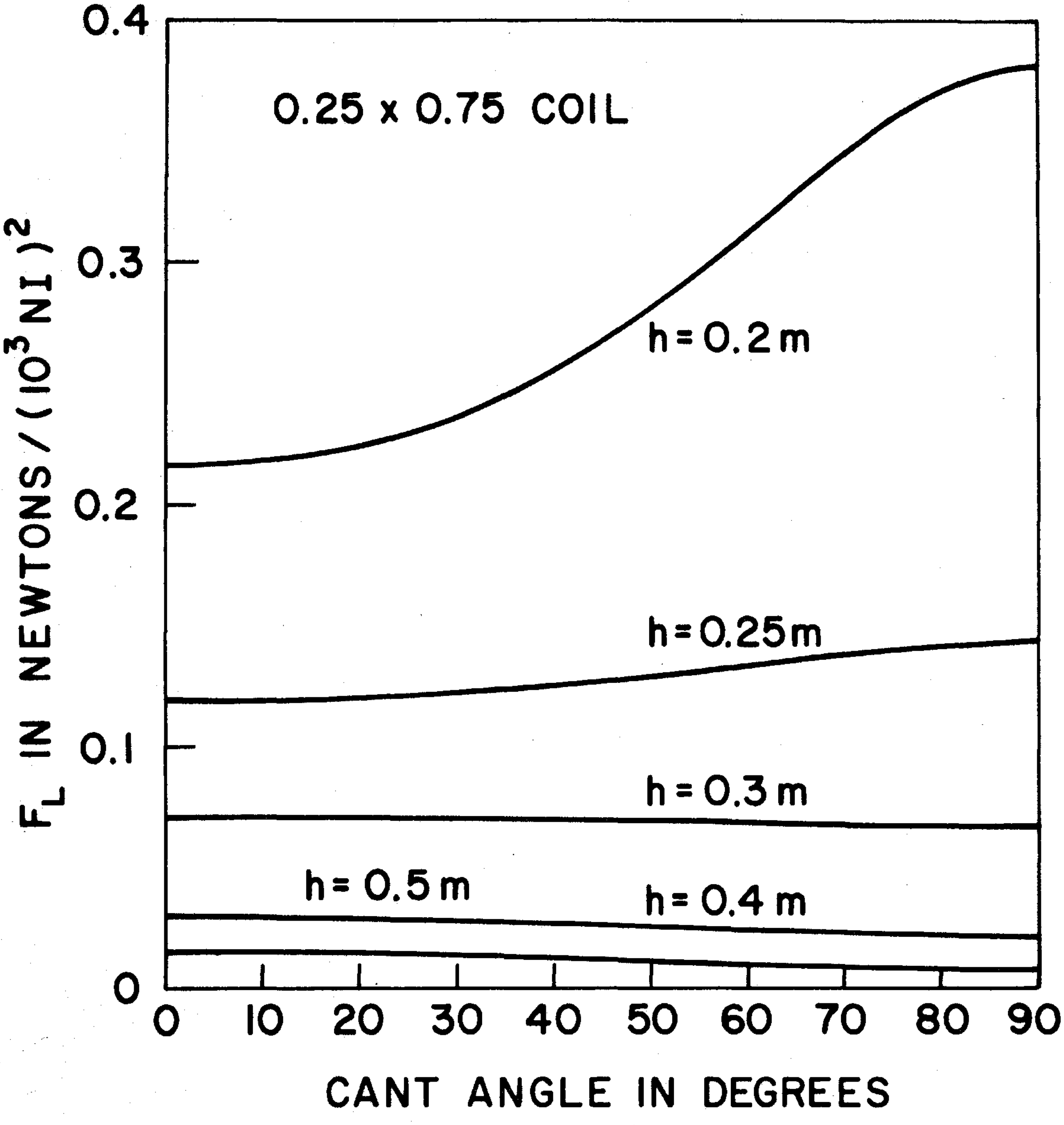

Fig. 3.13. Same as Fig. 3.11; smaller coil.

height. If constant clearance is maintained, the lift force F_L will always decrease as the cant angle increases.

Fig. 3.12 shows the torque on a 0.5 x 3 m coil when it is canted about the long axis of the coil. Again each curve is for constant height h of the cant axis. Fig. 3.13 shows the lift force on a smaller coil, 0.25 x 0.75 m, as it is canted about the long axis of the coil.

The results presented here may be applied to coils of different size through simple scaling procedures. If all coil dimensions and the height h are increased by a common factor, the force F_L per ampere-turn is not changed.

Figs. 3.14 and 3.15 provide results for the right-angle-corner, conducting guideway in the high-speed limit. The cant angle θ is defined in Fig. 3.14; a negative cant angle means that the coil is inclined toward the corner. Fig. 3.14 shows the lift force F_L and the guidance force F_G on a 0.5 x 3 m coil when it is canted about the long axis of the coil. The height of the cant axis above the horizontal surface is 0.3 m and the distance between the cant axis and the vertical panel is 0.45 m. At zero cant angle the result for F_G/F_L agrees with the prediction of Fig. 2.4 of reference 1. Fig. 3.14 also indicates that some improvement in the F_G/F_L ratio can be achieved by operating at -15° cant angle and increasing the coil elevation to maintain the desired clearance.

Fig. 3.15 shows F_L and F_G on a 0.25 x 0.75 m coil which it is canted about its long axis. The height of the cant axis is 0.3 m and the distance between the axis and vertical panel is 0.425 m. Similar scaling procedures apply here as for the flat, conducting plane guideway.

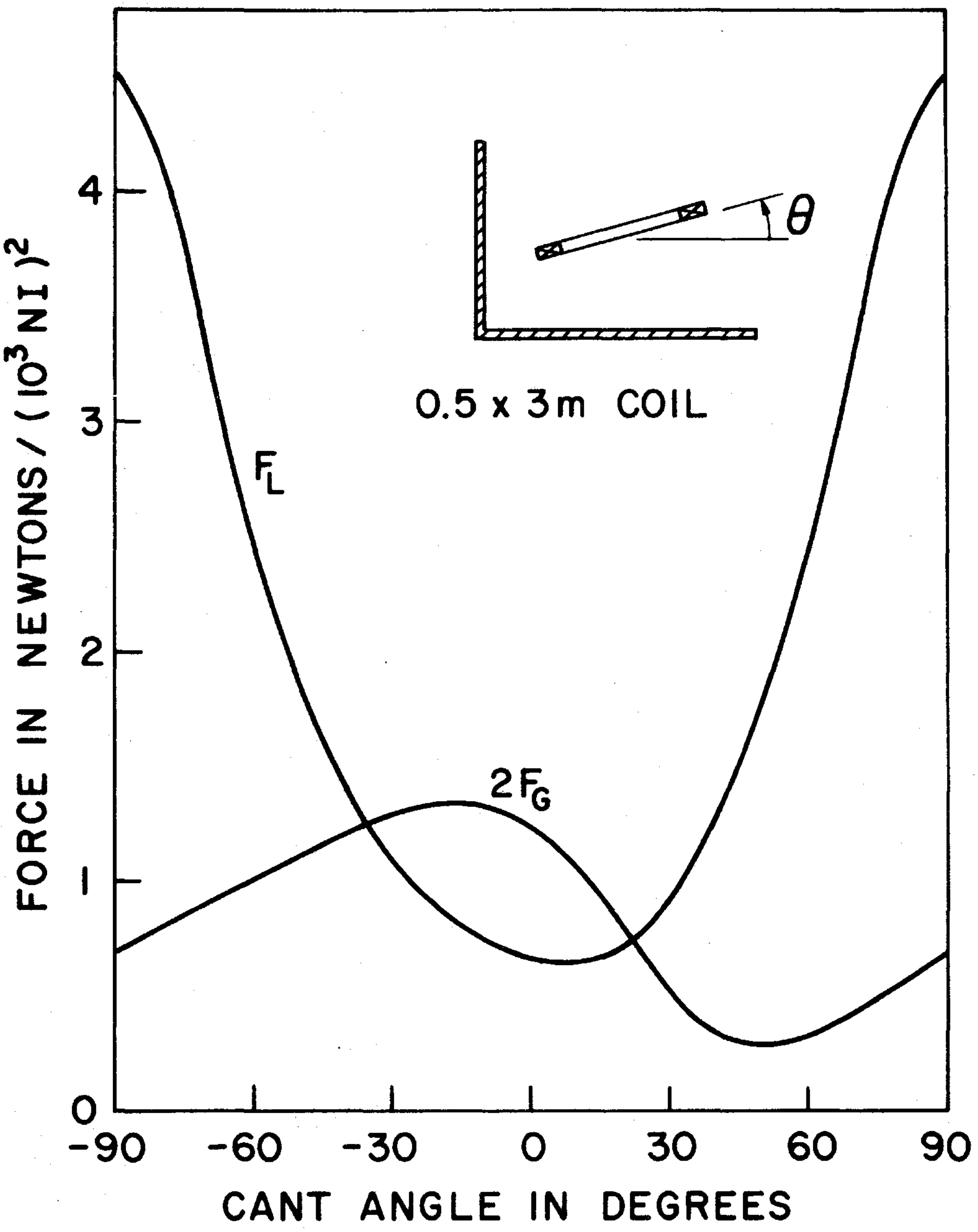

Fig. 3.14. Lift and guidance forces on a canted coil in a right-angle, corner guideway.

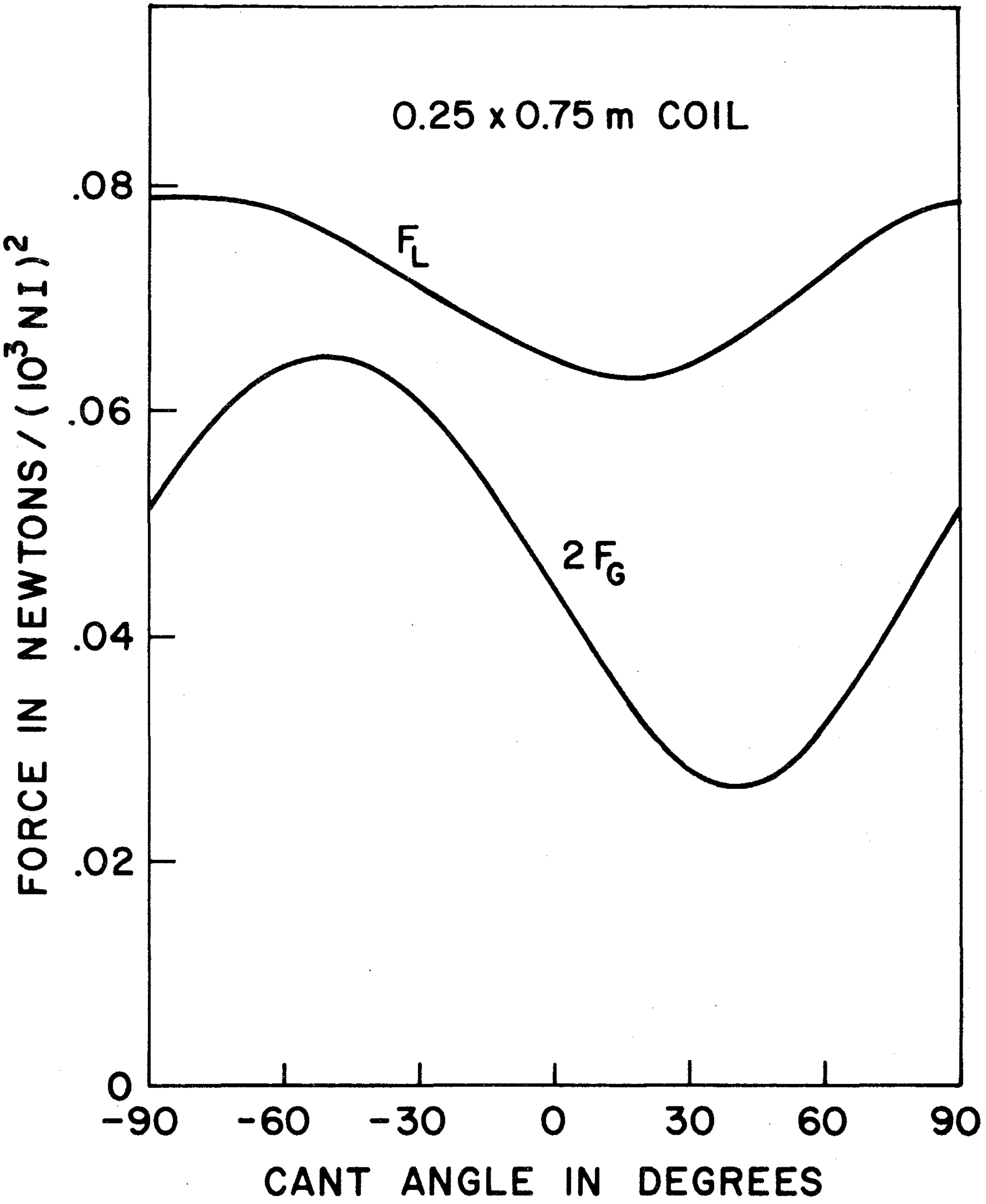

Fig. 3.15. Same as Fig. 3.14; smaller coil.

3.4 Field and Eddy Current Mapping

Detailed maps of the field and eddy current distributions in a flat, conducting guideway, as produced by a 0.5 x 3 m levitation coil, were calculated. These were made for vehicle speeds of 134 m/sec and 13.4 m/sec. These results are presented in Appendix B (Section B.2).

4. CONCLUSIONS

The present study is concerned with two types of magnetic suspensions for high-speed ground vehicles: the electromagnetic (or attractive-force) suspension and the electrodynamic (or repulsive-force) suspension. Since a rather detailed discussion of the critical problem areas relating to these suspensions has been made in an earlier study,[1] the present investigation is more limited in scope and focuses on just a few of these problem areas in depth. Specifically, work on the attractive-force suspension is devoted to developing a mathematical model which correctly predicts the penetration of magnetic flux into the ferromagnetic rail at high speed and to parameter optimization of the magnet. The goal for the repulsive-force suspension is to examine various track geometries to determine whether the aluminum in the track can be more effectively employed to produce a higher lift-to-drag ratio. Experimental studies have been carried out to guide and corroborate the analytical modeling.

4.1 Attractive-Force Suspension

In Section 2.1 of the report a mathematical model of the magnet-rail system is developed which allows the calculation of magnetic fields as well as forces on the moving magnet. The model is based on Fourier methods, but it uses a multi-layer description of the ferromagnetic track in which the permeability of each layer is determined self-consistently. The model has been used to study the effects of changes in magnet geometry, vehicle speeds, conductivity and permeability changes in the rail, and operation at different force levels. Experimental studies (Section 2.3) were conducted on small-scale magnets, using a rotating-wheel facility, to verify the predictions of the mathematical model. It is found that the basic predictions of the model agree with experiment, and this gives us confidence that it can be used to predict the behavior of full-scale systems. The model is probably the most accurate one for a magnet-track system which retains the essential simplicity of the Fourier method but, at the same time, allows for the non-linear nature of the track.

In Section 2.2 the effects of rail geometry and effects of saturation in the magnet, itself, are calculated (at zero speed) by a two-dimensional, field-relaxation technique. These results have also been compared with experiment and are found to be quite reliable.

The principal predictions of our theoretical model (which are also supported by experiment) are as follows:

i) At high speed, long magnets give superior performance to that of short magnets in regard to lift/unit length and lift-to-drag ratio. For example, at $v = 134$ m/s a one-meter long magnet will require 2 to 3 times (depending on detailed magnet geometry and the force level) as much current as at $v = 0$, but a 3-meter long magnet will require only 30% to 60% more. The lift-to-drag ratio, F_L/F_D, is approximately proportional to magnet length.

ii) Small gaps between the elemental magnets making up a "long" magnet will not degrade performance appreciably.

iii) Narrow magnets give better performance than wide magnets, presumably because they allow the magnetic flux to penetrate deeper into the track at high speed. If, however, the magnets are made too narrow, other effects such as increased coil resistance or increased core reluctance may degrade system performance. Thus, the detailed magnet geometry must be optimized as to overall system performance.

iv) The magnet pole faces should be made narrow, up to the point where the magnetic flux begins to saturate.

v) For an optimally-designed, long magnet (perhaps 30 m in length) it appears that the high-speed ($v = 134$ m/s) lift-to-drag ratio could be in the range of 200 to 300. This magnet would, however, be subject to a degradation in lift and to increased drag as a result of guideway roughness (see vi).

vi) The effect of the control system on magnet performance was not studied in the current program. It is clear, however, that the current distribution along the length of a long magnet will be affected by the control system. For example, under a severe perturbation the magnet current may be a maximum at several points along its length and zero or very small at others. Thus, it is expected that a reduction in lift and an increase in drag will result from guideway roughness and/or gust loading of the vehicle. Such a loss of lift is serious, even though sporadic or for a limited period of time. The levitation system must be able to supply full lift at all times, even under the most severe perturbation. On the other hand the increase in magnetic drag resulting from occasional severe perturbations is not too important since it is the time-averaged drag which governs system energy consumption.

vii) Magnet performance can be improved by laminating the track. Such a scheme would substantially increase track costs and is not being pursued by MBB and KM (the principal proponents of the attractive-force suspension).

4.2 Repulsive-Force Suspension

Section 3.1 of the report is devoted to a study of the slotted and ladder tracks. The slotted track is an aluminum sheet track containing an array of transverse slots spaced periodically along its length. The effect of slotting is to change the eddy current pattern in the track;

this could in principle (provided the slotting is done properly) increase the lift-to-drag ratio of the system, and such a benefit was found to occur by a group of experimenters at Stanford University.[12] A more careful analysis of their results[12] indicated, however, that the effect is marginal if it exists at all. Our experiments, performed on a larger system with low mechanical drag, show the opposite results, namely, a lower F_L/F_D for the slotted track as compared to the solid track. The slotted track also produces a somewhat smaller lift force, F_L, than does the solid track.

Measurements were also made of the lift and drag forces on a coil above a ladder track. This track has the same topology as the slotted track but the holes in this track are much larger. In all cases the lift force and F_L/F_D were found to be less for the ladder track than what was found for a solid track of the same thickness. The results are in fairly good agreement with theoretical calculations. The calculations show, however, that when the "rung spacing" of the ladder becomes large, F_L/F_D for a ladder track can be superior to that of a solid track having the same amount of aluminum per unit length; on the other hand the large rung spacing produces a substantial periodic component in the lift force.

Section 3.2 is devoted to calculations of lift and guidance in corner guideways and to inductance measurements of the guidance force in finite-height, corner guideways. It is found that F_G/F_L depends on the aspect ratio of the coil and is larger for longer coils. It is also found that finite-height guideways in which the vertical panel is only slightly larger than the suspension height of the coil give as much guidance as one where the panel is infinitely high.

Section 3.3 treats the canted coil, i.e., the situation where the plane of the coil is tilted relative to the lower guideway surface.

It is found that under certain conditions a small-angle cant ($\sim 15^{\circ}$) will improve the guidance-to-lift ratio of a coil in a corner guideway.

5. RECOMMENDATIONS

The present study has focused on the high-speed magnetic behavior of the magnet-track system in the attractive-force suspension and on alternative track configurations for the repulsive-force suspension. The results of this study have not altered the primary conclusions and recommendations of our earlier report.[1] Both types of magnetic suspension appear capable of supporting and guiding high-speed ground vehicles. The next phase of the magnetic levitation program should focus on high-speed comparison tests of these two suspensions. The rocket-sled program proposed by the Department of Transportation,[5] in which model vehicles supported by one or other of these suspensions are accelerated to speeds of 480 km/h and their dynamic behavior studied, would appear to be a direct way of accomplishing this objective.

Attractive Force Suspension: The results of the present study indicate that satisfactory high-speed performance of the magnet-track system can be obtained without requiring the ferromagnetic rail to be laminated, at least for situations where the environmental perturbations are small. On the other hand, substantial current variation along the length of the magnet, if required by the control system, will probably cause a deterioration in magnet performance. This latter effect could be studied by means of analytic simulations, but is probably best studied as part of a rocket-sled test program or of a research vehicle test program.

Repulsive-Force Suspension: On the basis of this and previous studies we recommend a solid, sheet-type track in the configuration of two right-angle corners, for the research vehicle program. This guideway is easy to fabricate, has good magnetic performance, and offers positive retension if the magnetic guidance fails. There have been so many different kinds of guideways proposed for the repulsive-force suspension (sheet track, slotted track, ladder track, discrete coil, null-flux, and sheet track with variable cross-section) that it is impossible to state categorically that one guideway is clearly superior to the others. We can, however, definitely state that the slotted track is inferior to the solid sheet track; furthermore, the advantages of other tracks over the solid sheet, if they exist at all, come about through loss in lift per unit magnet current and through more complicated fabrication requirements.

6. REFERENCES

1. J.R. Reitz, R.H. Borcherts, L.C. Davis, T.K. Hunt, and D.F. Wilkie, "Preliminary Design Studies of Magnetic Suspensions for High Speed Ground Transportation". U.S. Department of Transportation Report PB223-237* (1973).

2. L.C. Davis, J.R. Reitz, D.F. Wilkie and R.H. Borcherts, "Technical Feasibility of Magnetic Levitation as a Suspension System for High-Speed Ground Transportation Vehicles". U.S. Department of Transportation Report PB210-506* (1972).

3. H.T. Coffey, F. Chilton and L. O. Hoppie, "The Feasibility of Magnetically Levitating High Speed Ground Vehicles". U.S. Dept. of Transportation Report PB210-505* (1972)

4. R.H. Borcherts, L.C. Davis, J.R. Reitz and D.F. Wilkie, "Baseline Specifications for a Magnetically Suspended High-Speed Vehicle", proc. IEEE 61, 569 (May, 1973).

5. Request for Proposal DOT-FR-30050, "Tracked Magnetic Levitation Vehicle Technology Program", U.S. Dept. of Transportation, 30 March 1973.

6. H.T. Coffey, J.D. Colton and K.D. Mahrer, "Study of a Magnetically Levitated Vehicle". U.S. Department of Transportation Report PB222-696 (1973).

7. E. Gottzein and B. Lange, "Magnetic Suspension Control Systems for the German High Speed Train", Fifth IFAC Symposium on Automatic Control in Space, Genoa, Italy (June, 1973).

8. G. Winkle, "Status of the Transrapid Development Program", Second Intersociety Conference on Transportation, Denver (Sept. 23-27, 1973).

9. Robert Lari is the designer and present custodian of TRIM and FORGEY at Argonne National Laboratory.

10. USS, Non-Oriented Electrical Steel Sheets (United States Steel, 525 William Penn Place, Pittsburgh, Pa. 15230).

11. J.R. Powell and G.R. Danby, Amer. Soc. Mech. Engrs. Paper 66-WA/RR-5 (1966).

12. R.L. Byer, R.F. Begley and G.R. Stewart, "A Magnetically Levitated Merry-Go-Round" Stanford Univ. Report, unpublished (1972); Amer. J. Phys. 42, 111 (1974).

13. E. Ohno, M. Iwamoto, T. Yamada, "Characteristics of Superconductive Magnetic Suspension and Propulsion for High-Speed Trains", Proc. IEEE 61, 579 (May, 1973).

14. Philco-Ford Computer Program

15. F.W. Grover, Inductance Calculations, Dover (New York, 1962).

---

* Available from National Technical Information Service, Springfield, Va. 22151.

APPENDIX A. ANALYTIC EXPRESSIONS FOR THE FORCE ON THE MAGNET IN THE ELECTROMAGNETIC SYSTEM ($v = 0$)

To explore some of the features of our model of the electromagnet in the attractive system, we examine the results for zero velocity. In this instance, we can reduce the problem to a two-dimensional calculation since the magnets are long in the direction of motion. Analytical results can be obtained in many cases for two dimensions, whereas for three dimensions we must resort to the computer. At zero velocity, the track can be treated as a linear material, an additional simplification. Initially we explore the consequences of assuming a uniform magnetization (model of reference 1). Then we show how the peaking of the field near the edges of poles comes about.

To reduce the complexity of the mathematics involved without losing the accuracy of the results, we make three very realistic assumptions.

1) The length of the magnet in the x-direction (Fig. A3) is very large in comparison to c,
2) the magnet is placed at a height h above an infinitely thick and wide slab of unsaturated magnetic material,
3) $d \gg 2h$ (Fig. A3).

These assumptions result in a two dimensional and linear magnet model for the zero-velocity case ($v = 0$). (The model can be generalized to the case: $v \neq 0$, although in the latter case the actual length of the magnet is important and the results cannot be expressed in closed form.) We consider here only the case: $v = 0$.

To derive these relations, the Fourier transform method is used. The magnetized core is modeled by replacing it by a uniform surface magnetization current of J amp/m. This method of modeling is similar to the one used in reference 1.

Fig. A1 represents the magnetization currents at height h_1 from the track. The whole magnet consists of such magnetization current planes from height h to h + d as indicated in Fig. A.2.

In Fig. A1 we divide the space into two regions: region I above the plate containing the magnet and region II, the magnetic slab itself. The coordinate axes are fixed as indicated in Figs. A1 and A2.

Since the magnet is stationary we have from Maxwell's equations

$$\nabla^2 \underline{B} = 0 \tag{A1}$$

$$\nabla \cdot \underline{B} = 0 \quad . \tag{A2}$$

Let $B_y(y,z)$ and $B_z(y,z)$ represent the total flux density in the y and z directions at any point in the space (the component of flux density in the x-direction is identically zero).

In region I: $(z \geq 0)$

$$B_y(y,z) = \frac{1}{2\pi}\int_{-\infty}^{+\infty} a^c \exp(ik_z z + ik_y y)dk$$

$$+ \frac{1}{2\pi}\int_{-\infty}^{+\infty} a_1 \exp(-ik_z z + ik_y y)dk \quad . \tag{A3}$$

$$B_z(y,z) = \frac{1}{2\pi}\int_{-\infty}^{+\infty} b^c \exp(ik_z z + ik_y y)dk$$

$$+ \frac{1}{2\pi}\int_{-\infty}^{+\infty} b_1 \exp(-ik_z z + ik_y y)dk \quad . \tag{A4}$$

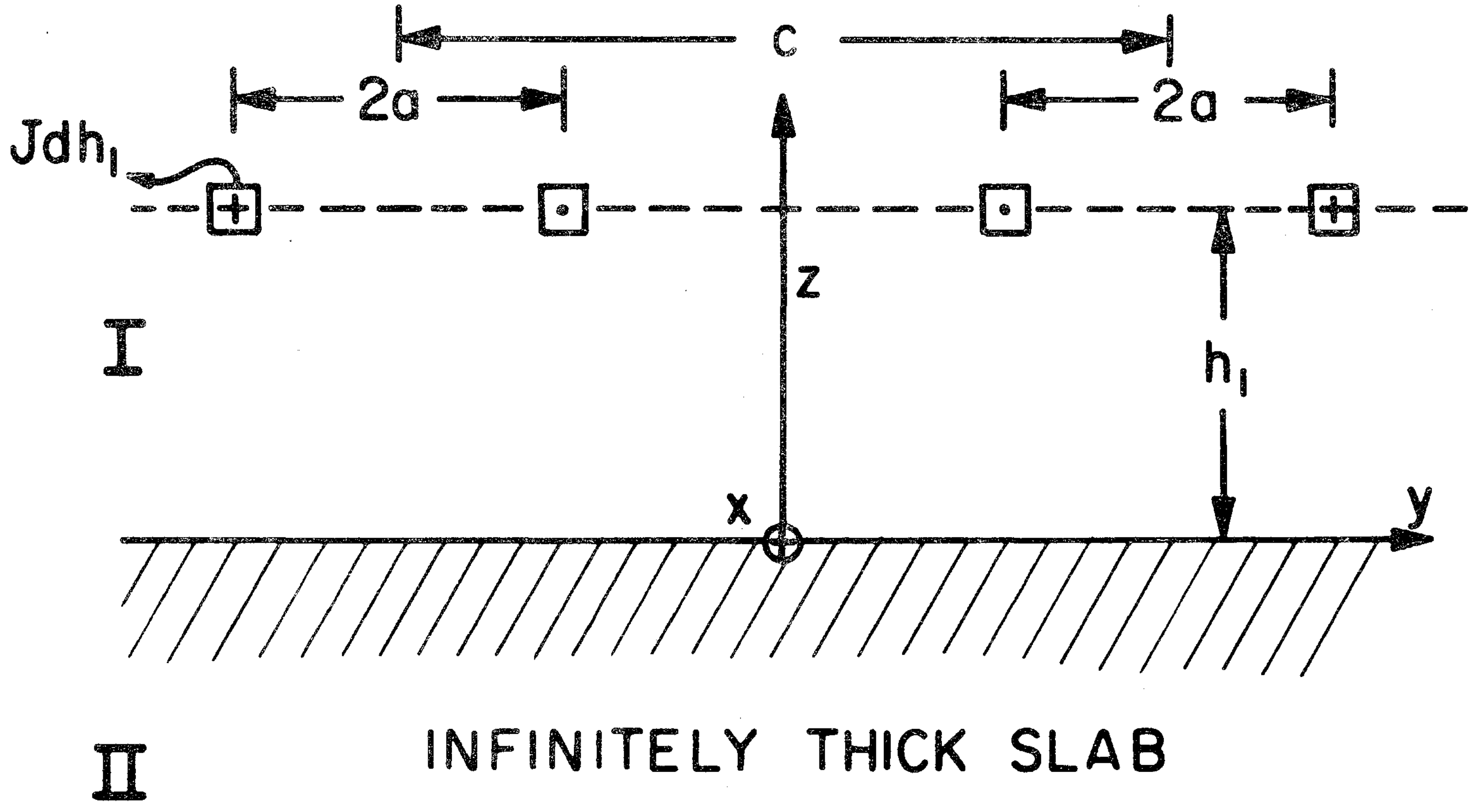

Fig. A.1. Coordinate system for single loop pair

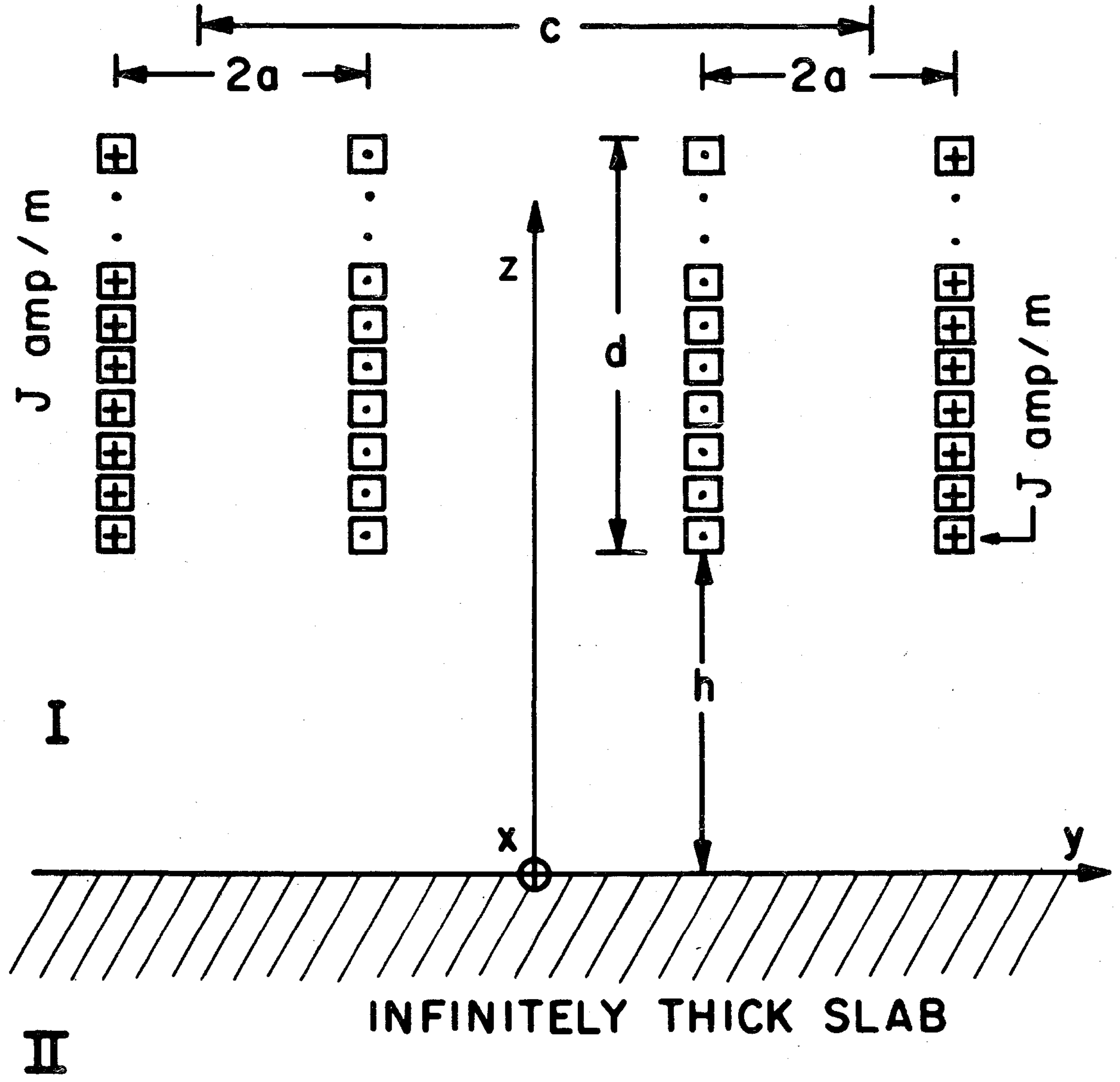

Fig. A.2. Coordinate system for model of electromagnet (uniform magnetization of poles).

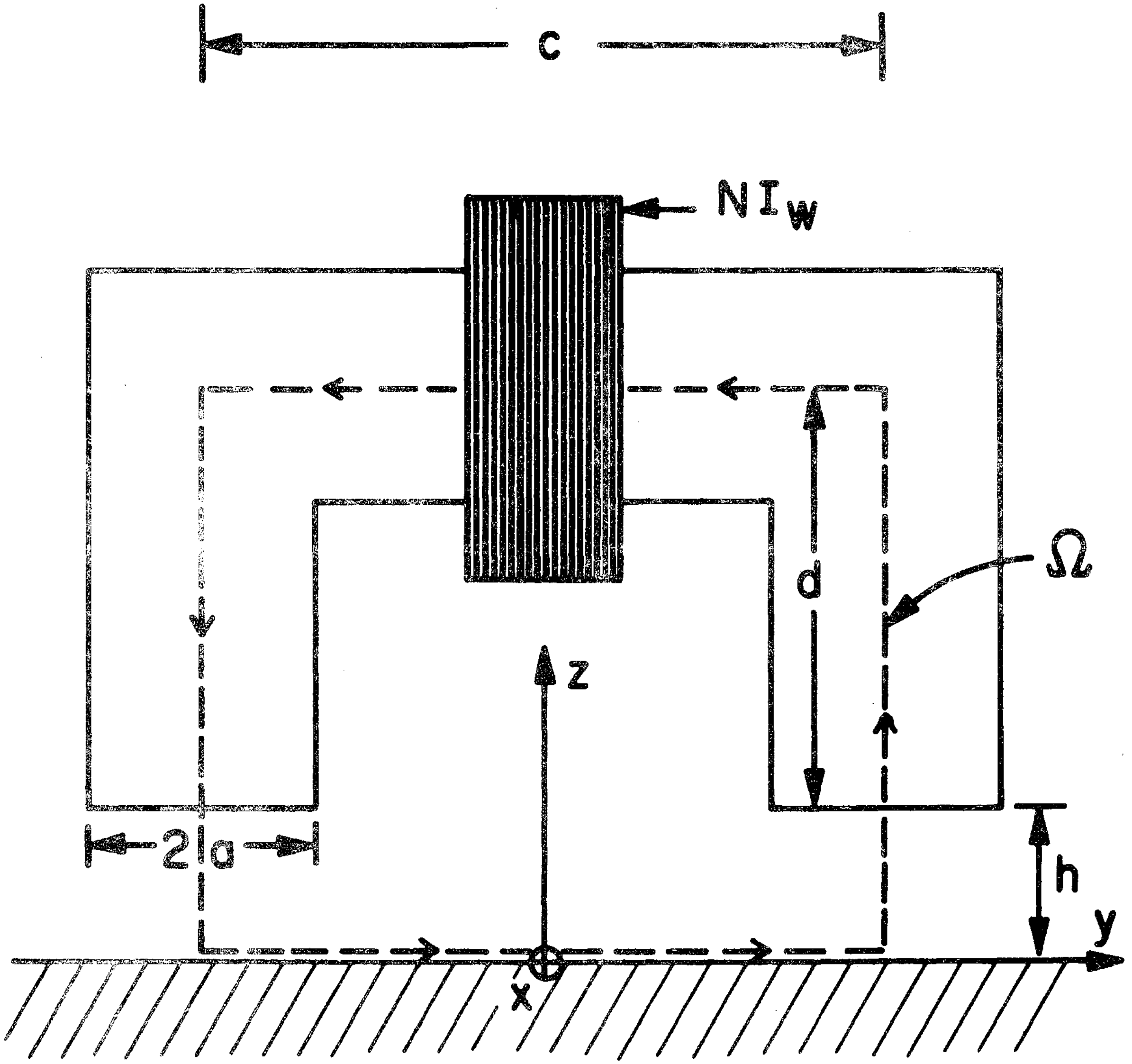

Fig. A.3. Schematic drawing of electromagnet.

The first term on the right hand side of Eqs. (A3) and (A4) corresponds to the field due to the coil, whereas, the second term is the field due to the magnetization of the magnetic slab.

In region II: $(z \le 0)$

$$B_y(y,z) = \frac{1}{2\pi} \int_{-\infty}^{+\infty} a_2 \exp(ik_z z + ik_y y) dk \qquad (A3')$$

$$B_z(y,z) = \frac{1}{2\pi} \int_{-\infty}^{+\infty} b_2 \exp(ik_z z + ik_y y) dk \quad . \qquad (A4')$$

To satisfy the condition in (A1) the k's are related by

$$k^2_y + k^2_z = 0 \quad .$$

Let

$$k_y = k \qquad (A5)$$

$$k_z = - i|k| \quad . \qquad (A6)$$

Application of condition (A2) along with (A5) and (A6) gives

$$a^c = i\, b^c \qquad (A7)$$

$$a_1 = -i\, b_1 \quad . \qquad (A8)$$

Matching the normal components of B and tangential components of H across the boundaries of regions I and II the following results are obtained.

$$b^c = -i\, a^c \qquad (A9)$$

$$a_1 = \left(\frac{1-\varkappa}{1+\varkappa}\right) a^c \qquad (A10)$$

$$a_2 = \left(\frac{2\varkappa}{1+\varkappa}\right) a^c \qquad (A11)$$

$$b_1 = i\left(\frac{1-\kappa}{1+\kappa}\right) a^c \tag{A12}$$

$$b_2 = \frac{-2i\kappa}{1+\kappa}\, a^c \tag{A13}$$

where a_2 and b_2 are the Fourier coefficients of B_y and B_z in region II, and where κ is the relative permeability of region II (the magnetic slab) with respect to region I(air).

The boundary conditions at $z = h_1$ gives

$$B_y^c(y, z=h_1) = \frac{\mu_o}{2}\, i(x,y) \tag{A14}$$

where

$$B_y^c(y, z=h_1) = \frac{1}{2\pi} \int_{-\infty}^{+\infty} a^c \exp(|k|h_1 + iky)\,dk \tag{A15}$$

and

$$i(x,y) = J\,dh_1 \left\{ \delta(y + \frac{c}{2} + a) - \delta(y + \frac{c}{2} - a) - \delta(y - \frac{c}{2} + a) + \delta(y - \frac{c}{2} - a) \right\}. \tag{A16}$$

Using the properties of transform pairs and the Dirac delta function we get

$$a_1^c = -\,2\,\mu_o (J\,dh_1)\ \sin(ka)\ \sin(\frac{kc}{2})\ \exp(-|k|h_1) \quad . \tag{A17}$$

Integrating with respect to h_1 to find this value for the entire magnetized core we get

$$a^c = \lim_{d \gg 2h} \int_h^{h+d} a_1^c$$

$$a^c = -2\,\mu_o J\ \frac{\sin(ka)\ \sin(kc/2)\ \exp(-|k|h)}{|k|} \quad . \tag{A18}$$

From this value of a^c all the coefficients given in (A9) through (A13) and components of flux density in various regions could be evaluated.

In region I:

$$B_y(y,z) = W_1(y,z) - \frac{\varkappa-1}{\varkappa+1} W_1(y,-z) \qquad \text{(A19)}$$

$$B_z(y,z) = W_2(y,z) + \frac{\varkappa-1}{\varkappa+1} W_2(y,-z) \qquad \text{(A20)}$$

where

$$W_1(y,z) = \frac{1}{2\pi} \int_{-\infty}^{+\infty} a^c \exp(|k|z + i\,ky)dk$$

$$W_2(y,z) = \frac{1}{2\pi} \int_{-\infty}^{+\infty} b^c \exp(|k|z + i\,ky)dk \quad .$$

These integrals are evaluated and are

$$W_1(y,z) = \frac{\mu_o J}{4\pi} \ln \frac{[(h-z)^2+(\frac{c}{2}-a-y)^2][(h-z)^2+(\frac{c}{2}-a+y)^2]}{[(h-z)^2+(\frac{c}{2}+a+y)^2][(h-z)^2+(\frac{c}{2}+a-y)^2]} \qquad \text{(A21)}$$

$$W_2(y,z) = \frac{\mu_o J}{2\pi} \tan^{-1} \frac{\frac{c}{2}+a+y}{h-z} + \tan^{-1} \frac{\frac{c}{2}-a-y}{h-z} - \tan^{-1} \frac{\frac{c}{2}-a+y}{h-z}$$

$$-\tan^{-1} \left\{ \frac{\frac{c}{2}+a-y}{h-z} \right. \quad . \qquad \text{(A22)}$$

To find the total force on the magnet, we first evaluate the lift force on a current carrying plane at a height h_n, with current distribution as indicated in (A16) due to the field induced in the magnetic slab by the current plane at a height h_m, which is given by

$$f_{nm} = \int_{-b}^{+b} dx \int_{-\infty}^{+\infty} i_n(y)\, B^m_{ny}(y, z=h_n)\, dy \qquad \text{(A23)}$$

where

$$B^m_{ny}(y, z=h_n) = \frac{1}{2\pi} \int_{-\infty}^{+\infty} a_1 \exp(-|k|h_n + i\,ky)dk \quad .$$

The equation (A23) could also be written as

$$f_{nm} = \frac{2b}{2\pi} \int_{-\infty}^{+\infty} i_n^*(k)\, B_{ny}^m(k)\, dk \tag{A24}$$

where $i_n(k)$ is the Fourier transform of (A16) and

$$B_{ny}^m(k) = a_1 \exp(-|k|h_n)$$

Substituting these values into (A24) and integrating with respect to h_n and h_m for the total force we get

$$f = \frac{16\mu_o J^2 b}{\pi} \left(\frac{1-\kappa}{1+\kappa}\right) \int_0^{\infty} \sin^2 (ka)\cdot\sin^2 \left(\frac{kc}{2}\right) \iint_h^{h+d} \exp\left[-k(h_m+h_n)\right] dh_m dh_n dk\ . \tag{A25}$$

Again, making use of the assumption that d >> 2h and carrying out the integration

$$f = \frac{2\mu_o J^2 bh}{\pi} \left(\frac{1-\kappa}{1+\kappa}\right) \left\{ \ln\left[\frac{\left[1+\left(\frac{c-2a}{2h}\right)^2\right]\left[1+\left(\frac{c+2a}{2h}\right)^2\right]}{\left[1+\left(\frac{a}{h}\right)^2\right]^2 \left[1+\left(\frac{c}{2h}\right)^2\right]^2}\right] + \left[\frac{4a}{h}\tan^{-1}\left(\frac{a}{h}\right) + \frac{2c}{h}\tan^{-1}\left(\frac{c}{2h}\right) - \frac{(c+2a)}{h}\tan^{-1}\left(\frac{c+2a}{2h}\right) - \left(\frac{c-2a}{h}\right)\tan^{-1}\left(\frac{c-2a}{2h}\right)\right]\right\}\ . \tag{A26}$$

Equations (A21), (A22) and (A26) are given as a function of magnetization current. But as described in Sec. 2.1.3 of this report it is possible to get a relation between the true ampere turns (NI_w) of the magnetizing coil and the magnetization current J.

Integrating around the contour shown in Fig. A3, we have

$$\oint_{\Omega} H \cdot d\ell = NI_w \tag{A27}$$

Neglecting the MMF drop in the magnetized core in comparison to the MMF of the rest of the magnetic circuit

$$NI_w = \frac{1}{\mu_o} \int_{-c/2}^{o} B_y\ (y, z = 0)\ dy + \frac{1}{\mu_o} \int_{o}^{c/2} B_y\ (y, z = 0)\ dy$$

$$+ \frac{1}{\mu_o} \int_{o}^{h} B_z\ (y = \frac{c}{2}, z)\ dz + \frac{1}{\mu_o} \int_{-h}^{o} B_z\ (y = \frac{-c}{2}, z)\ dz\ . \tag{A28}$$

Because of the symmetry of the problem (A28) reduces to

$$NI_w = \frac{2}{\mu_o} \int_{o}^{c/2} B_y\ (y, z = 0)\ dy + \frac{2}{\mu_o} \int_{o}^{h} B_z\ (y = \frac{c}{2}, z)\ dz\ . \tag{A29}$$

From the equations (A19) and (A20)

$$B_y\ (y, z = 0) = W_1(y,0) - \left(\frac{\varkappa-1}{\varkappa+1}\right) W_1(y,0)$$

$$B_y(y, z = 0) = \frac{1}{2\pi} \int_{-\infty}^{+\infty} \frac{2}{(\varkappa+1)}\ a^c \exp\ (iky)\ dk$$

$$\int_{o}^{c/2} B_y(y,0)\ dy = \int_{o}^{c/2} \frac{1}{2\pi} \left(\frac{2}{\varkappa+1}\right) \int_{-\infty}^{+\infty} a^c \exp(iky)\ dk\ dy$$

$$\int_{o}^{c/2} B_y(y,0)\ dy = \frac{1}{\pi(\varkappa+1)} \int_{-\infty}^{+\infty} dk \int_{o}^{c/2} a^c \exp(iky)\ dy\ . \tag{A30}$$

Similarly

$$\int_{o}^{h} B_z(y = \frac{c}{2}, z) dz = \frac{1}{2\pi} \int_{-\infty}^{+\infty} dk \int_{o}^{h} b^c \Big[\exp\ (|k|z) +$$

$$\left(\frac{\varkappa-1}{\varkappa+1}\right) \exp(-|k|z) \Big] \exp\left(\frac{ikc}{2}\right)\ dy\ . \tag{A31}$$

In Eqns. (A30) and (A31) the order of integration is changed because of obvious reasons.

Evaluating (A30) and (A31) and adding we get

$$NI_W = \frac{J}{\pi} \left\{ c\ell n \left(\frac{c+a}{c-a}\right) + a\ell n \left(\frac{c^2-a^2}{a^2}\right) - \left(\frac{\varkappa-1}{\varkappa+1}\right) \left[\frac{c}{2} \ell n \left[\frac{4h^2 + (c+a)^2}{4h^2 + (c-a)^2}\right] \right.\right.$$

$$+ \frac{a}{2} \ell n \left[\frac{(4h^2 + (c+a)^2)\ (4h^2+(c-a^2))}{(4h^2 + a^2)^2}\right]$$

$$\left.\left. + 2h \left[\tan^{-1} \left(\frac{c+a}{2h}\right) - \tan^{-1} \left(\frac{c-a}{2h}\right) - 2 \tan^{-1} \left(\frac{a}{2h}\right)\right] \right\} . \quad (A32)$$

Some sample results are shown in Fig. (A4) through (A9). In our numerical studies we have used the geometry of the magnet which is being used for our experimental studies.

In Fig. (A4) the calculated z-component of flux density is plotted at $z = h^-$ for three different heights for a coil with current of 10 amperes. Figure (A4) shows that for this model the flux distribution is uniform across the pole face for larger gaps, where as it peaks up at the center of the pole face for smaller gaps. In both cases the flux outside the pole face decays sharply.

In Fig. (A5) the z-component of flux density (at the center of the magnet pole face) is plotted for three different heights as a function of coil current. The points marked correspond to the experimental data.

The field has also been measured across the pole face (Fig. 2.5). It was found to be peaked at the edges of the pole face and not peaked at the center as in our model (Fig. (A4)). The field data shown in Fig. (A5) was taken at the center of the pole face and is substantially

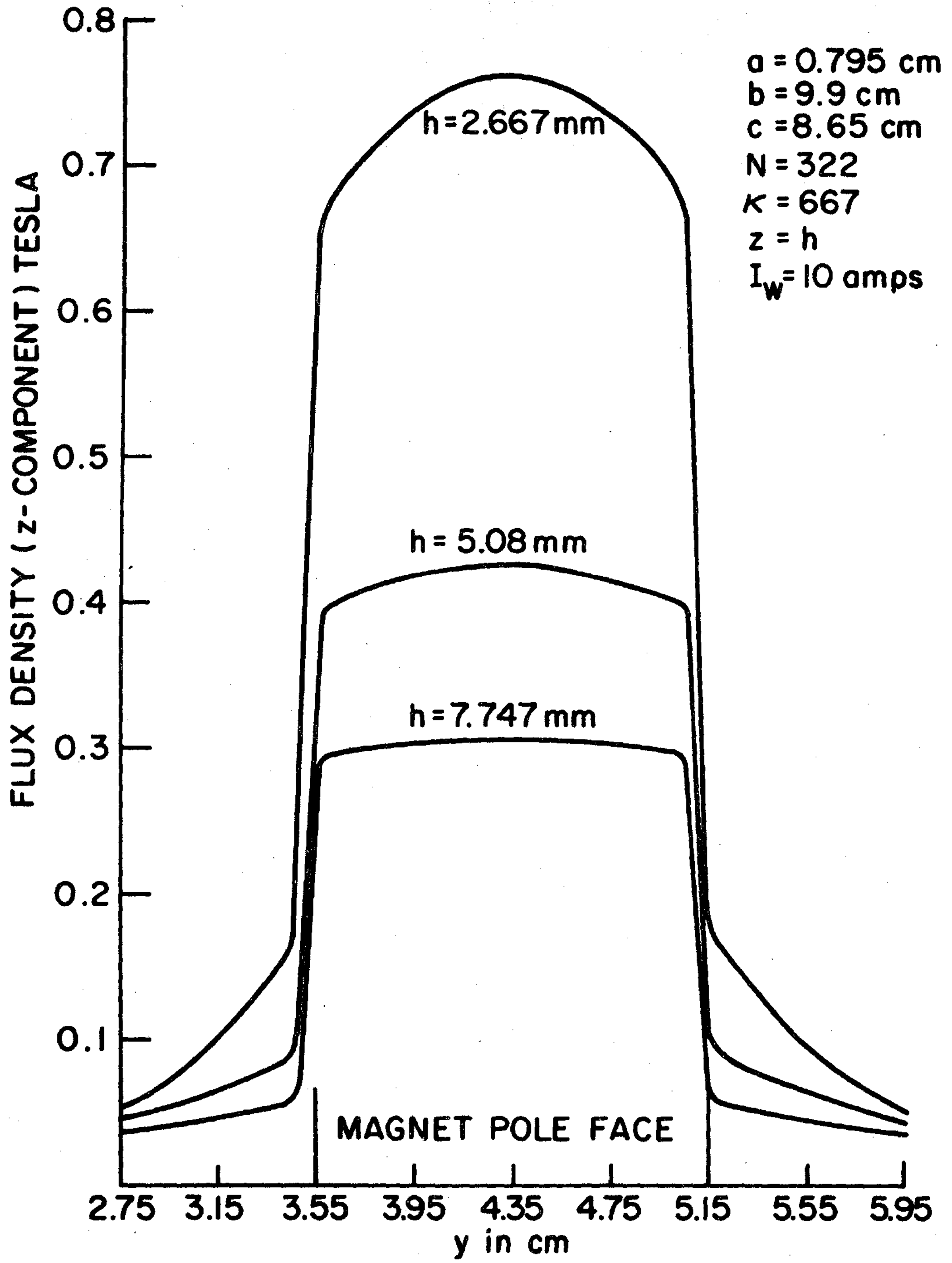

Fig. A.4. Magnetic field under pole face (uniform magnetization of poles).

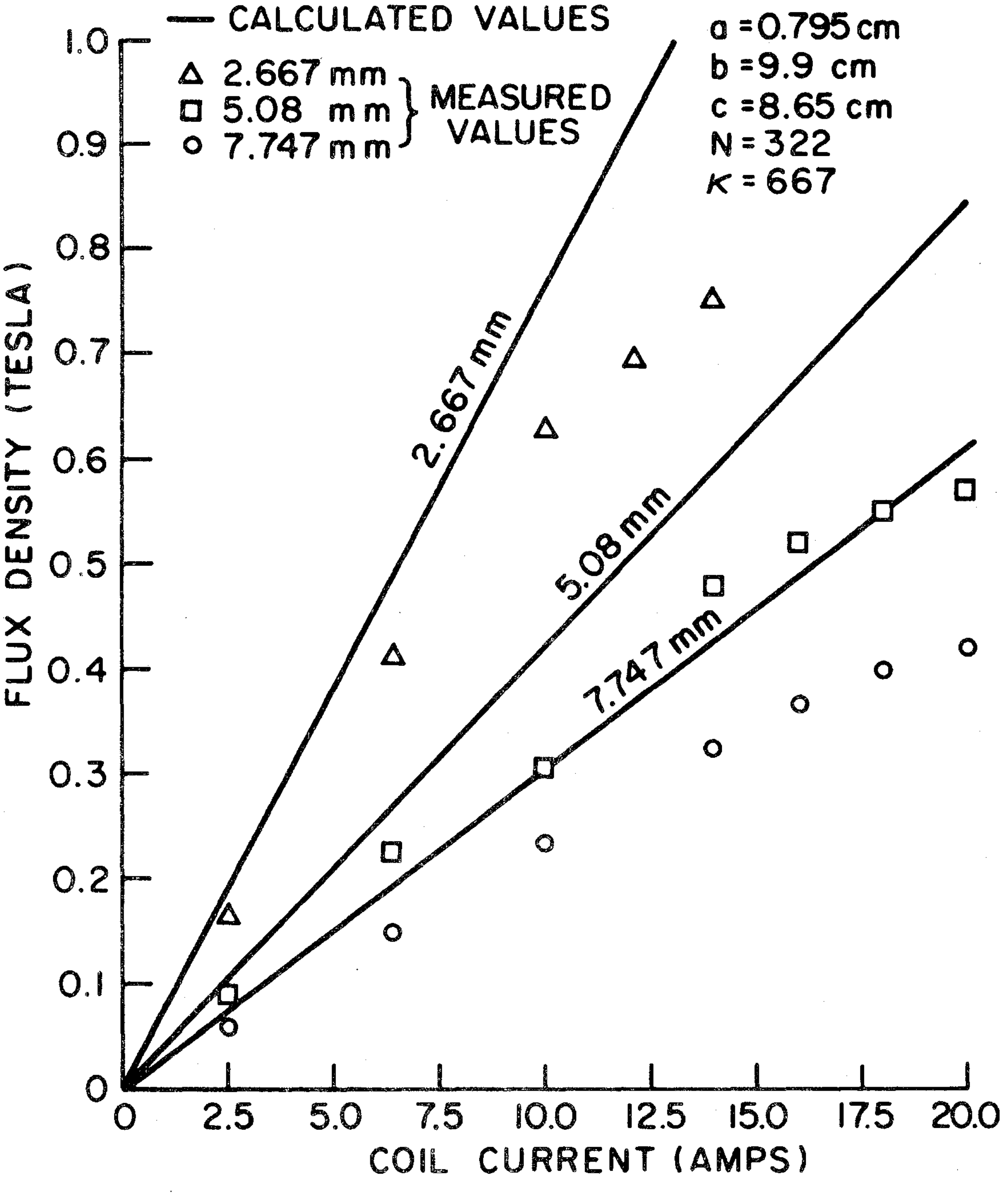

Fig. A.5. Flux density vs. current, experimental and calculated (uniform magnetization of poles) lower than at the edges. This is one reason why our calculated values are larger than those measured.

Figure (A6) and Fig. (A7) show the variation of the lift force as a function of current and $(\text{height})^2$ for this model.

In Fig. (A7) the dashed lines represent the force on the magnet calculated by very simple theoretical assumptions:

$$F = \frac{\mu_o (NI)^2 A}{4h^2} ,$$

(see Sec. 3.2 of reference 1 and neglect the reluctance of the core and track). Our model gives a smaller force when compared to the simple theory.

In Fig. (A8) and Fig. (A9) we have plotted the measured force and the calculated force as a function of current and flux density squared. The calculated values of the force are smaller than the measured values. Since the model does not take into account core saturation the results should be compared at the lower current values; here there is substantial disagreement between the model and experiment. It is believed that this discrepancy is due, for the most part, to a shortcoming of the model, namely, that of uniform magnetization of the core.

A1. Effect of Non-Uniform Magnetization

In deriving Eqs. (A21), (A22), (A26) and (A32) we replaced the magnetized core by surface magnetization current as shown in Fig. A2.

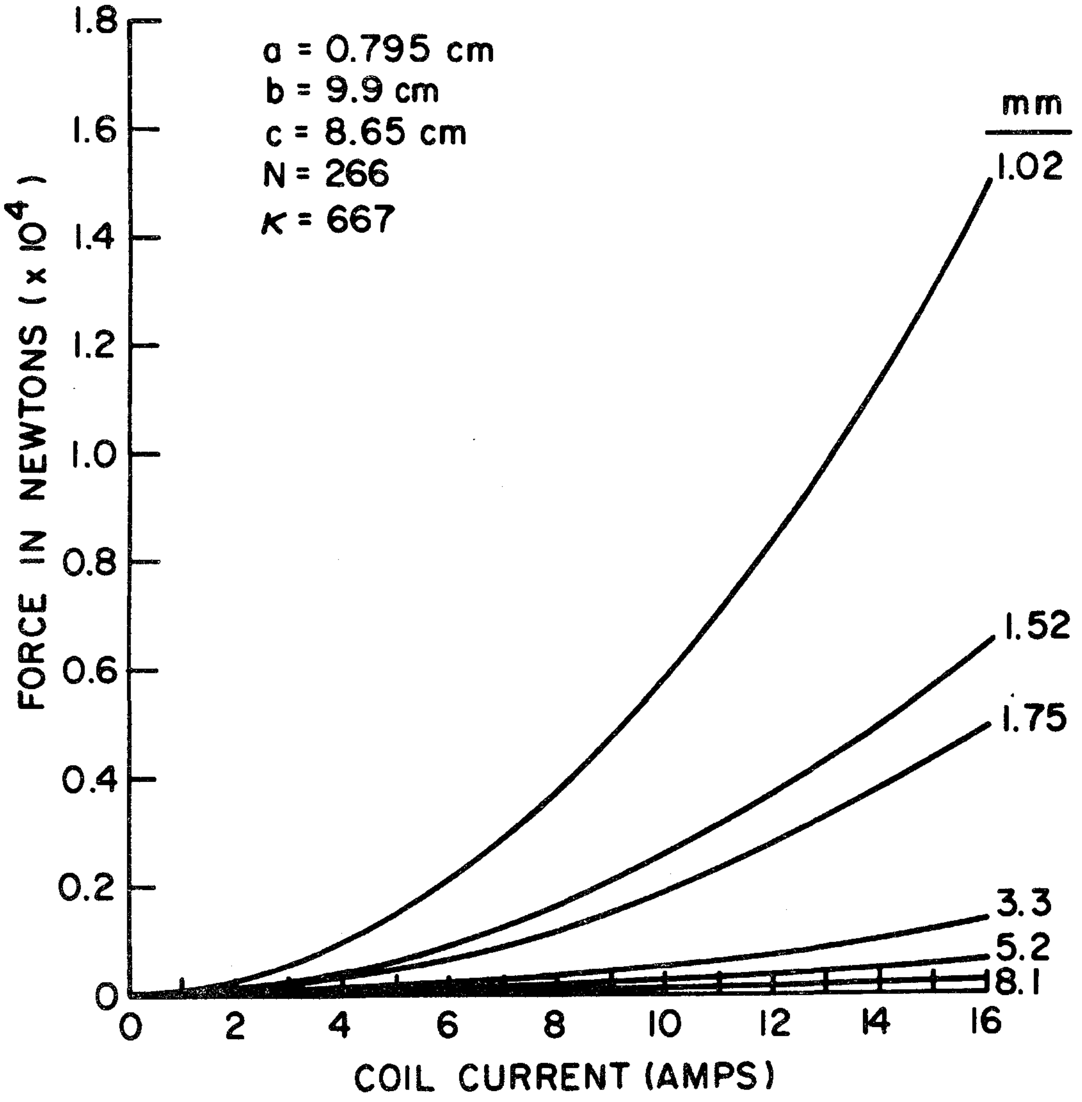

Figure A.6. Lift force vs. current for various gaps (uniform magnetization of poles).

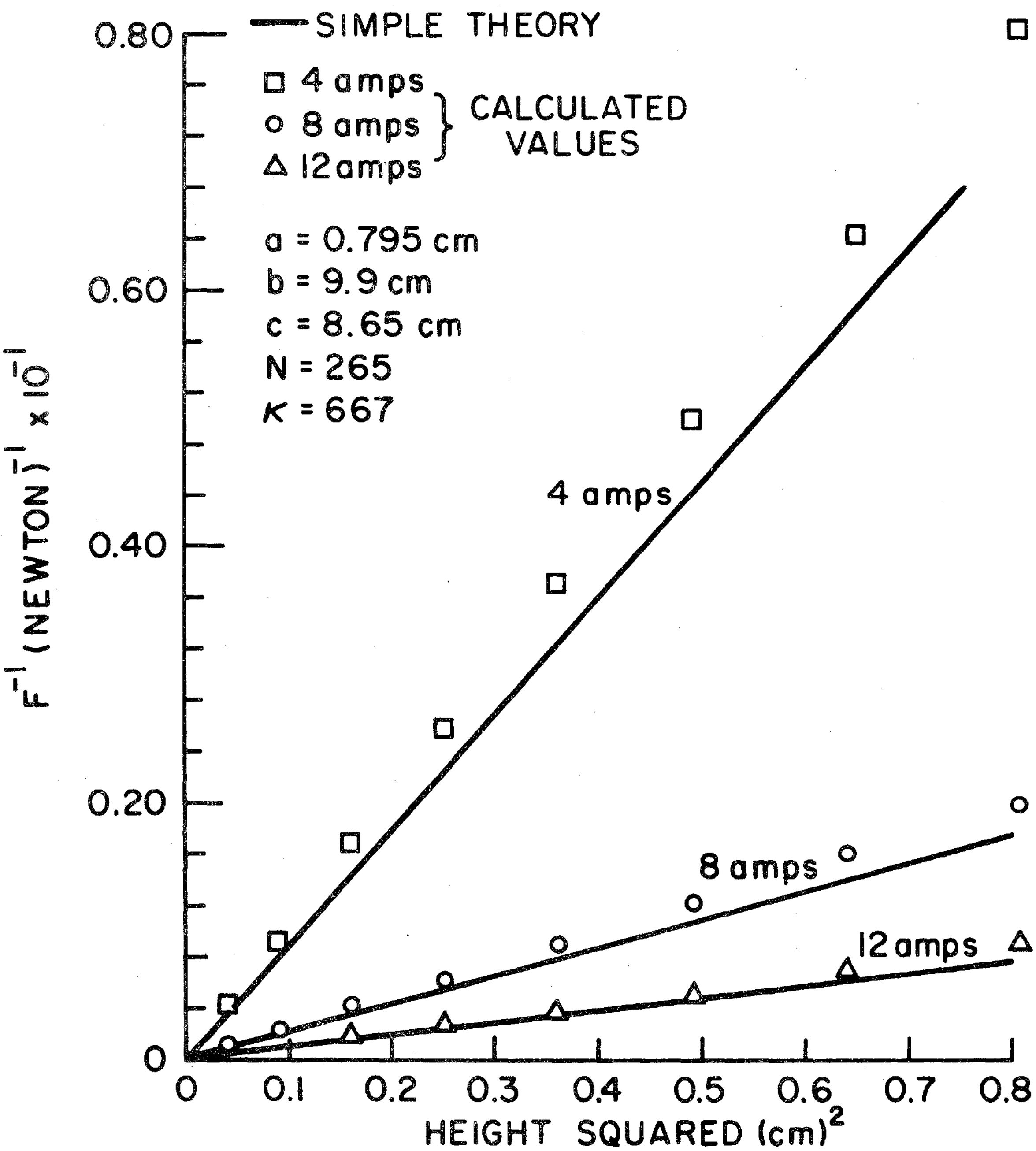

Fig. A.7. Reciprocal of lift force vs. height squared, experimental and simple theory.

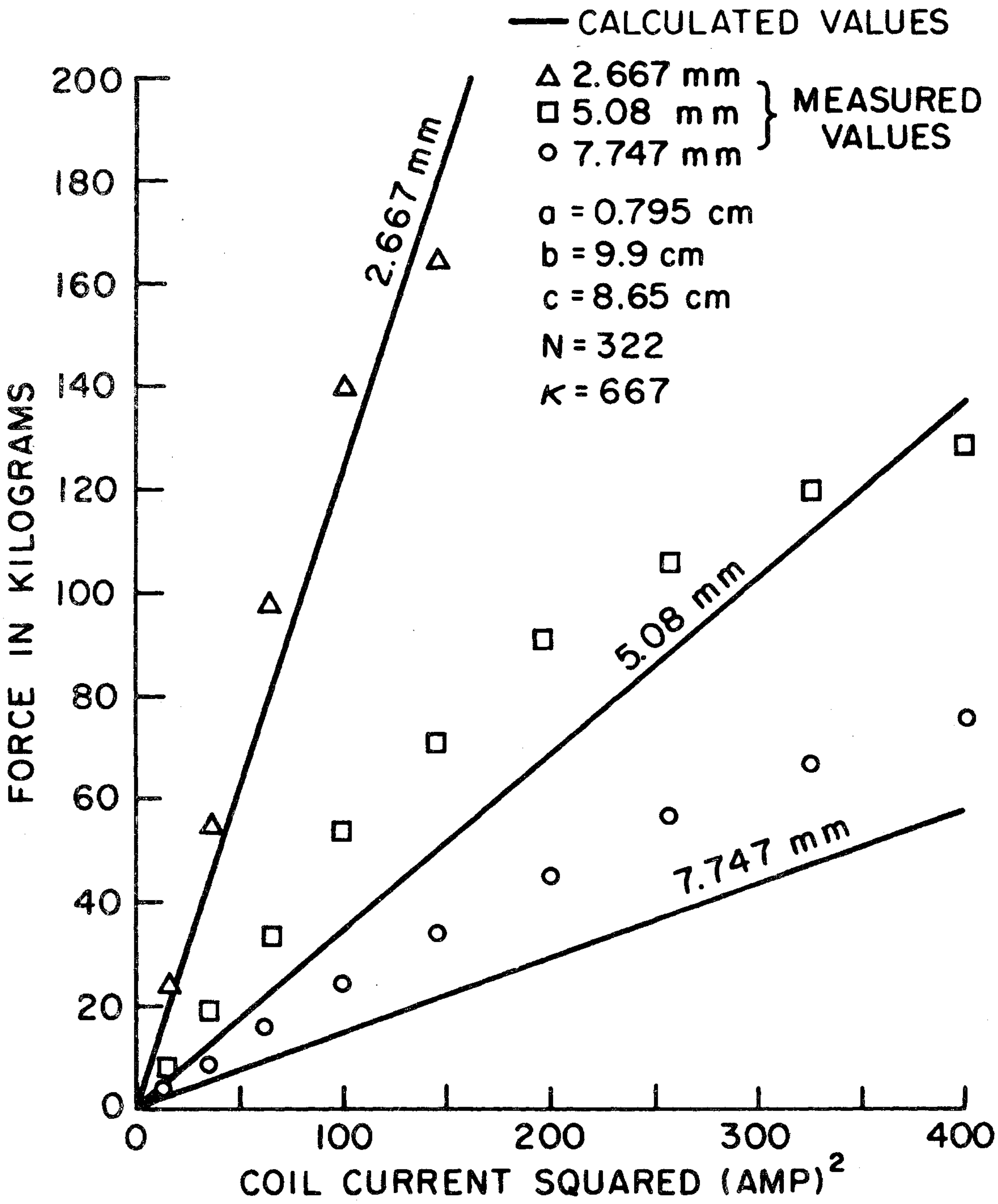

Fig. A.8. Lift force vs. current squared, experimental and calculated (uniform magnetization of poles).

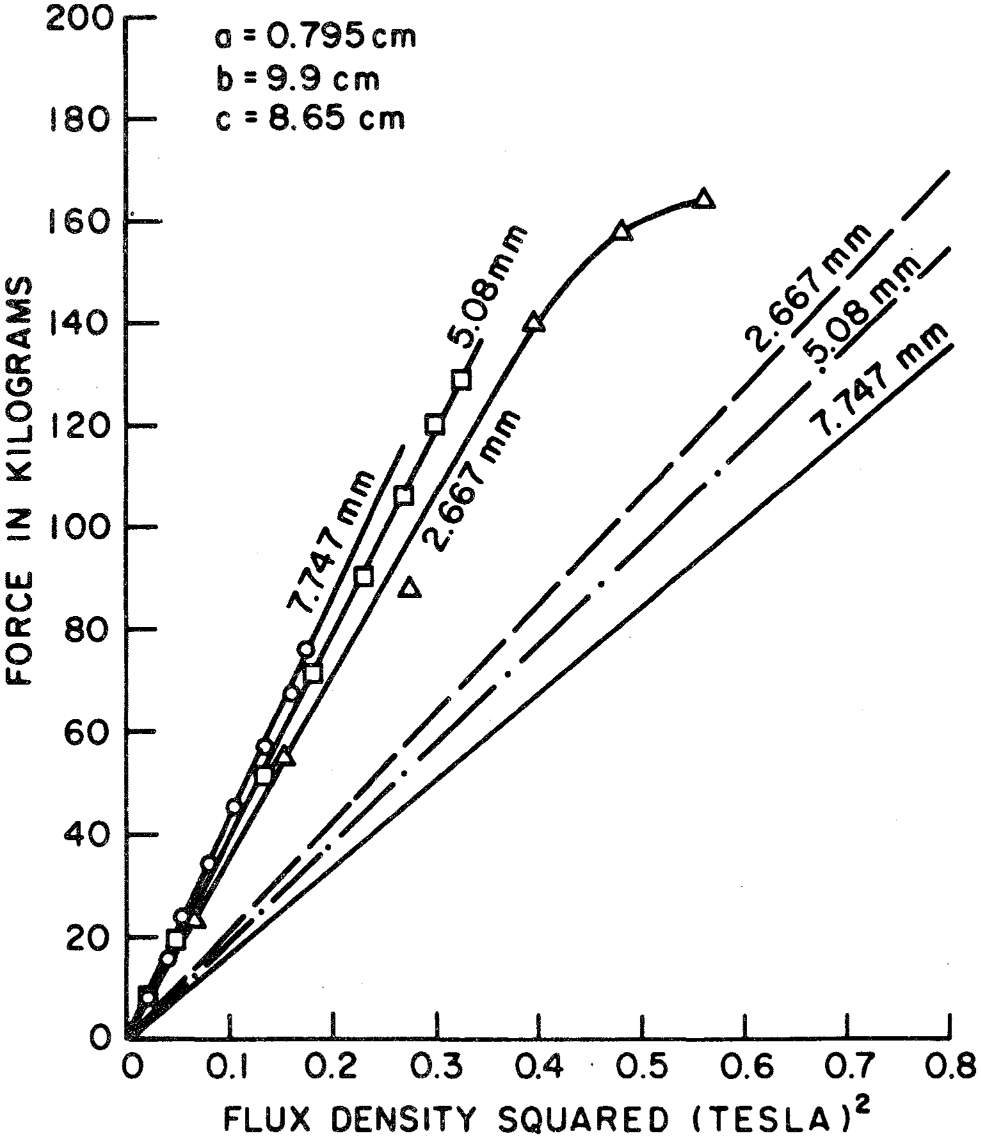

Fig. A.9. Lift force vs. flux density squared, experimental and calculated (uniform magnetization of poles).

Equation (A32) is the result of integrating (A27) along a specific contour shown in Fig. A3 whereas Eq. (A27) is valid for any arbitrary contour which encloses all the ampere turns of the coil. These assumptions give results as shown in Fig. A4, which indicates that the flux density peaks up at the center of the pole face. This contradicts the results obtained experimentally which shows the peaks at the edges of the magnet. In our derivation we assumed the integral along the specific contour is representative of the integral along any other contour which is not a correct assumption since the integration of Eq. (A27) along a smaller contour must result in higher flux density than flux density obtained by integrating (A27) along a bigger contour. Therefore, to circumvent these effects and to improve the accuracy of the expressions obtained, the magnetization current is assumed to be an arbitrary function of y .

Let $J(y)$ be the value of this current at any point $y(h < z < h+d)$ and $J(k)$ be its Fourier transform given by

$$J(k) = \int_{-\infty}^{+\infty} J(y) \exp(-iky)\, dy \quad . \qquad (A33)$$

With this assumption the relation given in Eq. (A18) is given by

$$a^{c} = -\frac{\mu_o}{2} \frac{J(k)}{|k|} \exp(-|k|h) \quad . \qquad (A34)$$

Equations (A21) and (A22) cannot be evaluated in closed form but are given by

$$W_1(y,z) = \lim_{\epsilon \to o} \frac{-\mu_o}{2\pi} \operatorname{Re}\left[\int_{\epsilon}^{\infty} \frac{J(k)}{k} \exp\{-k(h-z-iy)\} dk \right] \qquad (A35)$$

$$W_2(y,z) = \lim_{\epsilon \to 0} \frac{-\mu_0}{2\pi} I_m \left[\int_{\epsilon}^{\infty} \frac{J(k)}{k} \exp\{-k(h-z-iy)\}dk \right] . \qquad (A36)$$

The contour of integration in (A27) is assumed to satisfy the constraint that it enter the pole face at z = h; therefore, as described: before

$$NI_w = \frac{2}{\mu_0} \left[\int_0^y B_y(y,z)dy + \int_z^h B_z(y,z)dz \right] . \qquad (A37)$$

The above integrals are evaluated and the ampere turns of the coil are given by (setting $\Gamma = (\varkappa - 1)/(\varkappa + 1)$)

$$NI_w = \frac{1}{2\pi} \int_{-\infty}^{+\infty} \frac{J(k)}{k^2} \Big[\exp\{-|k|(h-z)\} - \exp\{iky\}$$

$$+ \Gamma \exp\{-|k|2h + iky\} - \Gamma \exp\{-|k|(h+z)\} \Big] dk \qquad (A38)$$

where $\frac{c}{2} - a \leq |y| \leq \frac{c}{2} + a \quad , \quad 0 \leq z \leq h$.

The total force on the magnet is given by Eq. (A24) where

$$i_n^*(k) = \frac{2}{\mu_0} a_n^c \exp(|k| h_n) \qquad (A39)$$

$$B_{ny}^m(k) = a_{1m} \exp(-|k| h_n) . \qquad (A40)$$

Therefore

$$f_{nm} = \frac{b}{\pi} \int_{-\infty}^{+\infty} \frac{2}{\mu_0} \Gamma a_n^c a_m^c dk \qquad (A41)$$

where

$$a_n^c = \frac{\mu_0}{2} J(k) \exp(-|k| h_n) dh_n \qquad (A42)$$

$$a_m^c = \frac{\mu_0}{2} J(k) \exp(-|k| h_m) dh_m . \qquad (A43)$$

Substituting these values in (A41) we get

$$f_{nm} = \frac{\mu_o}{2\pi} \, b\Gamma \int_{-\infty}^{+\infty} [J(k)]^2 \, \exp\{-|k|(h_n + h_m)\} \, dk dh_n dh_m \tag{A44}$$

Integrating with respect to h_n and h_m and assuming $d \gg h$ we get

$$f = \frac{\mu_o}{2} \, b\Gamma \int_{-\infty}^{+\infty} \frac{[J(k)]^2}{|k|^2} \, \exp(-2|k|h) \, dk \tag{A45}$$

At this point Eq. (A38) can be evaluated by either of two different methods. In the first method we assume a certain functional form for the magnetization current J(y), and using (A38) and (A45) the parameters of the chosen functional form can be evaluated to meet the desired results or experimental data. In the second approach we use Eq. (A38) as an integral constraint to evaluate J(k). Here we adopt the second method. To solve Eq. (A38) we discretize J(y) as shown in Fig. A10. With this type of current distribution Eqs. (A34)-(A36), (A38) and (A45) are given by,

$$a^c = -2\mu_o \frac{\exp(-|k|h)}{|k|} \sum_{n=-N}^{+N} J_n \sin k(c + 2na') \sin(ka') \tag{A46}$$

$$W_1(y,z) = \frac{\mu_o}{4\pi} \sum_{n=-N}^{+N} J_n \, \ell n \left[\frac{[(h-z)^2+(c+(2n-1)a'+y)^2}{[(h-z)^2+(c+(2n+1)a'+y)^2} \right.$$

$$\left. \times \frac{[(h-z)^2+)c+(2n-1)a'-y)^2]}{[(h-z)^2+(c+(2n+1)a'-y)^2]} \right] \tag{A47}$$

$$W_2(y,z) = \frac{\mu_o}{2\pi} \sum_{n=-N}^{+N} J_n \left[\tan^{-1}\left(\frac{c+(2n+1)a'+y}{h-z} \right) + \tan^{-1}\left(\frac{c+(2n-1)a'-y}{h-z} \right) \right.$$

$$\left. - \tan^{-1}\left(\frac{c+(2n+1)a'-y}{h-z} \right) - \tan^{-1}\left(\frac{c+(2n-1)a'+y}{h-z} \right) \right] \tag{A48}$$

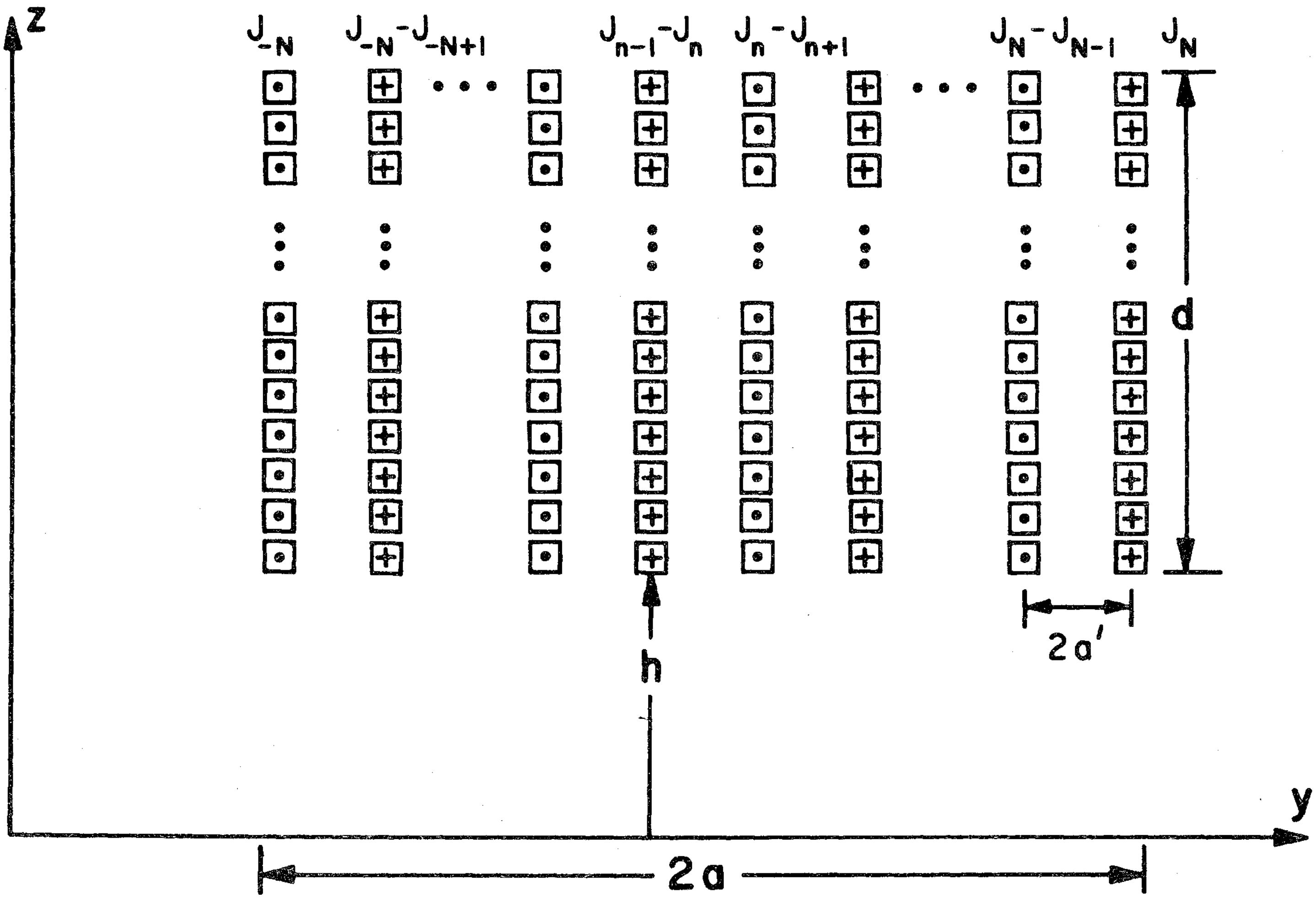

Fig. A.10. Coordinate system for discretized version of pole magnetization (non-uniform magnetization).

$$NI_w = \frac{2}{\mu_o}\left[Q(y,h) - \Gamma Q(y,-h)\right] \tag{A49}$$

where

$$Q(y,z) = \frac{\mu_o}{2\pi}\sum_{n=-N}^{+N} J_n\left[u\left\{\tan^{-1}\left(\frac{q}{u}\right) + \tan^{-1}\left(\frac{r}{u}\right) - \tan^{-1}\left(\frac{p}{u}\right) - \tan^{-1}\left(\frac{s}{u}\right)\right\}\right.$$

$$+ \left(\frac{c}{2} + na'\right)\ell n\left\{\frac{(u^2+q^2)(u^2+r^2)}{(u^2+p^2)(u^2+s^2)}\right\} + \frac{y}{2}\ \ell n\left\{\frac{(u^2+r^2)(u^2+s^2)}{(u^2+q^2)(u^2+p^2)}\right\}$$

$$\left. + \frac{a'}{2}\ell n\left\{\frac{(u^2+q^2)(u^2+s^2)}{(u^2+r^2)(u^2+p^2)}\right\}\right] \tag{A50}$$

where

$$u = h-z \tag{A51}$$

$$p = c + (2n+1)a' + y \tag{A52}$$

$$q = c + (2n+1)a' - y \tag{A53}$$

$$r = c + (2n-1)a' + y \tag{A54}$$

$$s = c + (2n-1)a' - y \quad . \tag{A55}$$

$$f = 2\mu_o\ \Gamma \sum_{n=-N}^{+N}\ \sum_{m=-N}^{+N} J_n J_m \cdot T \tag{A56}$$

where

$$T = \frac{h}{2}\left[\ell n\left[\frac{[h^2+((n-m)a')^2]^2\,[h^2+(c+(n+m-1)a')^2]}{[h^2+(c+(n+m)a')^2]^2\,[h^2+((n-m-1)a')^2]}\right.\right.$$

$$\left.\left.\times\frac{[h^2+(c+(n+m+1)a')^2]}{[h^2+((n-m+1)a')^2]}\right]\right] - \left[\frac{4(n-m)a'}{h}\quad\tan^{-1}\left(\frac{(n-m)a'}{h}\right)\right.$$

$$- \frac{4(c+(n+m)a')}{h}\tan^{-1}\left(\frac{c+(n+m)a'}{h}\right)$$

$$
\begin{aligned}
&+ \left\{ \frac{2(c+(n+m-1)a')}{h} \right\} \tan^{-1}\left(\frac{c+(n+m-1)a'}{h} \right) \\
&+ \left\{ \frac{2(c+(n+m+1)a')}{h} \right\} \tan^{-1}\left(\frac{c+(n+m+1)a'}{h} \right) \\
&- \left\{ \frac{2(n-m-1)a'}{h} \right\} \tan^{-1}\left(\frac{(n-m-1)a'}{h} \right) \\
&- \left\{ \frac{2(n-m+1)a'}{h} \right\} \tan^{-1}\left(\frac{(n-m+1)a'}{h} \right) \quad . \qquad \text{(A57)}
\end{aligned}
$$

In Fig. (A.11), the calculated magnetic field in the z direction, B_z, is shown for different positions in the gap. The results are obtained numerically by breaking the magnetization into approximately 100 discrete sections and then solving the integral equation (A.38). The plots of B_z for larger gaps are similar. The forces calculated from this model are substantially larger than those from the model with uniform magnetization (see Fig. A.12, where the dashed curves are the results of this model. The other curves and data are the same as in Fig. A.8). Saturation of the magnet core is not accounted for in this model, so the sublinear behavior of the experimental force vs. current squared is not reproduced. The agreement with experiment for smaller values of current is reasonable, however.

The phenomena of the peaking of the field, and hence the peaking of the magnetization, is clearly established by this model.

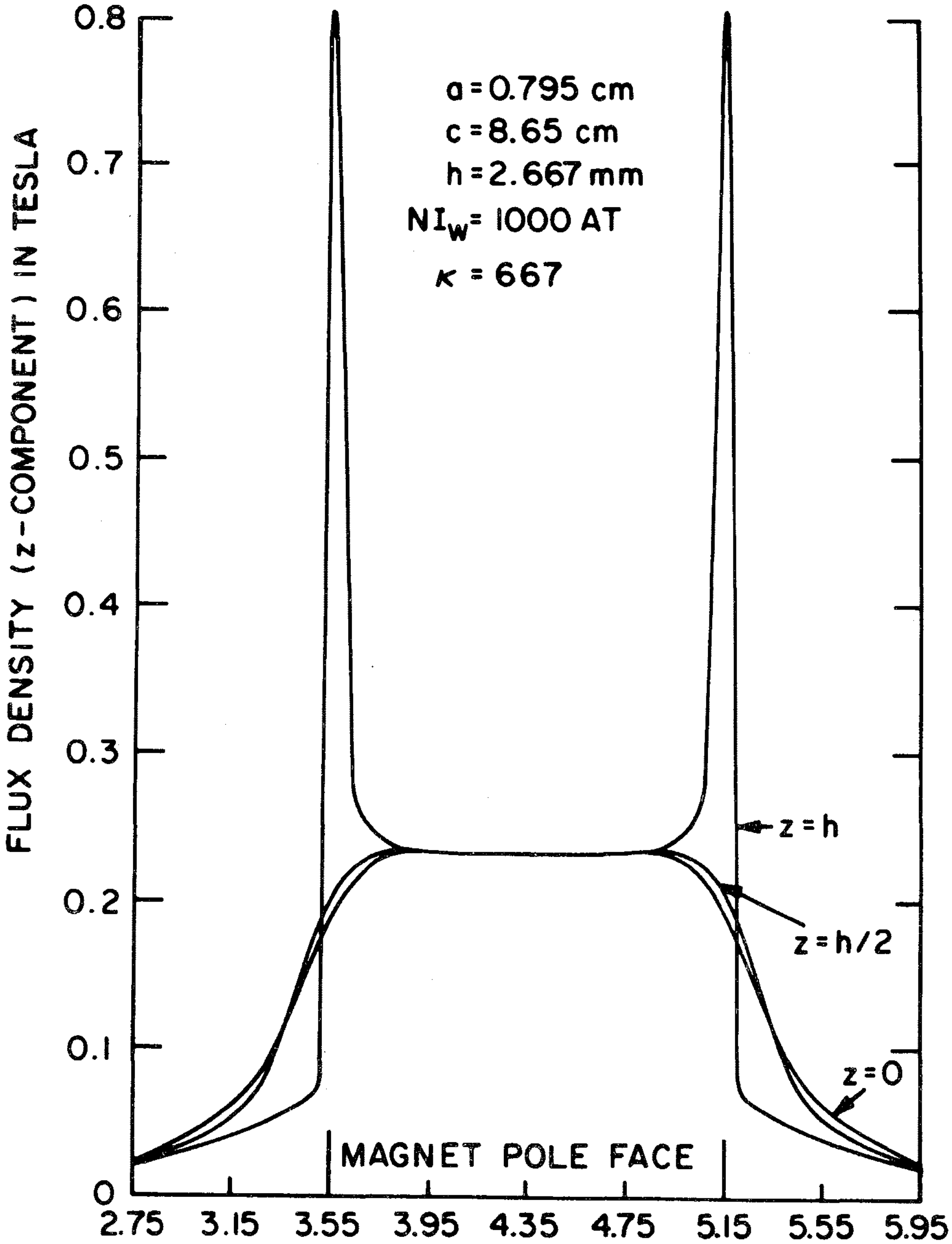

Fig. A.11. Flux density in gap region for non-uniformly magnetized (h = 2.667 mm) poles.

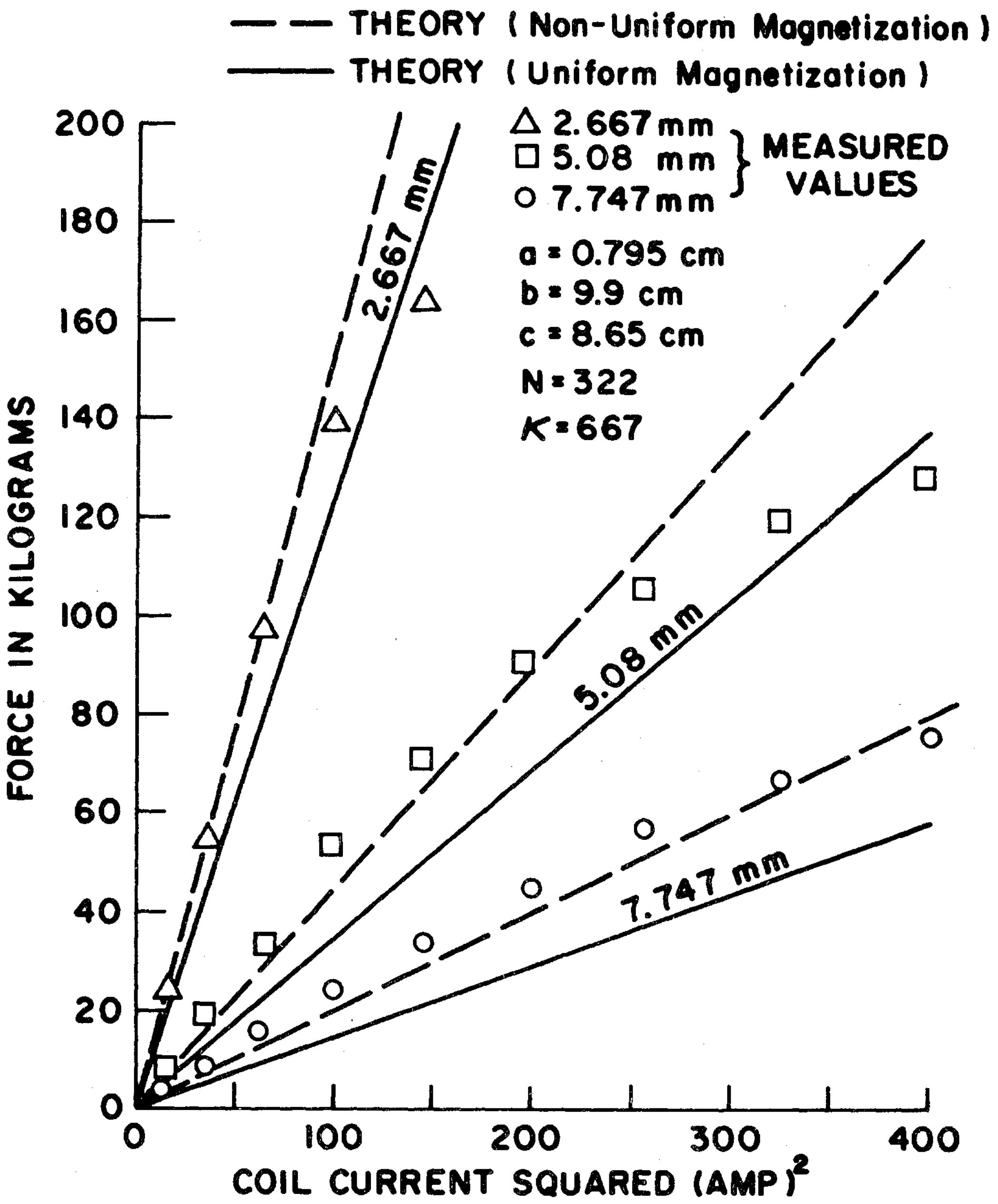

Fig. A.12. Lift force vs. current squared. A comparison of the results of the model with non-uniform magnetization to the results from assuming uniform magnetization and also to the experimental results.

APPENDIX B. FIELD AND EDDY CURRENT MAPPING

B.1 Magnetic Field and Eddy Current Calculations for the Attractive (Electromagnetic) System

A model of the ferromagnetic system is shown in Fig. B.1. It has been described previously (see Sec. 3.1. of reference 1). This work was done prior to the modifications introduced in the present report. The general features are thought to be valid, however. We consider the case where $T \to \infty$ (infinite thickness) and μ equals a constant, $\varkappa \mu_o$. It was thought to be worthwhile to examine the magnetic field patterns for such a system. This will enable us to determine how serious the magnetic saturation of the track is and where it is occurring. We will also be able to examine the spatial dependence of the skin depth.

From our previous work, it is straightforward to show that for $z < 0$ (inside the track)

$$B_\gamma(x,y,z) = 4\mathrm{Re}\int_0^\infty dk_x \int_0^\infty dk_y \, b_\gamma \sin k_y y \sin k_y c/2 \; e^{ik_x x + \alpha z} \quad , \quad \gamma = x,z \tag{B.1a}$$

and

$$B_y(x,y,z) = -4\mathrm{Re}\int_0^\infty dk_x \int_0^\infty dk_y \, b_y \cos k_y y \, \sin k_y c/2 \; e^{ik_x x + \alpha z} \, , \tag{B.1b}$$

where

$$b_y = i k_y b_x / k_x \quad , \quad b_z = -i k b_x / \beta k_x \quad , \tag{B.2a}$$

$$k = \sqrt{k_x{}^2 + k_y{}^2} \quad , \quad \beta = \alpha / k \quad , \tag{B.2b}$$

$$\alpha = \alpha_1 - i \alpha_2 \quad , \quad \alpha_{1,2} = 2^{-1/2} [(\lambda_1^2 k_x^2 + k^4)^{1/2} \quad , \tag{B.2c}$$

$$\lambda_1 = \varkappa \mu_o \sigma v \quad , \quad b_x = -2i \, \beta W_1 / (1 + \beta/\varkappa) \quad , \tag{B.2d}$$

and

$$W_1 = (\mu_o J / \pi^2 \; k_y k \sin k_y a \, \sin k_x b \; e^{-kh} \quad . \tag{B.2e}$$

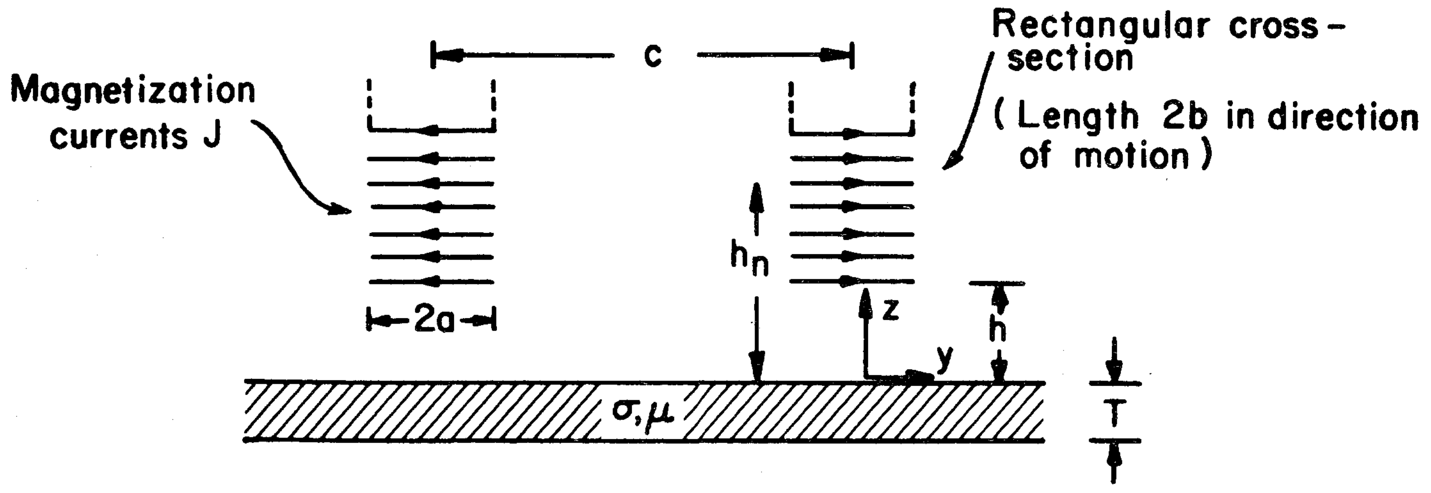

Fig. B.1. Theoretical model of magnet and track. (All figures B.1 - B.14 are for electromagnetic (attractive) system.)

Re denotes the real part. From the equation $\mathrm{curl}\,\underline{B} = \mu \underline{J}$, the currents can be obtained,

$$J_x = \frac{4}{\kappa\mu_0} \,\mathrm{Re} \int_0^\infty dk_x \int_0^\infty dk_y \,(k_y b_z + \alpha b_y) \cos k_y y \sin k_y c/2 \, e^{i k_x x + \alpha z} \qquad \text{(B.3a)}$$

$$J_y = \frac{4}{\kappa\mu_0} \,\mathrm{Re} \int_0^\infty dk_x \int_0^\infty dk_y (\alpha b_x - i k_x b_z) \sin k_y y \sin k_y c/2 \; e^{i k_x x + \alpha z} , \qquad \text{(B.3b)}$$

and

$$J_z \equiv 0 \quad . \qquad \text{(B.3c)}$$

For $h > z > 0$ (gap region)

$$B_\gamma(x,y,z) = 4 \,\mathrm{Re} \int_0^\infty dk_x \int_0^\infty dk_y (a_\gamma e^{-kz} + a'_\gamma e^{kz}) \sin k_y y \sin k_y c/2 \, e^{ik_x x} , \quad \gamma = x,z , \qquad \text{(B.4a)}$$

and

$$B_y(x,y,z) = -4 \mathrm{Re} \int_0^\infty dk_x \int_0^\infty dk_y (a_y e^{-kz} + a'_y e^{kz}) \cos k_y y \sin k_y c/2 \, e^{ik_x x} , \qquad \text{(B.4b)}$$

where

$$a_y = i k_y a_x / k_x \quad , \quad a_z = i k a_x / k_x \quad , \qquad \text{(B.5a)}$$

$$a'_y = i k_y a'_x / k_x \quad , \quad a'_z = -i k a'_x / k_x \quad , \qquad \text{(B.5b)}$$

$$a_x = - \Gamma a'_x \quad , \quad \Gamma = (1-\beta/\kappa)/(1+\beta/\kappa) \quad , \qquad \text{(B.5c)}$$

and

$$a'_x = - i W_1 \quad . \qquad \text{(B.5d)}$$

Some typical results are shown in Figs. B2-B4 for an example taken from reference 1 (p. 84). The x coordinate is in the direction of motion, y is transverse and z is vertical. The origin of the coordinate system is at the center of the magnet on the top surface of

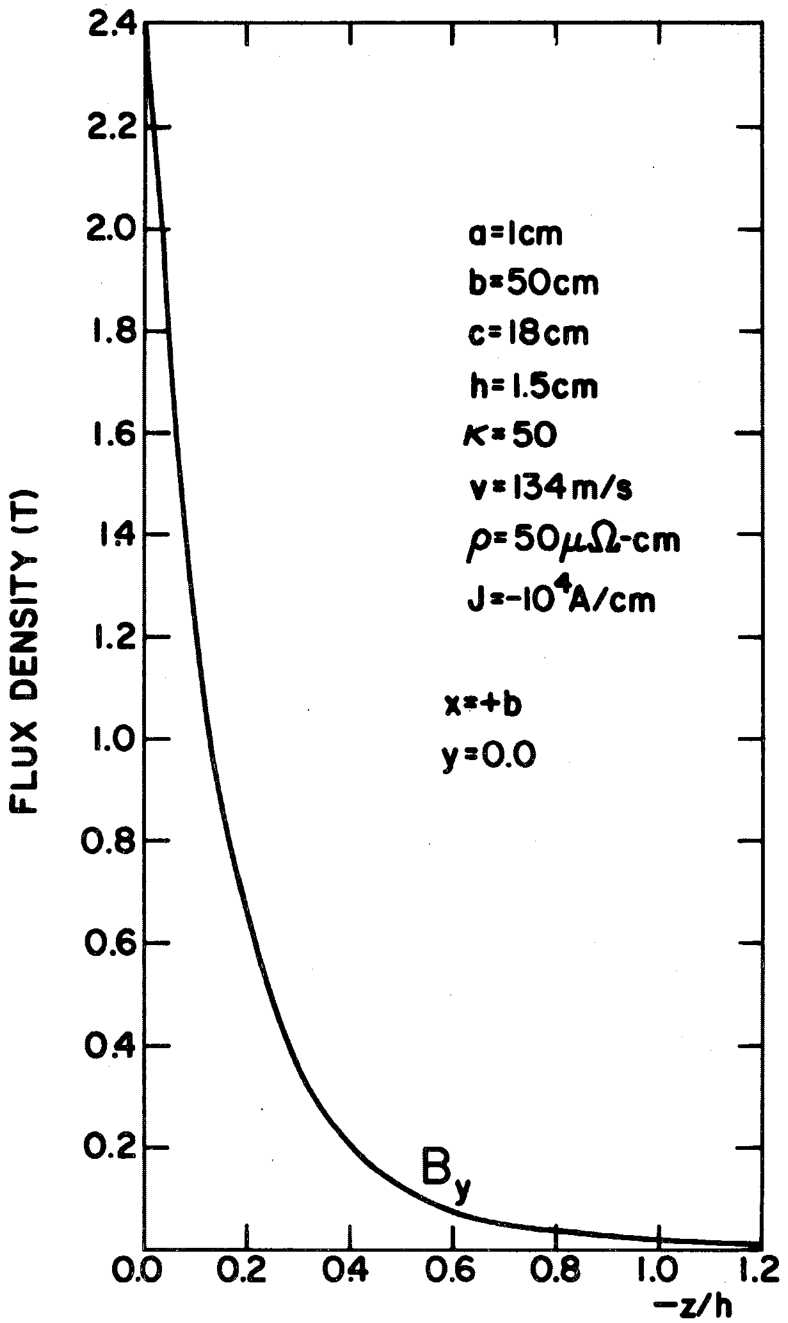

Fig. B.2. Magnetic field in the track as a function of depth for magnet mid plane, $(y = 0)$. $x = +b$ is the leading edge of the magnet.

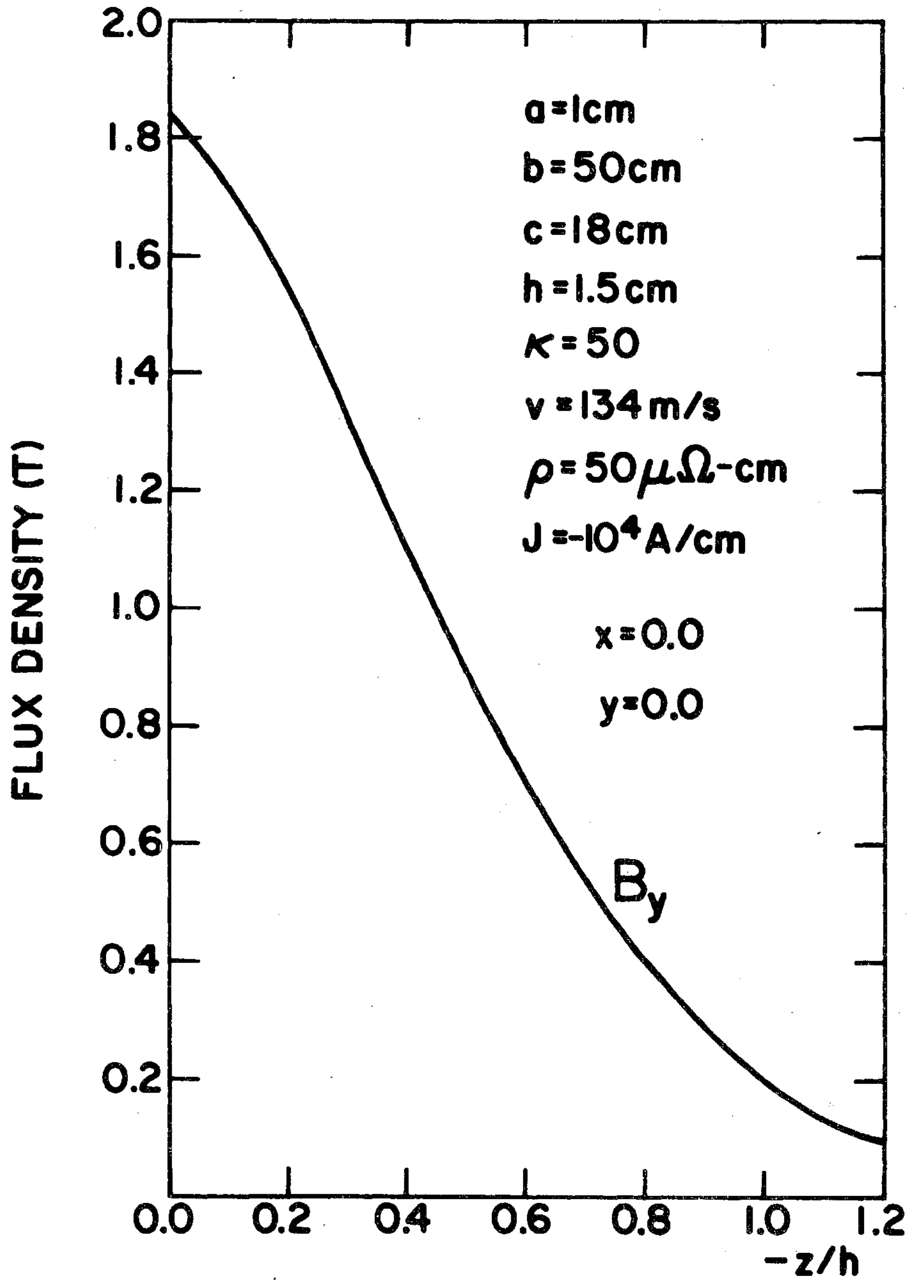

Fig. B.3. Magnetic field in the track as a function of depth for magnet mid plane ($y = 0$). $x = 0$ is the center of the magnet.

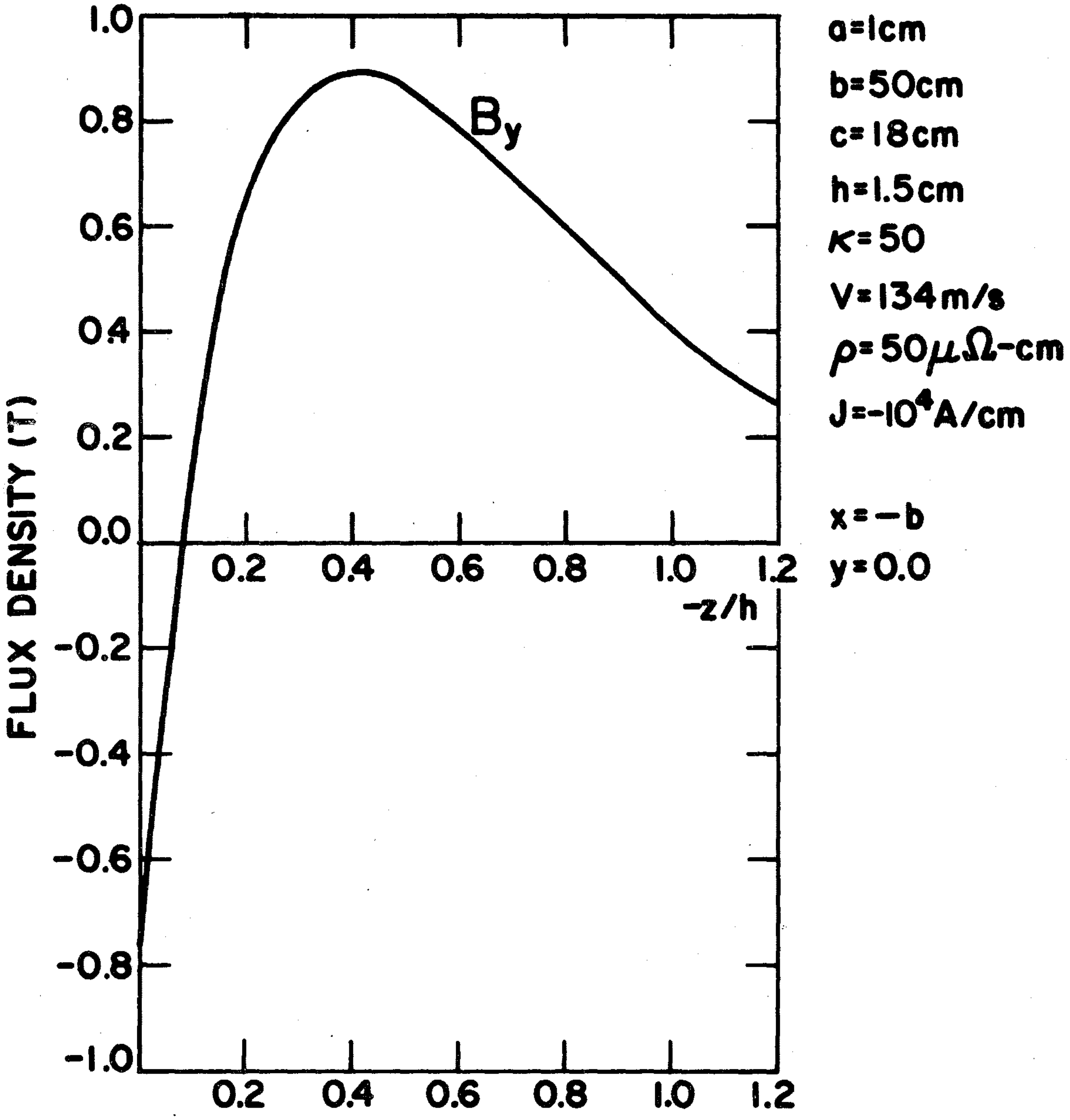

Fig. B.4. Magnetic field in the track as a function of depth for magnet mid plane ($y = 0$). $x = -b$ is the trailing edge of the magnet.

of the track (not under a pole face as indicated in Fig. B.1). Hence, $y = 0$ is the midplane of the magnet, $x = b$ is the leading edge, $x = 0$ is is the center, and $x = -b$ is the trailing edge. Due to symmetry, only $B_y \neq 0$ for $y = 0$.

The skin depth from the formula

$$\delta \simeq (2/\kappa\mu_o \sigma v k_x)^{1/2} \tag{B.6}$$

(See Eq. (3.9) of reference 1) turns out to be

$$\delta \simeq 0.41 \text{ h} \tag{B.7}$$

when $k_x = \pi/2b$ and the parameters are as given in the figures. We note that the effective skin depth at the leading edge is somewhat smaller than δ and approximately δ at the center. At the trailing edge, the field reverses sign near the surface, and it is difficult to define a skin depth. However, the field is mostly confined to a region only a few δ wide. Calculations for other magnetic lengths indicate that the penetration of the field into the track scales fairly well with δ.

For $J = -10^4$ A/cm (magnetization currents), the gap field B_z at $z = 0$ under a pole face is 0.45T for $v = 0$, a reasonable field. Since we have chosen an example with a low permeability, $\kappa = 50$, the fields in the track do not excedd the saturation value (~ 2.0 T) by very much.

Data are presented for the field under a pole face of the magnet in Fig. B5. The three components of the field just below the surface of the track are shown for zero velocity ($v = 0$). Just above the track surface. B_x and B_y are smaller by a factor $1/\kappa = .02$ whereas B_z is the same as just below the surface. The leading edge of the magnet is at 50 cm and the trailing edge at -50 cm. The y-coordinate is $c/2 = 9$ cm, which corresponds to the middle of the pole face.

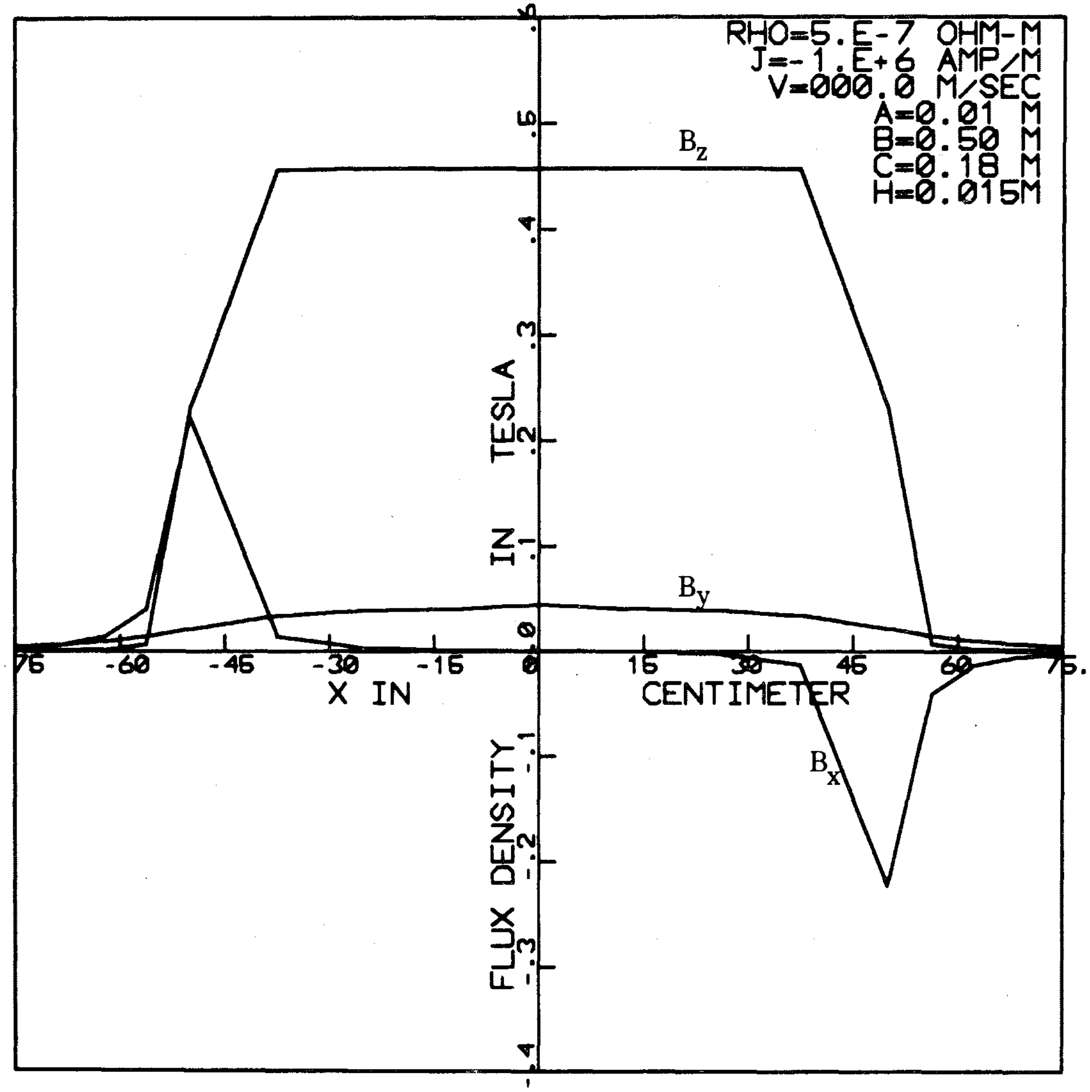

Fig. B.5. Three components of field just below track surface. v = 0.

The same field components are shown in Fig. B.6 for v = 134 m/s. We note that B_z is still nearly uniform under the pole face, being slightly smaller in the front than in the back. The magnitude of B_z is roughly the same, also, since the magnetization currents J (not real ampere-turns) have been held constant. (Note there is a vertical scale change between Figs. B.5 and B.6.) There is a striking difference in the horizontal components, both of which are much larger for v = 134 m/s. If it were possible to shape the pole faces in such a manner as to reduce these horizontal components, the performance of the magnet might be improved. This requires further investigation.

Field penetration into the track under the pole faces is limited by the skin depth in much the same way as for the magnet midplane.

To investigate the current patterns, it is convenient to plot $\underline{I} = \int_{-\infty}^{0} \underline{J}\, dz$. $\underline{I}$ can be found readily from the equations for J_x and J_y given previously (B.3). Recall that $J_z = 0$. The general current flow is shown schematically in Fig. B.7. The current loops are divided into two groups. The first encircles the leading edge of the pole; and the second, the trailing edge.

Detailed plots of I_x, I_y and $I = \sqrt{I_x^2 + I_y^2}$ are shown in Fig. B.8-B.14. In each case, the current is shown for $0 \leq y \leq 24$ cm for a fixed x value. I_x is symmetric about y = 0 and I_y is anti-symmetric. Note that the current flows well beyond the magnet in both the direction of motion and transverse to it. In the transverse direction the currents will be restricted by the finite width of the track. This might reduce these currents from what has been calculated, thereby improving the lift force and decreasing the drag force.

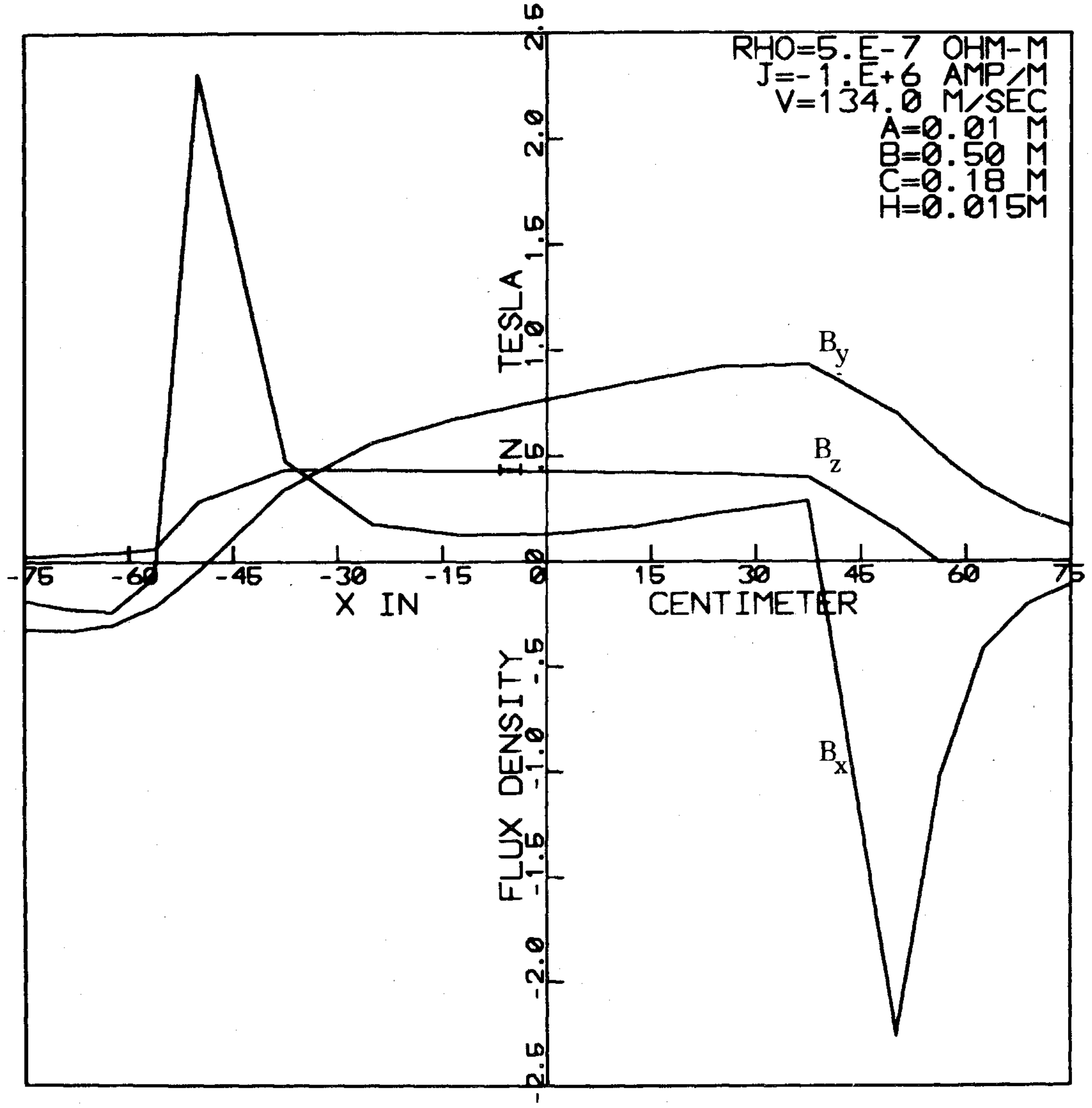

Fig. B.6. Three components of field just below track surface
v = 134 m/s. Positive x is in the direction of motion. $\varkappa$ = 50.

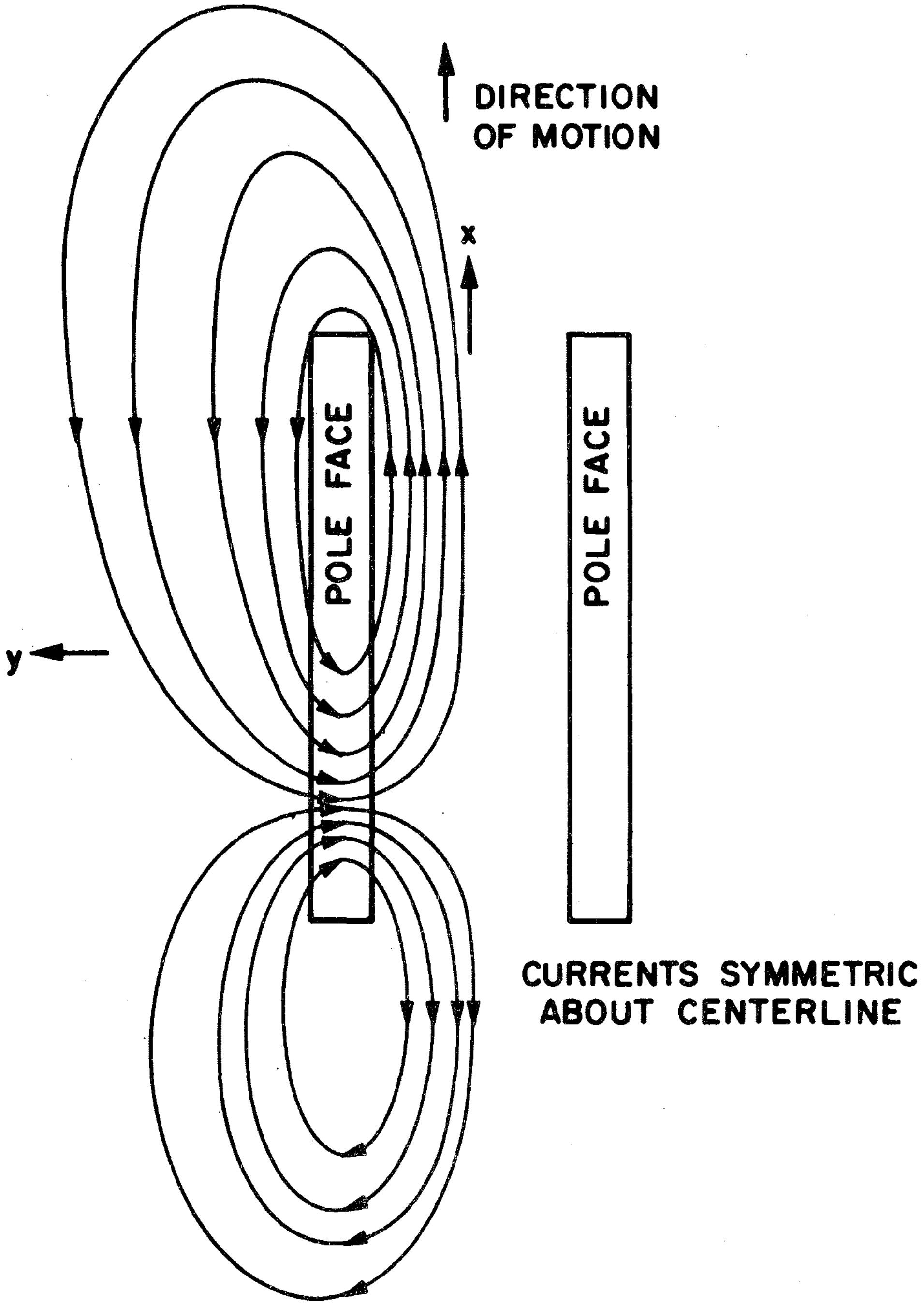

Fig. B.7. Schematic diagram of currents in track.

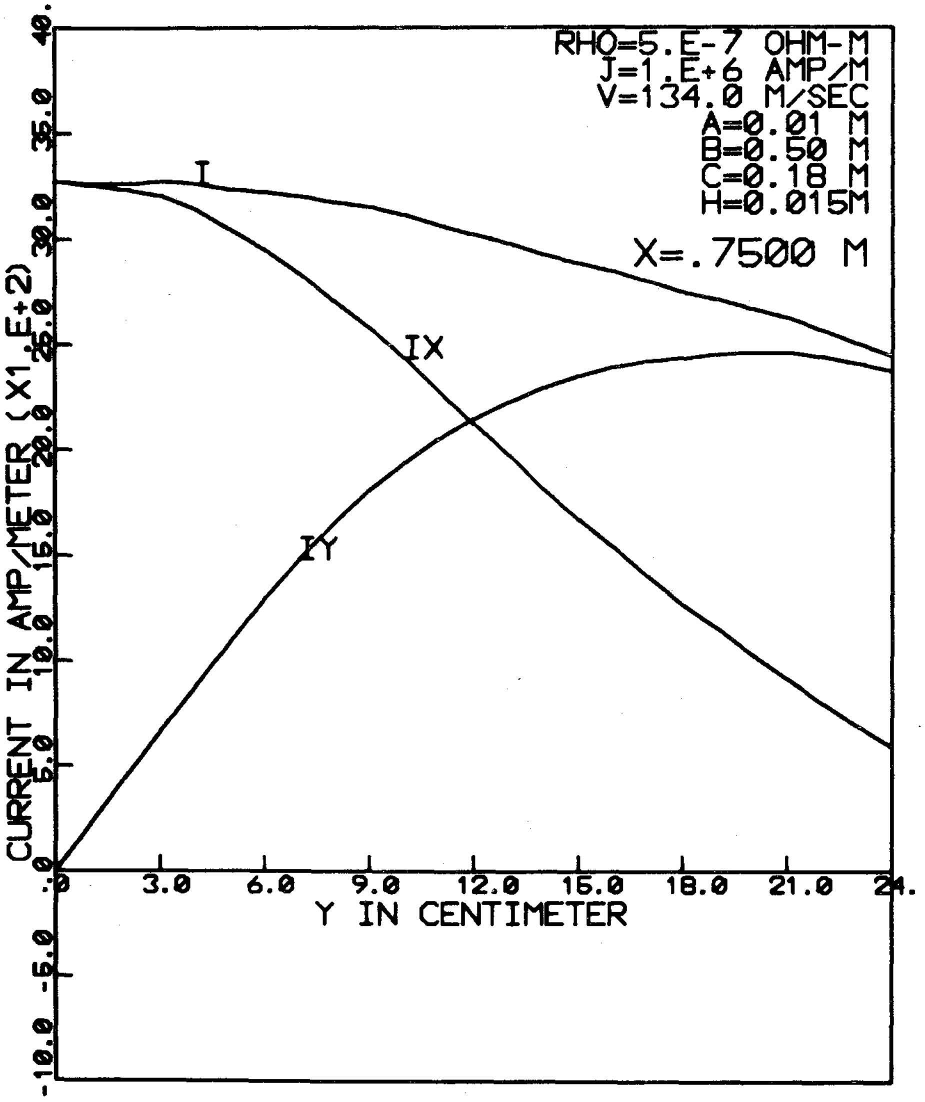

Fig. B.8. Current in track vs. y. x = 0.75 m.

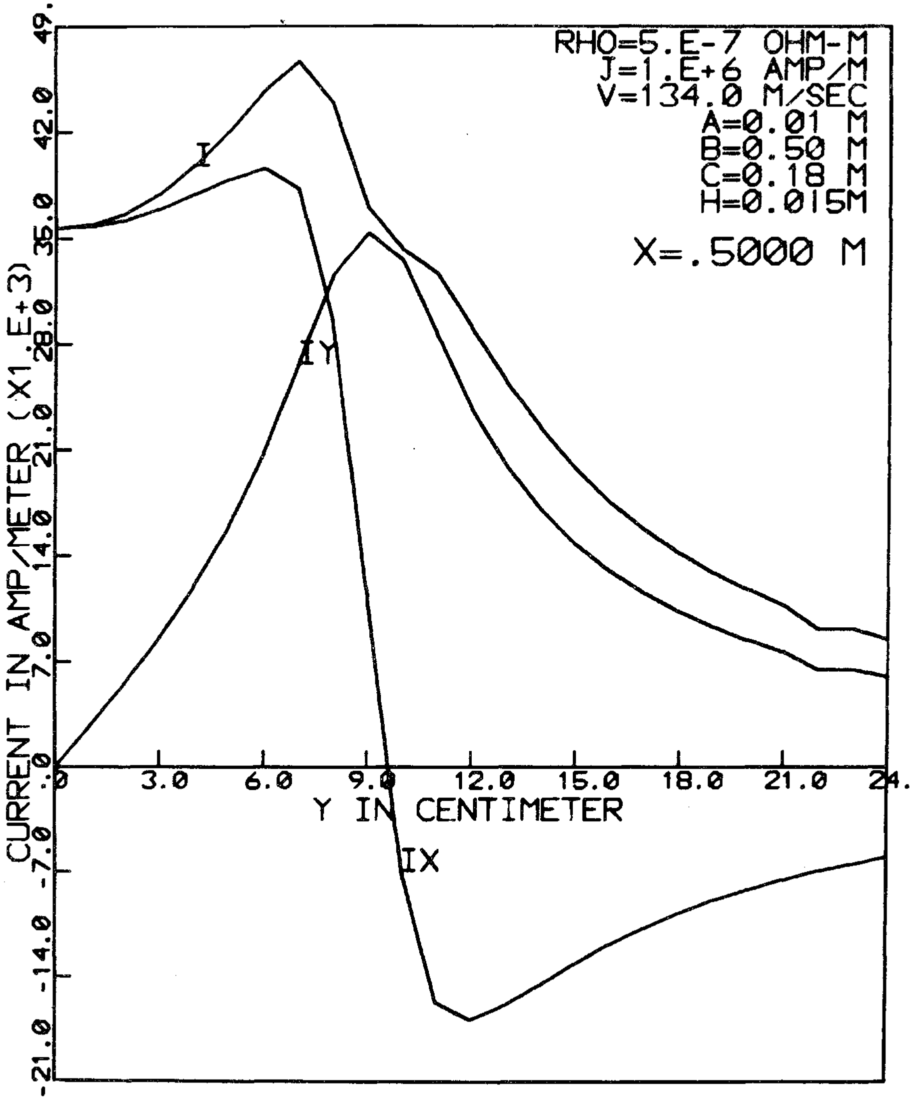

Fig. B.9. Current in track vs. y. x = 0.5 m.

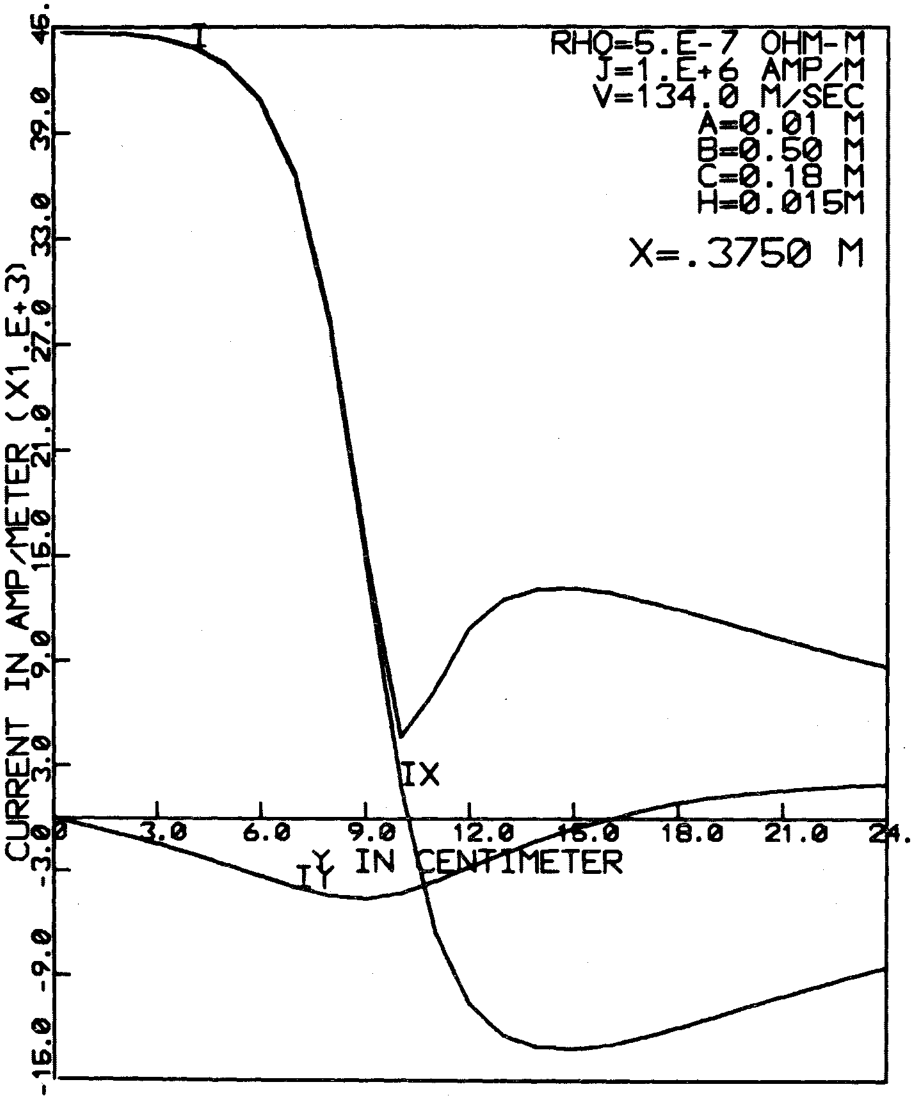

Fig. B.10. Current in track vs. y. x = 0.375 m.

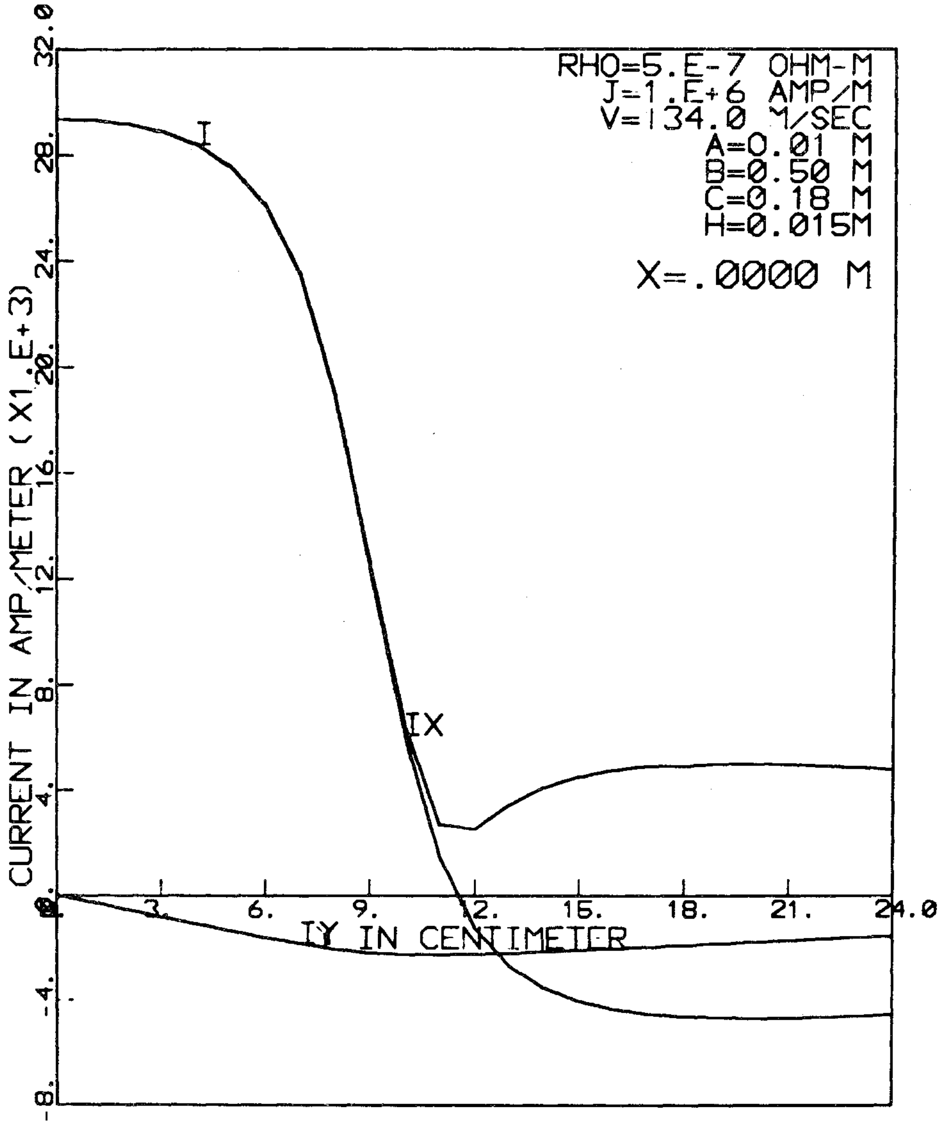

Fig. B.11. Current in track vs. y. x = 0.

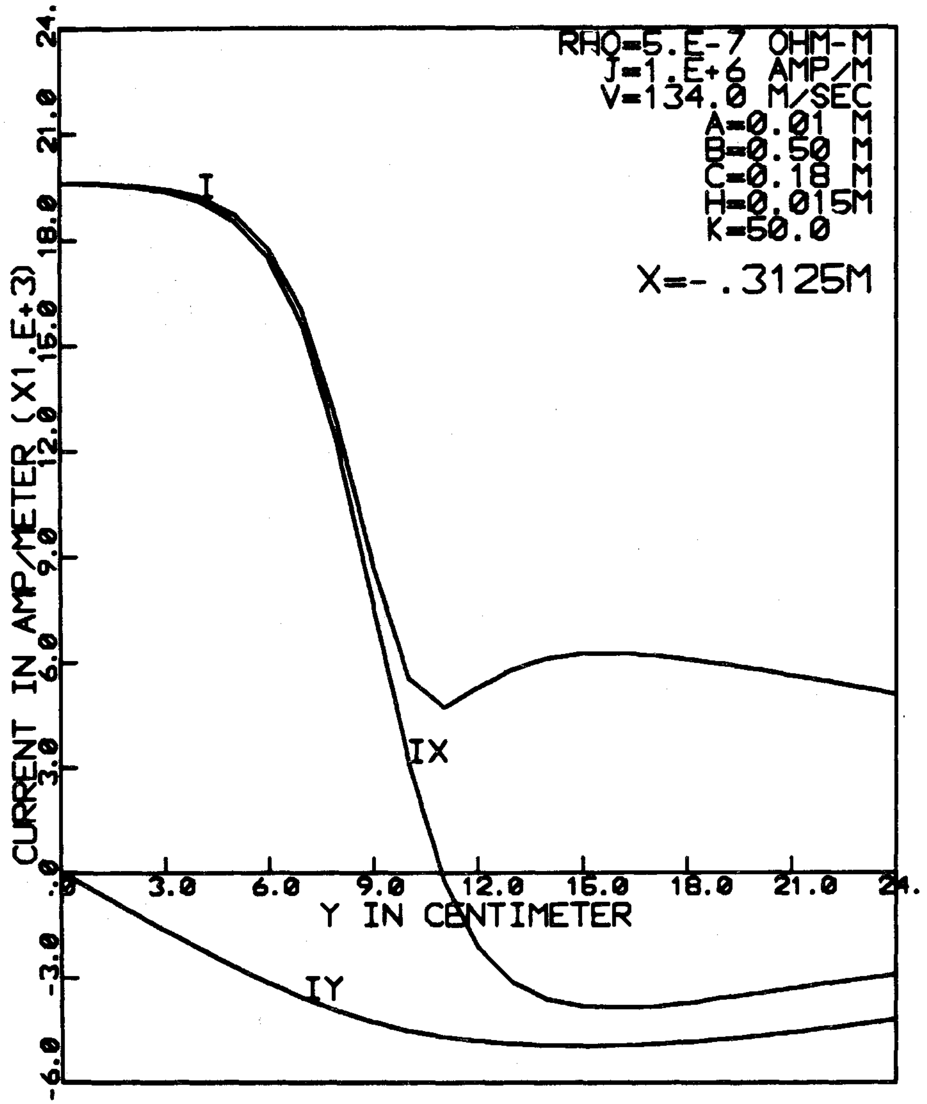

Fig. B.12. Current in track vs. y. x = -.3125 m.

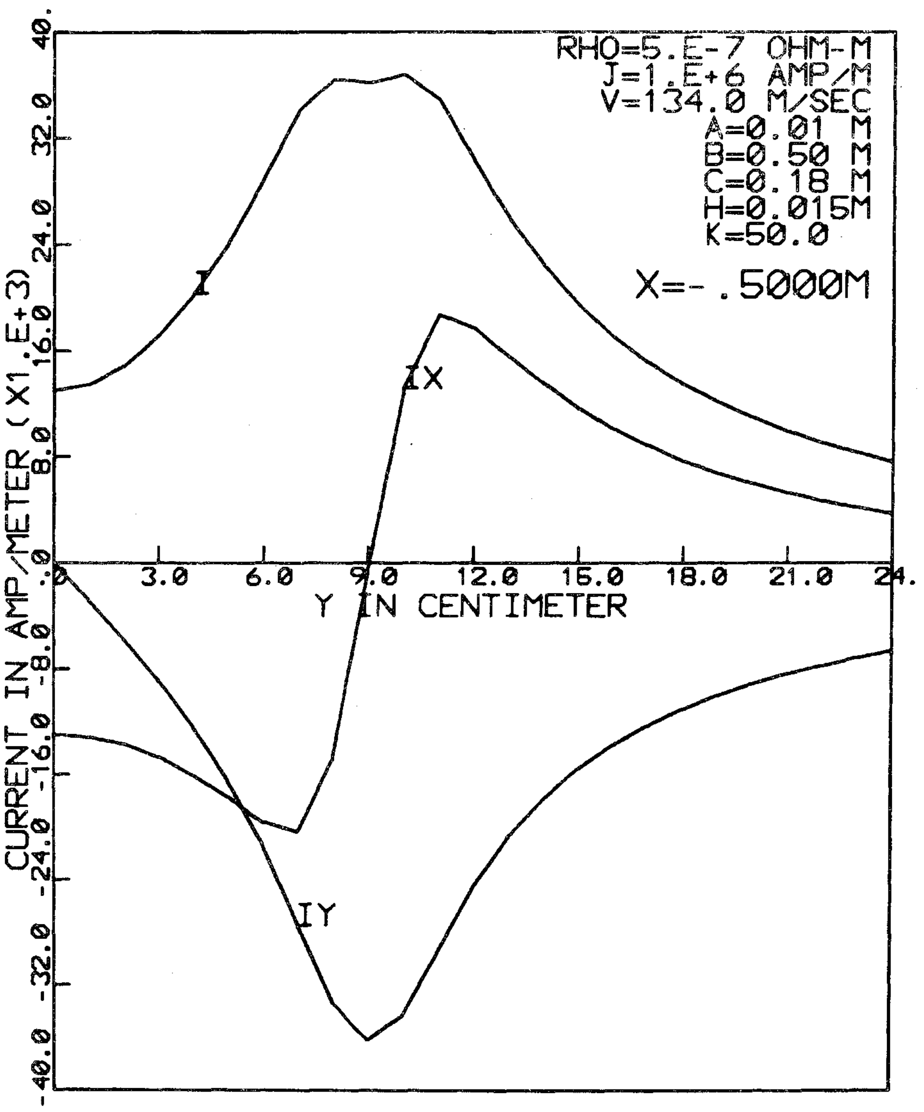

Fig. B.13. Current in track vs. y. x = -0.5 m.

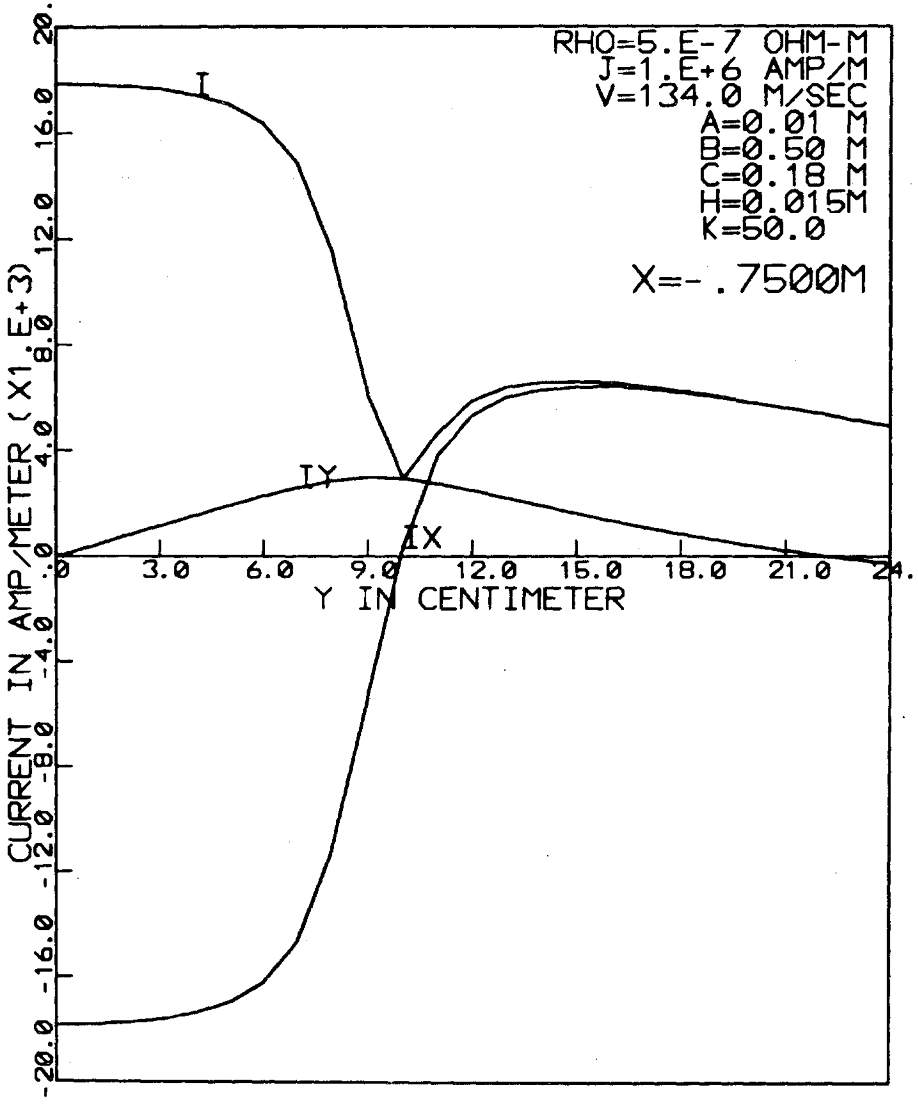

Fig. B.14. Current in track vs. y. x = -0.75 m

B.2 Track Currents in the Repulsive-Force (Electrodynamic) Suspension System

With a slight modification of the program used to calculate track currents for the ferromagnetic system, we were able to calculate these currents for the repulsive-force suspension system. We have chosen a 1/2 × 3 m coil at height 30 cm over an infinitely thick $A\ell$ track. Figures B.15-B.17 are for v = 134 m/s whereas Fig. B.18 is for v = 13.4 m/s. Fig. B.15 shows I_y (transverse current) for points along the centerline of the magnet. Positive x is in the direction of motion. We note that I_y is nearly anti-symmetric in x with respect to the center of the coil. Fig. B.16 shows I_x and I_y for x = 1m (1m in front of the coil center). It can be seen that the currents extend well beyond the coil edge (in the y direction). Fig. B.17 shows the same qualities, except x = -1 m. Finally, Fig. B.18 shows the I_y for the coil centerline at v = 13.4 m/s. The lack of odd symmetry is more evident at this lower speed (compare to Fig. B.15).

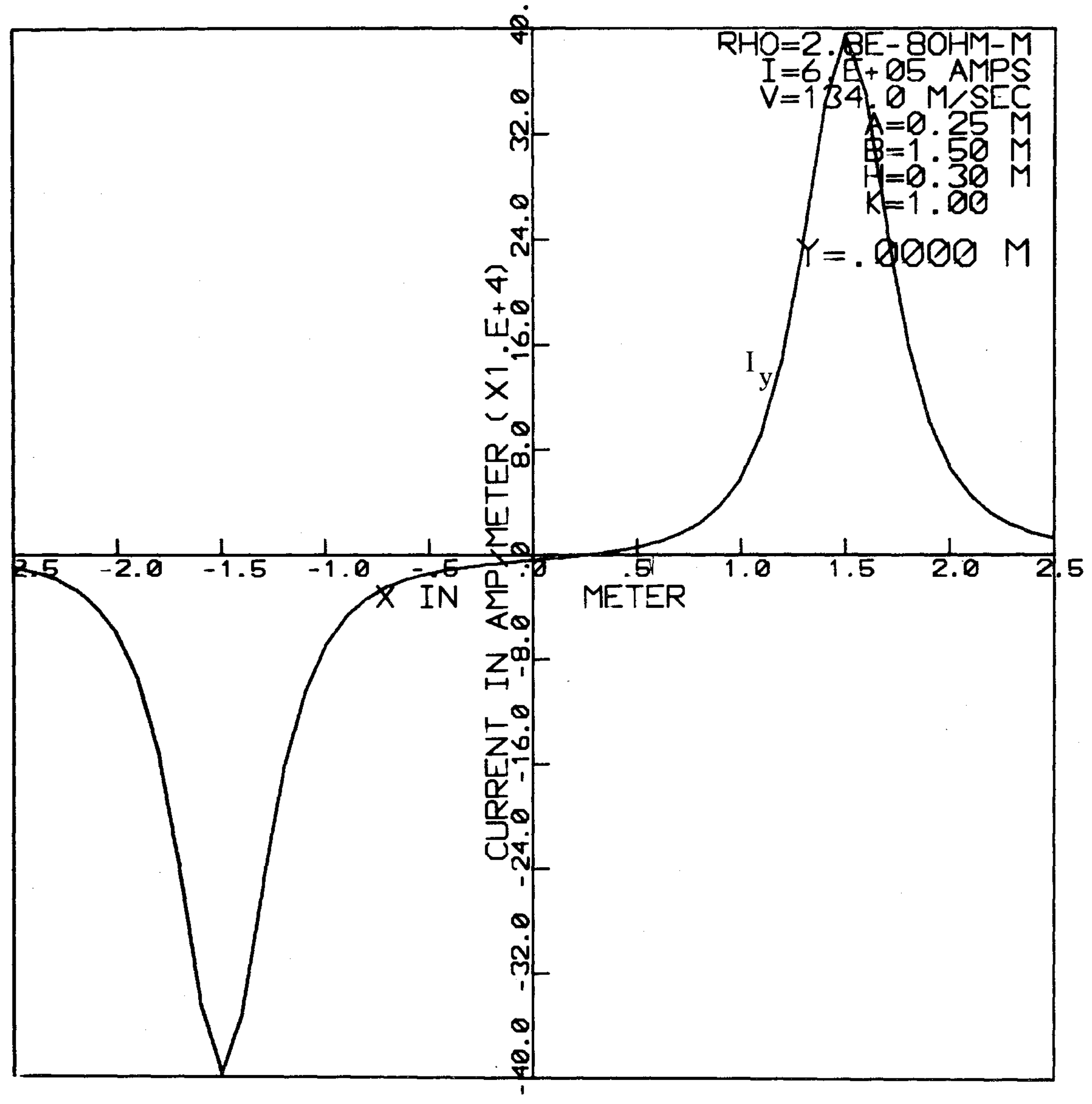

Fig. B.15. Current in track vs. x. y = 0 and v = 134 m/s. (All figures B.15 - B.18 are for electrodynamic (repulsive) system).

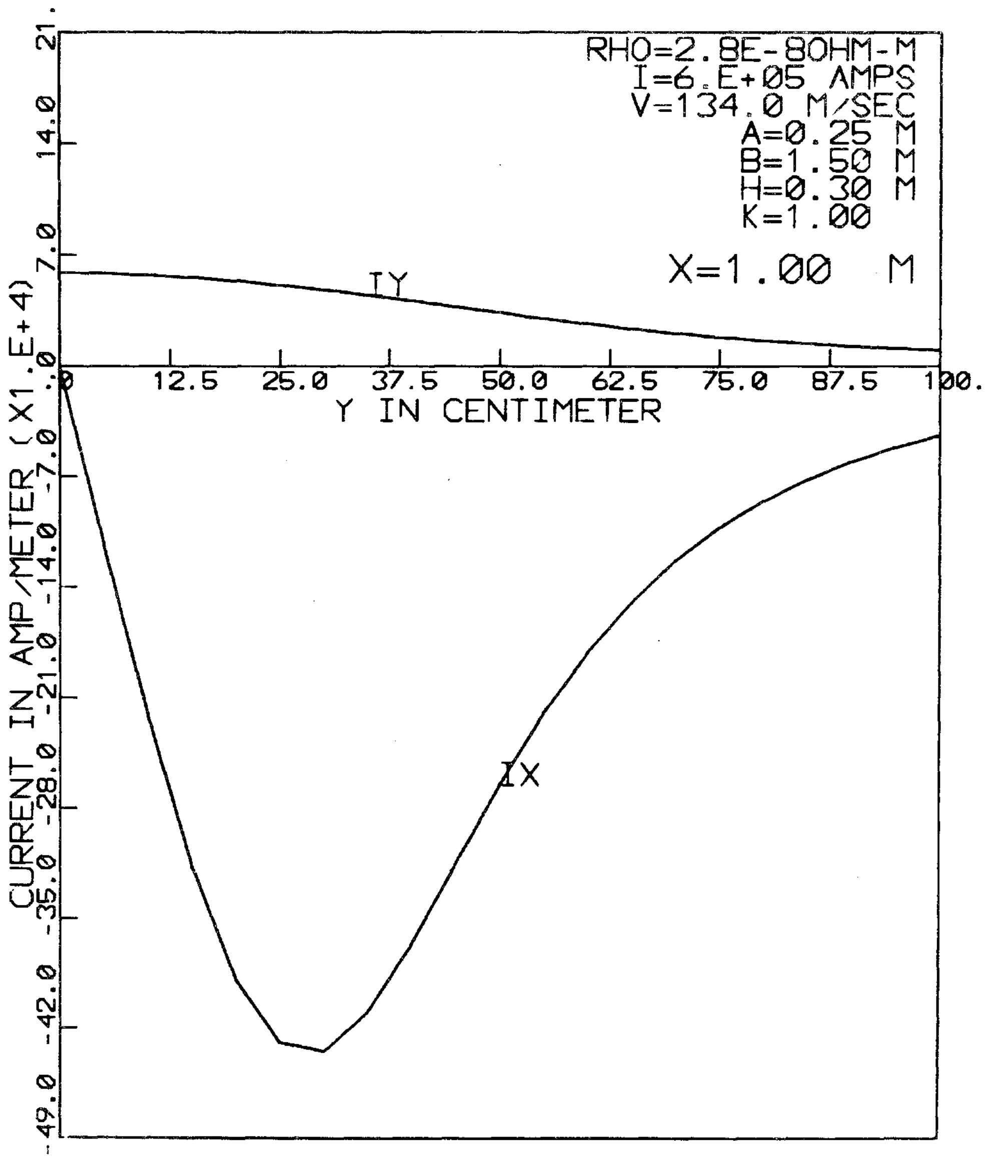

Fig. B.16. Current in track vs. y. x = 1.0 m and v = 134 m/s.

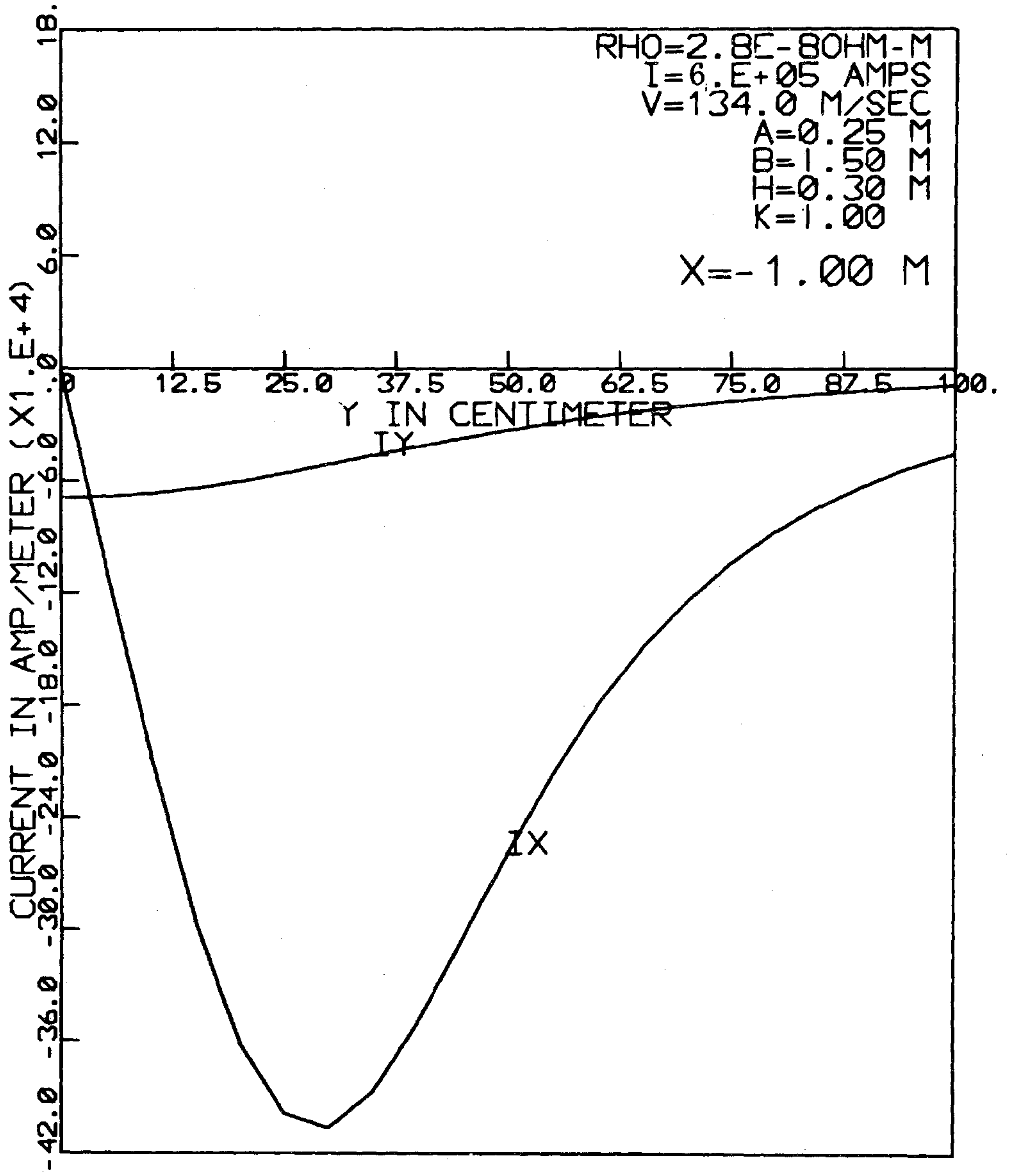

Fig. B.17. Current in track vs. y. x = -1.0 m and v = 134 m/s.

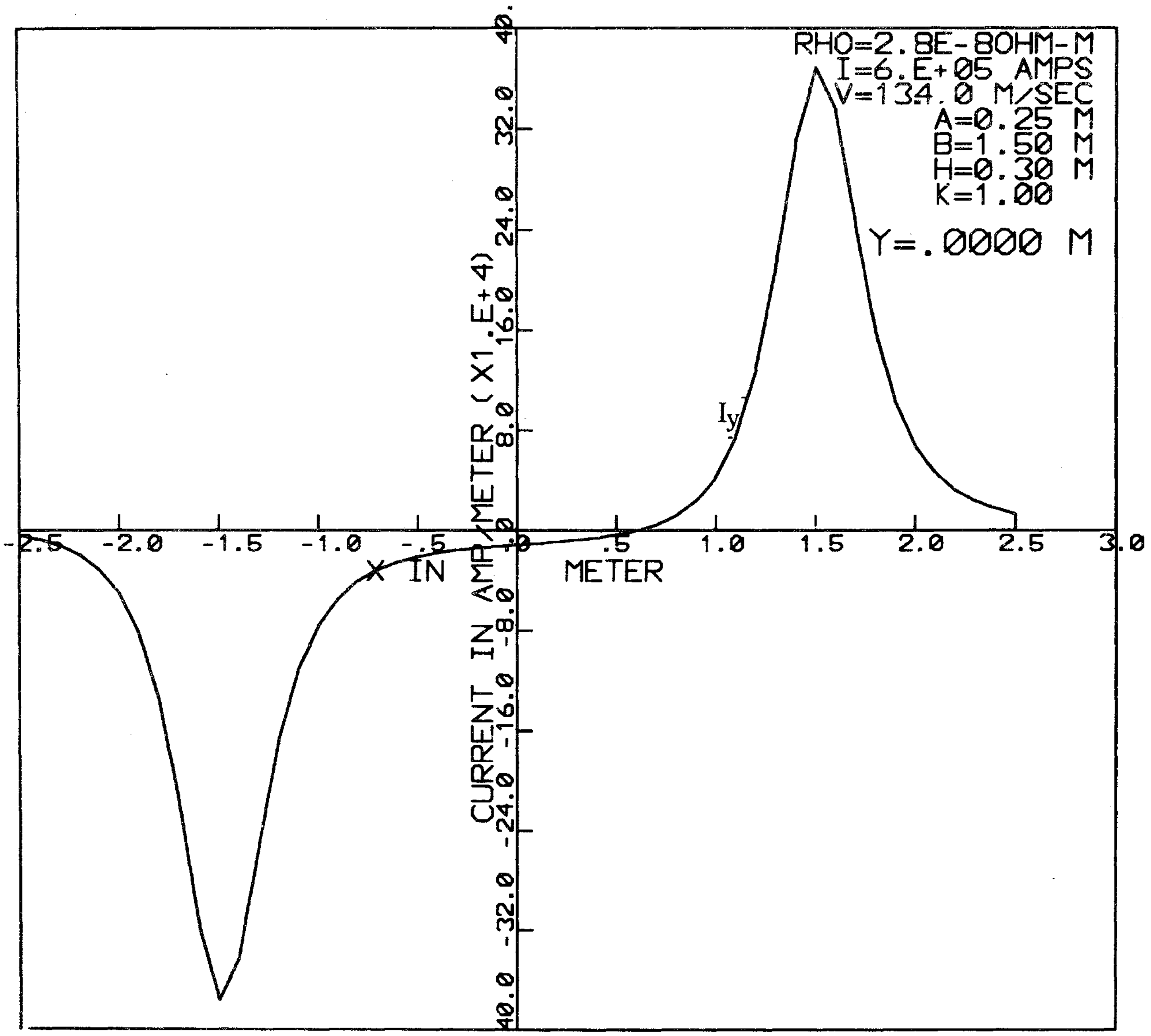

Fig. B.18. Current in track vs. x. y = 0 and v = 13.4 m/s.